“Understanding Changes in Tropical Precipitation due to Climate Change”

Submitted by **Marianne Pietschnig** to the
University of Exeter as a thesis for the degree of
Doctor of Philosophy in Mathematics in July 2020

Signature: 

Abstract

Projected precipitation changes due to increasing greenhouse gas concentrations exhibit considerable spatial structure with increases in the mid- to high-latitudes, and decreases in the subtropics. In the Equatorial regions, precipitation is projected to increase over oceans, over Africa and over the Maritime Continent, but to decrease in the Amazon basin. The decrease in precipitation over the Amazon basin and increase over the Maritime Continent are both enhanced in response to plant physiological changes. The aim of this thesis is to identify basic controls on tropical precipitation change over ocean and land, with a particular focus on the zonal asymmetry in the Equatorial region and amplification of precipitation changes due to vegetation.

We find that soil-moisture limits on evaporation and a teleconnection between Equatorial Africa and the Amazon basin contribute to the zonal asymmetry in rainfall changes over the two regions. When vegetation changes are included, the amplification of the drying over the Amazon basin is largely due to relatively weak local evapotranspiration, providing further evidence that loss of the Amazon rain forest could lead to strong decreases in rainfall. Furthermore, we find that tropical precipitation changes over a warm surface temperature anomaly are related to changes in the atmospheric energy budget, and that monsoon-type rainfall behaviour can be obtained even when the thermal inertias of land and ocean are the same, thus partly contradicting the historical view of monsoons as a large-scale land-sea breeze.

Our findings are based on idealised Atmospheric General Circulation Model simulations with continental configurations ranging from flat rectangles to realistic continents with topography. Despite their simplicity, the simulations exhibit precipitation changes similar to complex General Circulation Models, indicating that the mechanisms identified here contribute to tropical rainfall changes on Earth.

Acknowledgements

First and foremost, I would like to express my gratitude to my supervisors, Hugo Lambert and Geoff Vallis, for their scientific guidance, their enthusiasm, and for always encouraging me to conduct the research I was most interested in. I would also like to thank Marion Saint-Lu for all the helpful scientific discussions, particularly on the research presented in Chapter 4. During April and May last year I visited Abby Swann at the University of Washington and Chapter 5 is largely based on the research I conducted while I was there. I am extremely grateful to her for the interesting scientific discussions we had, for sharing her expertise on atmosphere-vegetation feedbacks and for warmly welcoming me into her research group. My gratitude is also due to Dargan Frierson for the inspiring discussions which motivated the research presented in Chapter 6. Several other academics have had an impact on the research presented here, including Mat Collins, whose insightful comment at one of the internal seminars at the University of Exeter ended up changing the basic design of my model simulations. I would also like to thank David Battisti (who suggested for me to visit Abby Swann), Brian Green and Marysa Laguë for interesting discussions during my time in Seattle. Special thanks are due to everyone from the Isca group, but in particular Ruth Geen and Stephen Thomson, who have both been incredibly helpful at solving modeling issues. I would also like to thank Ruth and my boyfriend Stefan for their helpful comments on several parts of this thesis.

I would like to express my gratitude to Dr. Michael Byrne and Dr. Tim Jupp for taking the time to read, and examine me on, this thesis, and to Prof. Mat Collins for taking the role of Non-Examining Independent Chair.

I want to acknowledge funding for my visit to the University of Washington from the Rupert Ford Award, administered by the Royal Meteorological Society and from the ADiD PhD Mobility Fund provided by the College of Engineering,

Mathematics and Physical Sciences at the University of Exeter.

I have met incredible people during my time in Exeter and Seattle, and I would like to mention a few of them here: Becky, who is without a doubt the best housemate anyone could ask for, and will always have a place in my heart. Laura, who is one of the most active and fun people I know – thank you for all the climbing, surfing and camping trips! Lauren and Jack, whom I lived with in Seattle and who spent large parts of their weekends going hiking with me in Washington. My time in Seattle would not have been the same without you two! Marion, Jules, Michelle and Sam, thank you for all the fun coffee breaks, games nights and dinners we had together during the first two years of my time in Exeter.

I am incredibly grateful to my family and friends from home for their continuous love and support. Helena, whom I've known since primary school and can be my goofy self with, but who is also a great person to turn to when things get tough. Sabine, whom I met during my undergraduate degree and have since built a very strong friendship with, which will hopefully last a lifetime. My mum and dad, who are always there for me when I need support, advice or just someone to talk to, and who have been incredibly patient with me over the last six months of my PhD, which I ended up spending at home due to unforeseen circumstances. My sister Kathi, who is one of the strongest, most independent people I know and the best sister one can ask for.

Finally, I cannot express how incredibly grateful I am to Stefan, who has been a constant source of positive energy over the past eight years and who makes my life better in so many ways.

Contents

List of Figures

List of Tables

Acronyms, Abbreviations and Symbols

AMIP, CMIP ... Atmospheric Model Intercomparison Project, Coupled MIP

ESM ... Earth System Model

GCM, AGCM ... General Circulation Model, Atmospheric GCM

ITCZ ... Intertropical Convergence Zone

MAM/JJA/SON/DJF ... March, April, May / June, July, August / September, October, November / December, January, February

MSE, MSE_b ... Moist Static Energy, sub-cloud or near-surface MSE

RCP8.5 ... Representative Concentration Pathway with 8.5 W/m^2 stronger radiative forcing by 2100 compared to pre-industrial conditions

SST ... sea surface temperature

SW, LW, SH, LH ... shortwave and longwave radiation, sensible and latent heat fluxes

TOA ... top of atmosphere

Symbol	Description	Units
α_L, α_{oc}	land, ocean albedo	1
Δ	Change due to climate perturbation	
E, E_{ctl}	evaporation, unperturbed (control) E	1 mm/d $\approx$ 28 W/m^2 of LH
E_A, E_P	actual and potential evapotranspiration	mm/d
F_{c_pT}	Vertically integrated sensible heat flux divergence	W/m^2
F_{DSE}	Vertically integrated dry static energy flux divergence	W/m^2
F_{gz}	Vertically integrated potential energy flux divergence	W/m^2
F_{Lq}	Vertically integrated latent heat flux divergence	W/m^2
F_{MSE}	Vertically integrated moist static energy flux divergence	W/m^2
F_{net}	Net energy input to the atmosphere	W/m^2
h, δh	Moist Static Energy, Gross Moist Stability	J/kg = m^2/s^2
P, P_{ctl}	precipitation, control P	1 mm/d = 1/86400 kg/(m^2·s)
$P-E$, $(P-E)_{ctl}$	precipitation minus evaporation, control $P-E$	mm/d
q, q_S	specific humidity, surface q	kg/kg
r, r_S	relative humidity, surface r	%
T, T_S	temperature, surface T	K
$\nabla.v_{h,2}$	Vertically integrated lower-level horizontal wind divergence	kg/(m^2·s)

Table 1: List of frequently used symbols

Chapter 1

Introduction

Global mean temperatures are projected to increase by 2 - 4°C compared to pre-industrial conditions by the end of the 21st century due to greenhouse gas forcing (Collins et al., 2013). The increase in temperatures is not globally uniform, with stronger warming generally projected in the high latitudes ('polar amplification', Manabe and Wetherald, 1975, Holland and Bitz, 2003, Pithan and Mauritsen, 2014, Stuecker et al., 2018) and over land (Sutton et al., 2007; Cubasch et al., 2001; Joshi et al., 2008; Lambert and Chiang, 2007). One of the many consequences of increasing temperatures for humans is the projected increase in the occurrence of heat-waves and associated deaths (Smith et al., 2014). Habitat loss for polar bears due to melting sea ice has become one of the most prominent examples of climate change impacts on wildlife (Larsen et al., 2014).

While the increase in temperatures in itself has important consequences for humans and ecosystems, the focus of this thesis is on warming-induced precipitation change, specifically in the tropics (henceforth roughly referring to the latitudinal band between 30°South and 30°North). Simply speaking, an increase in global temperatures leads to enhanced evaporation (E) and precipitation (P, Manabe and Wetherald, 1975, Trenberth, 2011). Climate models project an increase in global mean P and E of about 1 - 3 % per Kelvin warming (Collins et al., 2013; Held and Soden, 2006). Changes in precipitation (ΔP) are not globally uniform and particularly over land decreases in precipitation combined with increases in evaporation and temperatures can make droughts more severe, while the increase in atmospheric moisture can lead to an intensification of storms (Trenberth, 2011; Smith et al., 2014).

Generally, precipitation is projected to increase in the Equatorial regions (in this thesis roughly referring to 10°S - 10°N), decrease in the subtropics and increase in the mid- to high-latitudes (Fig. 1.1, Allen and Ingram, 2002, Held and Soden, 2006). This can be understood in terms of the 'wet-get-wetter' principle (see Section 2.1 and Held and Soden, 2006). According to this hypothesis, regions in which pre-industrial P exceeds E in the annual mean (such as the Equatorial regions and polar latitudes) will see an increase in $P - E$ with warming, whereas regions with a negative annual mean control $P - E$ ($(P - E)_{ctl}$) such as the subtropical oceans will see a decrease. Due to the spatial uniformity of changes in evaporation (ΔE), the changes in $P - E$ can be roughly related to ΔP itself (Held and Soden, 2006; Scheff and Frierson, 2012).

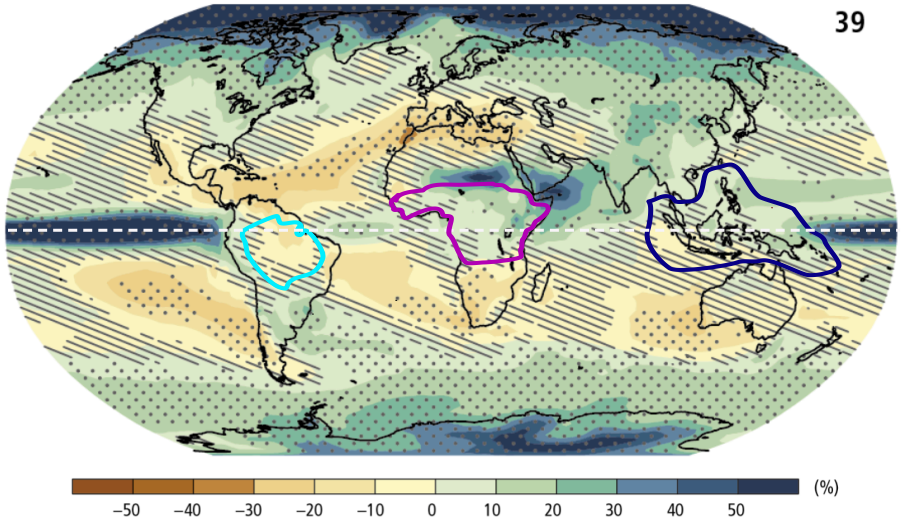

Figure 1.1: Annual mean precipitation change in percent, comparing 1986-2005 to 2081-2100 under the RCP8.5 scenario in the Coupled Model Intercomparison Project - Phase 5 (CMIP5, Taylor et al., 2012) multi-model mean over 39 models. The RCP8.5 scenario is the 'worst-case' emissions scenario, in which CO_2 concentrations increase from roughly 350 ppm in 1986-2005 to about 900 ppm in 2081-2100 (Collins et al., 2013). Increases in precipitation are shown in blue shading, decreases in brown. Stippling indicates regions where the changes are large compared to the natural variability and where at least 90% of the models agree on the sign of change, whereas hatching indicates small changes compared to the internal variability. The contours indicate the main regions of interest in this thesis: the Amazon basin (cyan), Equatorial Africa (magenta) and the Maritime Continent (dark blue). The Equator is indicated by the white, dashed line. Adapted from IPCC (2013).

While this simplification generally holds in the zonal mean and regionally over oceans, it does not apply over land (Fig. 1.1, Byrne and O'Gorman, 2015, Chadwick et al., 2013). For example, the Amazon basin is projected to receive less rainfall in the future, whereas at the same latitude Equatorial Africa and the Maritime Continent[1] are projected to see an increase in precipitation even though $(P - E)_{ctl} > 0$ in all three regions in the annual mean (Fig. 1.2, Trenberth et al., 2011, Kang and Ahn, 2015). The fact that ΔP over tropical land regions does not follow the 'wet-get-wetter' simplification is the motivation for Chapter 4.

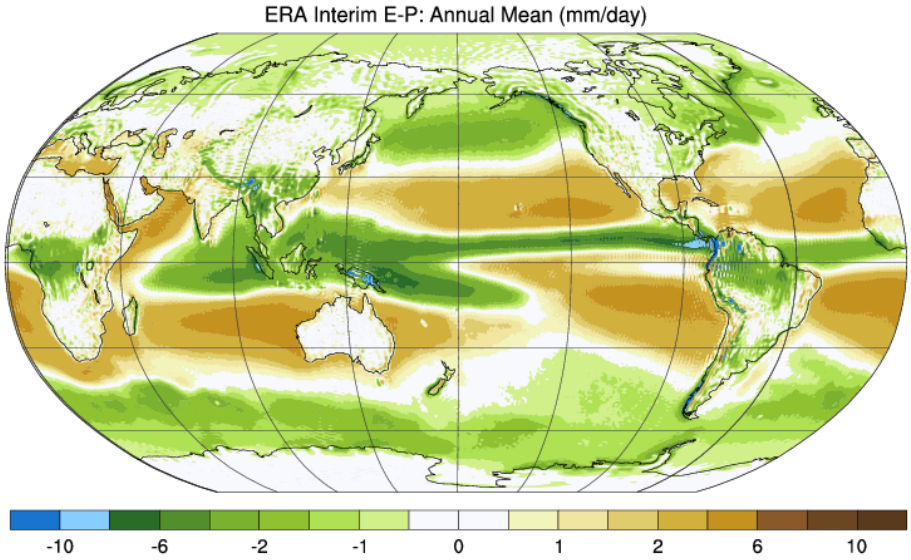

Figure 1.2: Evaporation minus precipitation ($E - P$) in mm/day from the ERA-Interim reanalysis (1979-2015, Dee et al., 2011). Regions in which precipitation exceeds evaporation are shown in green, and regions of positive $E - P$ are shown in brown. Figure from J. Fasullo, National Center for Atmospheric Research Staff (Eds). Last modified 27 Feb 2017. "The Climate Data Guide: ERA-Interim: derived components." Retrieved from https://climatedataguide.ucar.edu/climate-data/era-interim-derived-components on June 21, 2020.

Patterns of tropical ΔP over land and ocean are the subject of ongoing research (Saint-Lu et al., 2019; Kooperman et al., 2018; Byrne and O'Gorman, 2015; Chadwick et al., 2014, 2013; Xie et al., 2010), and no simple theory exists which captures all features of tropical rainfall change. Over recent decades several mechanisms have been identified which contribute to the projected patterns

[1] In this thesis, the 'Maritime Continent' refers to the continental areas only and not the surrounding oceans

in ΔP in the tropics.

Sea surface temperature (SST) patterns contribute to the distribution of tropical precipitation and precipitation change over oceans with warmer regions generally getting wetter (see Section 2.2, Xie et al., 2010 and Chadwick et al., 2014). SST anomalies can also influence ΔP over tropical land. For example, droughts in the Amazon basin have been linked to warm SST anomalies in the North Atlantic (Zeng et al., 2008; Marengo et al., 2011).

In the tropics, a warm surface temperature anomaly – be it over ocean or over a continent – can lead to rainfall changes elsewhere. The Matsuno-Gill theory of the tropical circulation (Gill, 1980 and Section 2.3) provides a helpful framework for understanding this teleconnection. The Matsuno-Gill theory states that introducing a surface heat source at the Equator leads to anomalous ascent and favourable conditions for rainfall over the heating region, and to low-level convergence and divergence aloft. This circulation pattern is associated with subsidence to the east and west of the heating, leading to unfavourable conditions for rainfall there. For example, dry conditions over the Sahara have been connected to the East Asian summer monsoon (Rodwell and Hoskins, 1996) and seasonal decreases in rainfall over the Atlantic Ocean and the Amazon basin to strong rainfall over Africa (Cook et al., 2004). In Chapter 4, this theory is employed to relate global warming induced P decreases over the Amazon basin to circulation changes over Equatorial Africa.

Another mechanism which contributes to tropical precipitation change patterns is the land-sea warming contrast (see Section 2.4). Global warming is projected to lead to stronger temperature increases over land than over ocean. The stronger warming can lead to anomalous ascent and rainfall over land, at least temporarily while the atmospheric circulation acts to export energy towards the ocean (Lambert et al., 2011).

The land-sea warming contrast is not a consequence of the different heat capacities over land and ocean (Sutton et al., 2007; Cubasch et al., 2001; Joshi et al., 2008; Lambert et al., 2011). Instead, the land-sea warming contrast is partly due to the fact that evaporation over land is more constrained compared to over ocean. Over land, evaporation is inhibited by the availability of moisture in the soil (Budyko, 1974; Manabe, 1969). In addition, plants are able to restrict the amount of moisture they release to the atmosphere (transpiration) particu-

larly in response to environmental changes (Sellers et al., 1996; Swann, 2018). The impact of limited evapotranspiration due to soil moisture and vegetation on continental ΔP will be investigated in Chapters 4 and 5, respectively.

Vegetation responses to climate change are manifold and depend on plant type and environmental stress factors among other things (see Section 2.5). From an atmospheric perspective, a key process is evapotranspiration (ET) as this provides moisture for precipitation. Plants lose water and take up CO_2 for photosynthesis through small pores on the bottom of their leaves called stomata. An increase in atmospheric CO_2 allows plants to reduce the conductance of their stomata, and thus to take up the same amount of CO_2 at a lower water cost (Sellers et al., 1996; Swann, 2018). An increase in CO_2 could therefore result in an ET decrease. However, CO_2 fertilization also allows plants to grow more biomass and increase their leaf area which in turn could potentially enhance ET. While the vegetation response to CO_2 forcing remains highly uncertain in natural ecosystems, the effect of vegetation on ET in Earth System Models tends to be dominated by the decrease due to closure of plant stomata rather than the increase due to a greater leaf area index (Swann et al., 2016; Swann, 2018; Skinner et al., 2017).

Due to the controls of vegetation on ET, climate change will not only have an effect on vegetation, but vegetation will also feed back to the atmosphere, potentially changing the strength and distribution of rainfall over land (see Section 2.6). Chadwick et al. (2017) suggested that most of the precipitation change over the Amazon basin is due to the plant physiological response to CO_2 forcing. In climate models or model simulations which do not include vegetation changes, precipitation decreases over the Amazon basin and increases over the Maritime Continent. When the vegetation response is included, the P decrease (henceforth also 'drying') of the Amazon basin and P increase ('wetting') of the Maritime Continent are both amplified (Skinner et al., 2017; Chadwick et al., 2017). The amplification of ΔP due to plant physiological changes is the motivation for Chapter 5.

On a more fundamental level, ΔP following a climate perturbation can be related to changes in the atmospheric energy budget (see Section 2.8). For example, the Hadley circulation – two global-scale atmospheric cells with ascending air near the Equator, upper-level poleward flow, descent in the dry subtropics

and equatorward near-surface flow – is essentially driven by energy gradients between the Equator and the poles, and between the Northern and the Southern Hemisphere (see Section 2.7). The Intertropical Convergence Zone (ITCZ) – associated with heavy convective rainfall – is located in the ascending region of this meridional circulation (Dima and Wallace, 2003; Bischoff and Schneider, 2014). Several studies have shown that cooling of one hemisphere (e.g. by introducing an ice sheet) leads to shifts of the ITCZ away from the cooler and into the warmer hemisphere (Section 2.7, Broccoli et al., 2006, Peyser and Poulsen, 2008). The large-scale circulation also has an impact on regional precipitation. For example, one theory for summer monsoons is that they are a regional manifestation of the seasonally migrating ITCZ (see Section 2.9). An energetic perspective on monsoons and on precipitation change in response to localised surface warming will be discussed in Chapter 6.

1.1 Research Questions

This study contributes to the understanding of tropical precipitation change by addressing the following key questions.

1. Why is the Amazon basin projected to dry out whereas Equatorial Africa is likely to receive more rainfall in the future, even though both regions see a positive $P - E$ in the unperturbed climate?

2. Why do plant physiological changes lead to an amplification of precipitation change, i.e. more drying over the Amazon basin and more wetting over the Maritime Continent compared to climate models without a representation of vegetation?

3. What are the mechanisms controlling tropical rainfall and warming-induced changes thereof over land versus ocean?

In this thesis, the idealised Atmospheric General Circulation Modelling framework 'Isca' (Vallis et al., 2018) is used (see Section 3). This flexible framework enables us to design climate modeling experiments with minimum – yet sufficient – complexity in order to capture the behavior of ΔP which we are interested in.

1.2 Thesis Structure

In Chapter 2, the necessary background knowledge for motivating the research aims and for understanding the results is outlined, including the 'wet-get-wetter' principle, the relationship between SSTs and precipitation, the Matsuno-Gill theory, the land-sea warming contrast, vegetation - atmosphere interactions, changes in the large-scale circulation, the atmospheric energy budget and a brief overview of monsoons.

In Chapter 3, 'Isca' – the University of Exeter's modelling framework for designing idealised Atmospheric GCMs (Vallis et al., 2018) – is described and an overview of the simulations studied in this thesis is given. These introductory chapters are followed by three results chapters (Chapters 4, 5 and 6), which address the key questions stated in Section 1.1 in order. In Chapter 7, the main findings from this thesis are summarised and discussed in a broader context, and possible avenues for future research are presented.

In Chapter 4, in order to study the P decrease over the Amazon basin and increase over Equatorial Africa (Question 1, Section 1.1), we first find a model set-up in Isca with realistic continents and topography which captures these ΔP patterns under a doubling of CO_2. This set-up is then simplified by representing Africa and America with two idealised, flat continents of rectangular shape, spanning the entire tropical band (30°S to 30°N). Even in this simplified simulation, the relevant ΔP patterns from complex models are still captured. This motivates us to study changes in the atmospheric circulation in our idealised simulations and infer that similar processes might govern P changes in more comprehensive models.

We find that the enhancement of ascent and precipitation over idealised Equatorial Africa (10°S - 10°N) leads to subsidence and drying over the Amazon basin. In addition, limited evaporation from land surfaces contributes to the zonally asymmetric rainfall response over Equatorial Africa and South America with global warming. The results from Chapter 4 were published in *Geophysical Research Letters* (Pietschnig et al., 2019).

In Chapter 5, the impact of changes in stomatal conductance on ΔP is investigated by including a simple representation of this constraint on evaporation over land surfaces in Isca, in addition to the limitation due to soil moisture. First

and foremost, in a simulation with realistic continents, the additional evaporative resistance leads to an amplification of ΔP over the Amazon basin and the Maritime Continent compared to the simulations where only soil moisture is included, as expected from Earth System Models. In order to address the question why different land regions respond differently to vegetation changes (Question 2, Section 1.1), we study ΔP for several rectangular continents with longitudinal extent ranging from 3° to 100° and varying degrees of stomatal closure with warming. We find that for a very narrow continent, precipitation increases more strongly when evaporation ceases with warming than when some moisture is provided by the land surface. This is due to strong temperature increases and enhancement of convection over the continent, which draws in moisture from the surrounding oceans.

Motivated by the results from Chapter 4, we also study the impact of idealised Africa on idealised America when changes in stomatal conductance are taken into account. We find that the stronger drying over the Amazon basin when stomatal conductance is reduced by 50% is mostly caused by local responses over South America, rather than by an enhancement of the teleconnection from Chapter 4. Evaporation over South America near the Equator becomes 'energy limited' in the Budyko framework, and hence E does not increase in step with P. Moisture for the strong rainfall increase along the Equator must thus be provided from other parts of the Amazon basin, leading to a decrease in rainfall there.

In Chapter 6, the fundamental question of what controls tropical rainfall and rainfall changes with warming over land and over ocean is addressed (Question 3, Section 1.1). Inspired by the Matsuno-Gill theory and the results from Chapter 4, rainfall changes for four types of surface warming are investigated. These simulations show that changes in surface temperatures alone are not a good indicator of rainfall changes – unlike what one might expect from the Matsuno-Gill theory – when changes in humidity occur. Instead, the atmospheric energy budget provides a useful framework for understanding tropical ΔP. In addition, the seasonal migration of the tropical rain band over land and ocean can be related to the near-surface energy content of the atmosphere. We find that a monsoon-type behaviour is exhibited over land even when heat capacity and albedo are the same for ocean and land due to limited evaporation from the continent.

Chapter 2

Background

2.1 The 'wet-get-wetter' principle

The paradigm that wet ($P-E>0$) regions get wetter and dry ($P-E<0$) regions get drier with warming is based on the Clausius-Clapeyron relationship

$$\frac{d\ln e_s}{dT} = \frac{L}{RT^2} \equiv \alpha(T) \tag{2.1}$$

where L is the latent heat of vapourisation ($\approx 2.45 \cdot 10^6$ J/kg) and R is the gas constant for water vapour (≈ 461.5 J/(kg $\cdot$ K), Held and Soden, 2006). For temperatures typical of the lower atmosphere $\alpha \approx 7\%K^{-1}$. This equation states that the saturation vapour pressure (e_s, in hPa) increases with increasing temperatures (T, in K). In other words, the atmospheric capacity to hold water increases with increasing temperatures. At constant low-level relative humidity ($r = 100 \cdot e/e_s$, in %) – which has been proven to be true over oceans in climate models (Byrne and O'Gorman, 2016) – the partial pressure of water vapour (e) increases in step with e_s (Held and Soden, 2006; Trenberth, 2011).

Assuming that the atmospheric circulation does not change, Held and Soden (2006) argued that the increase in low-level vapour content of the atmosphere – the 'thermodynamic' response to warming (Seager et al., 2010) – could be expected to result in an increase in $P-E$ through

$$\Delta(P-E) = \alpha \Delta T (P-E)_{ctl}. \tag{2.2}$$

$P-E$ is equal to the atmospheric moisture flux convergence in the annual mean through

$$P - E = -\nabla . \int_0^{p_S} q\mathbf{v}\frac{dp}{g}. \tag{2.3}$$

Here, q is specific humidity (in kg/kg), $\mathbf{v}$ the velocity vector, $g \approx 9.81$ m/s^2 the gravitational acceleration on Earth and the integral is performed over the entire atmospheric column ($p = 0$ at the top of the atmosphere, and $p = p_S$ at the surface, Trenberth and Stepaniak, 2001; Wills and Schneider, 2015).

The 'wet-get-wetter' approximation in Equation 2.2 essentially states that for a temperature increase ($\Delta T > 0$), patterns of $(P - E)_{ctl}$ will simply become amplified, i.e. a more positive $P - E$ near the Equator and in the mid- to high-latitudes, and a more negative $P-E$ in the subtropical regions (Fig. 1.2). Held and Soden (2006) further showed that ΔP has significantly more meridional structure than changes in evaporation and therefore related $\Delta(P - E)$ directly to ΔP.

While the wet-get-wetter principle generally works well over oceans and globally in the zonal mean (Held and Soden, 2006), ΔP over land is more complex (Chadwick et al., 2013; Byrne and O'Gorman, 2015). As discussed in Chapter 1, the Amazon basin and Equatorial Africa both see a strongly positive $P - E$ in the pre-industrial climate (see Fig. 1.2), but the Amazon basin is projected to dry out (i.e. P will decrease) under global warming while Equatorial Africa will probably receive more rainfall in the future (see Fig. 1.1). These changes in rainfall, which do not follow the 'wet-get-wetter' paradigm, will be examined in Chapter 4.

One might expect evaporation to increase at roughly 7% per Kelvin due to the increase in e_s and hence e (Eq. 2.1). However, evaporation and precipitation (i.e. the strength of the hydrological cycle) do not increase as much as expected from Clausius-Clapeyron. Instead, the global-mean increase is about 3% per Kelvin (Collins et al., 2013; Allen and Ingram, 2002; Boer, 1993; Held and Soden, 2006). The strength of the hydrological cycle does not simply increase in step with the surface temperature increase, due to the fact that P and E are controlled by the atmospheric energy budget (Mitchell et al., 1987; Boer, 1993; Collins et al., 2013).

An important consequence of the weaker increase in P compared to atmospheric moisture content is a weakening of the atmospheric circulation (Held and Soden, 2006). Precipitation can be simplified as $P \approx M \cdot \omega$, where ω is the

water vapour mixing ratio[1] (mass of water vapour per mass of dry air, in kg/kg) in the boundary layer (Held and Soden, 2006; Chadwick et al., 2013). M is the mass transport from the boundary layer to the free troposphere, excluding non-precipitating shallow convection. Since the increase in P in climate models is roughly 3% per Kelvin, much less than the 7% / K increase in ω, M must decrease with warming. This weakening of the circulation is part of the 'dynamic' response to warming, combined with shifts in the circulation (Seager et al., 2010).

2.2 SST pattern changes influence tropical precipitation change

In addition to the 'wet-get-wetter' principle, ΔP over tropical oceans has also been shown to be sensitive to changes in SST patterns (Xie et al., 2010; Chadwick et al., 2014), i.e. ocean regions with stronger warming than the tropical mean also see larger increases in precipitation. Chadwick et al. (2014) demonstrated that this 'warmer-get-wetter' principle applies on all timescales. Neelin and Held (1987) argued that the relationship between surface temperatures and precipitation is due to the fact that warmer sea surface temperatures lead to an increase in low-level moisture which destabilises the atmosphere in terms of moist convection (see Section 2.8).

Changes in SST patterns do not only influence maritime, but also continental ΔP. For example, South American rainfall outside of the rainforest regions is thought to be largely controlled by Pacific SST anomalies, with El Niño events resulting in less rainfall, particularly in the wet season (Moron et al., 1995; Erfanian and Fomenko, 2017). However, the 2005 and 2010 dry-season (May - September) droughts in the Amazon basin are more likely linked to warm SST anomalies in the North Atlantic (Zeng et al., 2008; Marengo et al., 2011). Warmer SSTs lead to stronger convection in the North Atlantic and – consequently – more subsidence in the South Atlantic and over the Amazon, reducing rainfall in those areas. The mechanism by which a warm SST anomaly in one region can impact the circulation elsewhere is described in the following section.

[1] The mixing ratio is related to specific humidity q via $q = \frac{\omega}{\omega + 1}$, and since $\omega << 1$, $q \approx \omega$.

2.3 Matsuno-Gill Circulation

The Matsuno-Gill model of the tropical circulation is a valuable framework for understanding present-day and future circulation patterns in the vicinity of a localised surface heat source. According to Gill (1980), a surface heating centered at the Equator results in the formation of an equatorially trapped Kelvin wave propagating the information eastward (Fig. 2.1a). A circulation develops with ascent over the heat source and descent to the East. The heating of the atmosphere also triggers a Rossby wave which propagates information westward and results in sinking to the west of the heat source (Fig. 2.1b). The signature of the equatorially trapped Rossby wave is a cyclone pair near the surface and associated westerly winds, and an anti-cyclone pair aloft (Fig. 2.2). The maximum speed of the Rossby wave is less than that of the Kelvin wave, hence the associated circulation patterns only extend about one third to the west of the heat source compared to the response to the east (Fig. 2.1c).

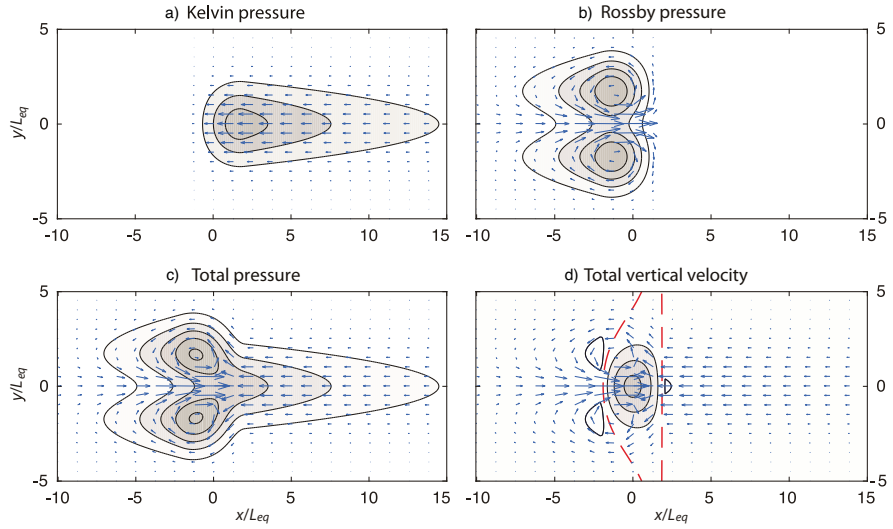

Figure 2.1: Schematic of Kelvin and Rossby-type surface pressure (a-c) and vertical wind (d) anomalies due to the imposed heating at the Equator centered around $x = y = 0$ and corresponding horizontal wind vectors. The horizontal extent of the imposed heating in this case is constrained by $|x| < 2$, and $L_{eq} = \sqrt{\frac{c}{2\beta}}$ is the equatorial deformation radius, β the Rossby parameter and c the wave speed. In (a)-(c), the contours show negative pressure anomalies, in (d) the contours show vertical velocity with ascending motion inside the red contour and sinking outside. Figure from Vallis (2017) with slight modifications.

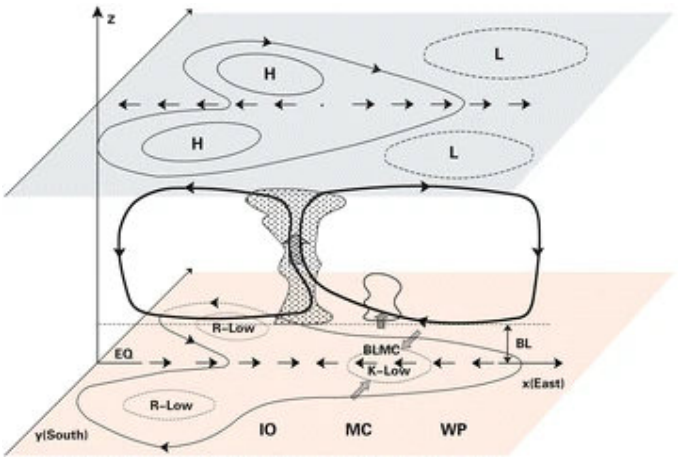

Figure 2.2: Schematic by Wang et al. (2016) linking the Madden-Julian-Oscillation to the Matsuno-Gill theory. The typical ascent over an Equatorial heat-source with Kelvin and Rossby lows to the East and West of the heating.

One of the most prominent examples of a Matsuno-Gill circulation is the Walker circulation, an atmospheric cell in zonal direction over the Pacific Ocean (Maher et al., 2019; Bjerknes, 1969; Julian and Chervin, 1978). Climatologically, warm waters around Indonesia and relatively cool temperatures in the Equatorial East Pacific lead to ascent and rainfall in the western Pacific, westerly winds aloft, descent in the eastern Pacific and near-surface easterlies. During an El Niño event, when the Eastern and Central Pacific Ocean are anomalously warm, a slowdown and shift in the Walker Circulation occurs (Julian and Chervin, 1978). The ascending branch of the circulation is shifted towards the Central Pacific leading to anomalously low rainfall over the Maritime Continent (Ropelewski and Halpert, 1987), but also droughts in the Amazon basin have been associated with El Niño (Hastenrath and Heller, 1977; Tedeschi and Collins, 2016).

As pointed out by Gill (1980), the tropical continents can be considered surface heat sources of relatively small extent. Cook et al. (2004) utilized the Matsuno-Gill framework to explain the formation of a zonal circulation between Africa and South America in the present-day climate, with an ascending branch over Africa and a descending branch over South America. Subsidence is associated with low relative humidity (Charney, 1975) and dry conditions (Rodwell and Hoskins, 1996), whereas ascent is associated with precipitation, particularly in the monsoon regions (Nie et al., 2010). Hence, strong rainfall over Africa is associated with dry conditions and little rainfall over the Atlantic Ocean and tropical South

America, particularly the Nordeste region of Brazil in January (Cook et al., 2004). Similarly, Rodwell and Hoskins (1996) argued that the Saharan desert is a result of the subsidence associated with the Rossby wave response to the Asian summer monsoon. In Chapter 4, the Matsuno-Gill theory will be employed to study warming-induced precipitation changes over Africa and South America, and in Chapter 6, the circulation and precipitation responses to different types of surface warming will be studied.

2.4 Land-Sea Warming Contrast

Land regions are generally projected to warm more than ocean regions with increasing CO_2 levels (Sutton et al., 2007; Cubasch et al., 2001). This can not be related to the different heat capacities of land and ocean, which only affect the transient warming contrast (Sutton et al., 2007; Joshi et al., 2008; Dong et al., 2009). Joshi et al. (2008) introduced a conceptual model to explain the equilibrium land-sea warming contrast. They proposed the existence of a level '*CH*' in the atmosphere, at which ΔT is globally uniform. This is particularly relevant for the tropics, where the weakness of the Coriolis force inhibits the atmosphere from maintaining strong horizontal temperature gradients ('Weak Temperature Gradient approximation', WTG, Sobel et al., 2001). The tropospheric lapse rate Γ decreases less over land than over ocean, since it is closer to the dry adiabatic lapse rate and therefore (nearly) independent of atmospheric humidity. Given a uniform warming at level *CH*, the different changes in Γ over land and ocean lead to a greater increase in land temperatures compared to the ocean.

The fact that the lapse rate over land is closer to a dry adiabat, whereas over ocean atmospheric profiles tend to be saturated (Joshi et al., 2008; Lambert et al., 2011), is due to land evaporation being limited by soil moisture availability (Manabe, 1969). Evaporative resistance over land also directly contributes to the land-sea warming contrast: Under the same radiative forcing, the ability of the land surface to release excess energy via latent cooling is restricted compared to the ocean and the radiative forcing must instead be balanced by an increase in sensible heat and upwelling longwave radiation (Manabe et al., 1991; Dong et al., 2009). Joshi et al. (2008) suggested another mechanism via which limited evap-

oration over land contributes to the land-sea warming contrast. While over oceans relative humidity near the surface is generally constant or shows a slight increase with warming, low-level r decreases over land in GCMs (Byrne and O'Gorman, 2016). Joshi et al. (2008) related this to the horizontal transport of moisture from ocean to the warmer land at a level C above the boundary layer. Since this level is cooler than the surface, the specific humidity at level C (q_C) corresponds to a lower relative humidity over the warmer land. The land surface initially evaporates in order to compensate for the gradient between the saturation specific humidity at surface temperature and q_C. However, evaporation quickly becomes limited by available moisture, again leading to an increase in surface temperatures (Joshi et al., 2008; Lambert et al., 2011).

Interestingly, the land-sea warming contrast $\phi = \frac{\Delta T_L}{\Delta T_O}$, where ΔT_L and ΔT_O denote land and ocean surface temperature changes, respectively, is remarkably similar under transient and equilibrium climate change (Lambert et al., 2011; Manabe et al., 1991; Joshi et al., 2008). Lambert et al. (2011) argued that this is due to a rapid adjustment in the atmospheric transport of energy between land and sea. Depending on the experimental design - be it a uniform increase in SSTs, a doubling of CO_2 with fixed control-climate SSTs or a mixed-layer ocean that is free to respond to the CO_2 forcing - the atmosphere exports energy away from the regions of stronger heating to regions of no or weaker warming. In the case of a uniform SST increase, where the ocean warms instantly while land surface temperatures initially remain unperturbed, convection increases over the ocean and subsidence over land, resulting in rainfall shifts from land to ocean and warming of the land. This atmospheric energy transport maintains its strength in the equilibrium climate. Conversely, in a doubling of CO_2 experiment (with or without fixed SSTs), the atmosphere transports energy away from the land, thereby shifting P away from the ocean towards the land. The atmospheric heat transport from land to ocean constrains the land to warm at roughly the same rate as the ocean. When equilibrium is reached, the atmospheric heat transport from land to ocean ceases (Lambert et al., 2011).

2.5 Vegetation response to CO_2 forcing

In the previous section on the land-sea warming contrast, we only mentioned the availability of soil moisture as a limiting factor for evaporation over land. As we will discuss here, in addition to soil moisture, vegetation plays an important role in modulating evapotranspiration from the land surface and thus regional precipitation. For example, evapotranspiration from the Amazon rain forest has been shown to impact rainfall over the region and therefore deforestation could increase the risk of drought (Spracklen et al., 2012; Wright et al., 2017; Spracklen et al., 2018). Evapotranspiration is an essential source of moisture for rainfall in the Amazon basin and plays an important role in the transition from dry to wet period in the Southern Amazon (Wright et al., 2017).

In addition to the present-day climate, vegetation responses to increasing atmospheric CO_2 levels affect evapotranspiration and thus potentially precipitation changes. Plants take up CO_2 from the atmosphere through small pores on their leaves called 'stomata' (Sellers et al., 1996). Simultaneously, water is lost through the same pathway ('transpiration'). Plants can regulate the stomatal aperture, thereby controlling transpiration and CO_2 uptake.

Plant physiological responses to increasing CO_2 levels in the atmosphere are complex and depend on water stress, nutrient availability and light limitation among other factors (Skinner et al., 2018; Swann et al., 2016). On the one hand, stomatal conductance has been shown to decrease in response to increasing CO_2 concentrations (Ainsworth and Long, 2005), potentially causing a decrease in evapotranspiration (Sellers et al., 1996). On the other hand, CO_2 fertilization generally results in a greater leaf area index in most tropical regions (Skinner et al., 2018; Kooperman et al., 2018) and thus potentially enhanced evapotranspiration (ET), albeit changes in leaf area are associated with large uncertainties (Swann, 2018; Mahowald et al., 2016). The decrease in stomatal conductance, rather than the increase in leaf area, dominates the ET response to CO_2 in Earth System Models (Skinner et al., 2017; Swann et al., 2016; Swann, 2018), but the ecosystem response in the real world is highly uncertain (Swann, 2018).

In order to gain insight into the response of different kinds of natural ecosystems to elevated CO_2 concentrations, the Free Air CO_2 Enrichment (FACE) field experiments were developed (Ainsworth and Long, 2005). Prior to the installment

of the FACE sites, the study of ecosystem responses to elevated CO_2 was restricted to small-scale ecosystems in confined conditions such as greenhouses, where the plants' environment is significantly altered compared to natural conditions. While those small-scale studies formed the basis for our understanding of plant physiological responses to CO_2 forcing, they might not yield results representative of the natural response of large ecosystems to greenhouse gas forcing.

Large-scale FACE experiments provide better estimates of how natural ecosystems might respond to climate change by allowing free exchange with the atmosphere (Ainsworth and Long, 2005). However, most FACE sites are located in temperate climates, whereas ecosystems in tropical as well as arctic climates have been mostly neglected so far. At FACE sites, jets of CO_2-enriched air or pure CO_2 gas are released into an ecosystem such as a grassland, plantation or forest, such that CO_2 is elevated by about 200 ppm to 475 - 600 ppm depending on the ambient levels (De Kauwe et al., 2013). Winds and diffusion naturally distribute the CO_2 across the site. Inferring from Ainsworth and Long (2005) and Ainsworth and Rogers (2007)'s estimates from FACE sites, stomatal conductance (g_s) decreases by roughly 10% per 100 ppm CO_2 increase. Those estimates do not represent tropical ecosystems, however, since most sites are located between 35° and 45°N (Ainsworth and Long, 2005), and there is also considerable variability between different plant functional types, with the least responsive plants showing an 8% decrease (shrubs), and the most responsive (C_3 grass) an 18% decrease per 100 ppm (Ainsworth and Rogers, 2007).

2.6 Changes in evapotranspiration and precipitation due to plant physiological changes

Changes in ET over land are associated with changes in P (Spracklen et al., 2012; Kooperman et al., 2018; Skinner et al., 2017). Over the Amazon basin and the Maritime Continent, the vegetation response to increasing CO_2 levels tends to amplify the P response compared to models or simulations where the plant physiological response is not included (Swann et al., 2016; Chadwick et al., 2017; Skinner et al., 2017; Kooperman et al., 2018). Over Equatorial Africa, the effect of plant physiological changes on ΔP is less clear.

In Earth System Models, changes due to increasing CO_2 can be separated into two components: Changes due to radiative transfer changes ('rad_{CO2}') – where the CO_2 increase only affects atmospheric radiative forcing while the vegetation scheme sees pre-industrial CO_2 levels – and changes due to the plant physiological response ('veg_{CO2}') where only the vegetation scheme responds to CO_2 forcing while the radiative forcing is held at pre-industrial conditions (Swann et al., 2016; Skinner et al., 2017).

The plant physiological response (veg_{CO2}) – which tends to be dominated by changes in stomatal conductance in ESMs (see Section 2.5, Swann et al., 2016, Swann, 2018, Skinner et al., 2017) – leads to a decrease in ET over all land regions between about 15°S and 15°N (Swann et al., 2016; Skinner et al., 2017; Kooperman et al., 2018). In contrast, in the CMIP5 multimodel mean, ET increases over Equatorial Africa and the Maritime Continent in rad_{CO2} experiments, while the response is mixed over the Amazon basin (Swann et al., 2016). In the full RCP8.5 scenario simulations in the CMIP5 multi-model mean, ET is projected to decrease over the Amazon basin, whereas over Equatorial Africa and the Maritime Continent the changes are slightly positive (Collins et al., 2013), although in Swann et al. (2016), where fewer CMIP5 members are considered, the changes are slightly negative in those regions except for the East Coast of Equatorial Africa. Projections of both ΔP and ΔET are relatively uncertain in the tropics compared to other land regions (Collins et al., 2013, Kooperman et al., 2018 and see Fig. 1.1).

The relationship between P and ET varies from one tropical land region to another. For example P increases over the Maritime Continent and decreases over the Amazon basin in veg_{CO2}, even though ET decreases over all land regions between 15° South and North in those simulations (Skinner et al., 2017; Swann et al., 2016; Kooperman et al., 2018). Chadwick et al. (2019), Saint-Lu et al. (2019) and Kooperman et al. (2018) suggested that P over the Maritime Continent increases in veg_{CO2}, because the decrease in ET changes the local circulation such that more moisture is advected from the surrounding ocean. We will examine the response of P and ET to a decrease in stomatal conductance with warming for different regions and varying degrees of stomatal closure in Chapter 5.

In summary, stomatal closure leads to a reduction in ET, whereas changes in

the radiative transfer tend to increase ET over land regions between 15°S and 15°N. Due to the interplay between ET and P it is important to understand that including the plant physiological response in GCMs does not necessarily result in a reduction in ET. This is only true in veg_{CO2} simulations. When both radiative transfer changes and stomatal closure are taken into account, the response to CO_2 forcing will be mixed. This is due to the fact that in some regions P can increase (either through enhanced moisture advection or due to changes in the radiative transfer) and thus provide more moisture for ET. This will be further discussed in Chapter 5.

2.7 Changes in the ITCZ

The large-scale atmospheric circulation can roughly be divided into three zonal-mean[2] overturning cells in each hemisphere: The Hadley cells in the tropics, the Ferrel cells in the mid-latitudes and the polar cells in the high-latitudes. The Hadley circulation consists of ascending air in the tropics, poleward flow aloft, subsidence in the subtropics and a return flow near the surface (Hadley, 1735; Dima and Wallace, 2003; Schneider, 2006). This meridional circulation is essentially driven by stronger heating of the Earth's surface by the Sun near the Equator than towards the poles and seasonally stronger heating in one hemisphere. The Hadley circulation transports energy from the tropics into the subtropics (Pierrehumbert, 2002) and from the energetically 'richer' summer hemisphere into the 'poorer' winter hemisphere (Donohoe et al., 2013; Fasullo and Trenberth, 2008). Most of the energy transport occurs in the upper branches of the Hadley cells, whereas the lower branches transport moisture and thus mass in the opposite direction (Held, 2001; Pierrehumbert, 2002; Frierson et al., 2013). During boreal spring and autumn, the two Hadley cells straddle the Equator, but as the Sun migrates into the respective summer hemisphere, so does the ascending branch and the cells are no longer equal in size and strength (Fig. 2.3, Dima and Wallace, 2003, Gadgil, 2018).

The Intertropical Convergence Zone (ITCZ) is located roughly 2° North of the Equator in the annual mean, but migrates seasonally and on geological timescales

[2]The atmospheric circulation is not zonally uniform but shows significant longitudinal variability, and hence the zonal mean picture is an 'idealised' concept (Maher et al., 2019).

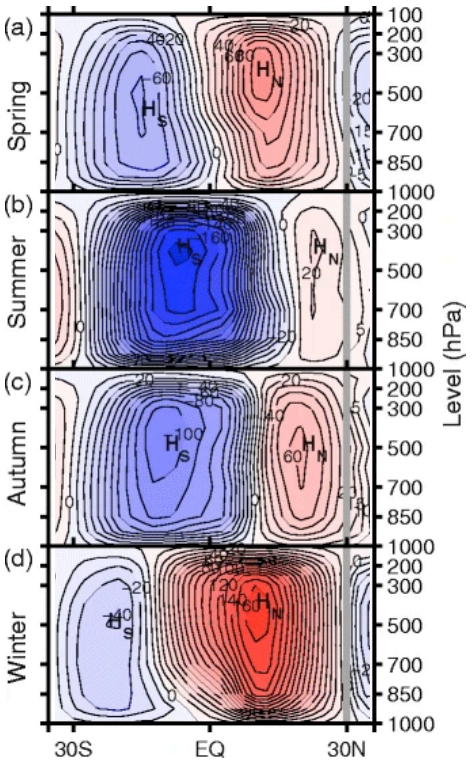

Figure 2.3: Atmospheric meridional mass streamfunction in the tropics (30°S - 30°N) showing the two Hadley cells to the south (H_S) and north (H_N) of the Equator averaged over a) March April May (MAM), b) June July August (JJA), c) September October November (SON) and d) December January February (DJF). Positive/negative contours indicate clockwise/anti-clockwise circulation (red/blue shading) and contours are spaced at 10^{10} kg/s. Based on the NCEP/NCAR reanalysis (Kalnay et al., 1996) for 1981-2010. Figure adapted from Qian et al. (2016).

(Donohoe et al., 2013). The ITCZ is co-located with the ascending branch of the Hadley circulation in the moist Equatorial region, forming a band of heavy convective rainfall (Dima and Wallace, 2003; Bischoff and Schneider, 2014). When an extra-tropical cooling (such as an ice-sheet) is applied, the ITCZ shifts away from this cooling (Broccoli et al., 2006; Peyser and Poulsen, 2008). Frierson et al. (2013) provided evidence for the importance of the northward oceanic heat transport in positioning the ITCZ in the Northern Hemisphere. Based on the energy input to the atmosphere from TOA fluxes only, the ITCZ would be expected to sit in the Southern Hemisphere which receives slightly more net radiation (Frierson et al., 2013). Thus, in a simulation where the ocean heat transport is made hemispherically symmetric, the ITCZ shifts into the Southern Hemisphere.

Byrne and Schneider (2016) showed that the majority of CMIP5 models project a narrowing and northward shift of the ITCZ with warming under the RCP8.5 scenario (comparing the end of the 21st Century to the historical period, 1976 - 2005). Upward velocities increase in the deep convecting regions close to the Equator ('deep-tropics squeeze', Lau and Kim, 2015) and decrease in the descent regions. The width of the Hadley circulation is also projected to increase, which – in combination with the narrowing of the ITCZ – results in an expansion of the descent regions in the subtropics. This narrowing of time-mean ascent

and expansion of subsidence regions results in an increase in longwave-radiative cooling through the 'dry-radiator fins' (Pierrehumbert, 1995). Therefore, climate model biases in the ITCZ width and changes thereof could potentially affect the climate sensitivity of the model.

2.8 Energetics of tropical precipitation

The moist static energy (MSE or h, in J/kg) of an air parcel is defined as

$$h = c_p T + gz + Lq \tag{2.4}$$

where c_p is the heat capacity of dry air at constant pressure ($\approx$ 1004 J/(kg $\cdot$ K), Yano and Ambaum, 2017). With $g \approx 9.81$ m/s^2 being Earth's gravitational acceleration and z denoting the geopotential height in meters, gz is the specific gravitational potential energy in m^2/s^2 or J/kg. L is the latent heat of vapourisation ($\approx 2.45 \cdot 10^6$ J/kg) and q is the specific humidity of the air in kg/kg. The sum of the first two terms is the dry static energy (s, in J/kg), which is constant for dry adiabatic processes (potential temperature $\theta = const.$). Similarly, h is conserved under moist adiabatic processes (equivalent potential temperature $\theta_e = const.$, e.g. Yanai et al., 1973).

In the annual mean (denoted by overbars), the energy budget of the atmosphere is given by

$$\int_0^{p_S} \nabla . \overline{(h+k)\mathbf{v}} \frac{dp}{g} = \overline{F_T - F_S} \tag{2.5}$$

where F_T and F_S denote the top of the atmosphere and surface net energy fluxes (in W/m^2), respectively (both positive downward), $\mathbf{v}$ is the velocity vector (m/s) and p is the pressure in hPa (e.g. Trenberth and Solomon, 1994; Neelin and Held, 1987). The vertical integral is taken between the top of the atmosphere ($p = 0$) and the surface (p_S). The flux of kinetic energy (k) is often neglected (Oort and Vonder Haar, 1976; Bischoff and Schneider, 2014). The left hand side less the kinetic energy is the vertically integrated moist static energy flux divergence (F_{MSE}, in W/m^2).

In the zonal mean (denoted by square brackets), the vertical integral of the moist static energy flux ($h\mathbf{v}$) is related to the net energy input to the atmosphere

($F_{net} = \overline{F_T - F_S}$) via

$$\frac{\partial}{\partial y} \int_0^{p_S} [\overline{hv}] \frac{dp}{g} = [F_{net}] \tag{2.6}$$

(Bischoff and Schneider, 2014; Wei and Bordoni, 2018; Neelin and Held, 1987).

In order to relate changes in surface temperatures to precipitation changes for example during El Niño events, Neelin and Held (1987) introduced the concept of gross moist stability ($\delta h = h_1 - h_2$, in J/kg), where the subscripts 1 and 2, respectively, denote the top and bottom layer in a two-layer atmosphere. Specifically,

$$\begin{aligned} h_1 &= \frac{1}{\nabla.\mathbf{v}_{h,1}} \int_0^{p_M} \overline{h} \nabla.\overline{\mathbf{v}_h} \frac{dp}{g} \\ h_2 &= \frac{1}{\nabla.\mathbf{v}_{h,2}} \int_{p_M}^{p_S} \overline{h} \nabla.\overline{\mathbf{v}_h} \frac{dp}{g} \end{aligned} \tag{2.7}$$

where p_M is the mid-tropospheric level (the boundary between the two atmospheric layers 1 and 2), above (below) which most of the poleward (equatorward) mass transport occurs (Frierson, 2007). $\mathbf{v}_h$ denotes the horizontal velocity vector and $\nabla.\mathbf{v}_{h,1}$ and $\nabla.\mathbf{v}_{h,2}$ (units of kg/(m^2·s)) are defined as

$$\begin{aligned} \nabla.\mathbf{v}_{h,1} &= \int_0^{p_M} \nabla.\overline{\mathbf{v}_h} \frac{dp}{g} \\ \nabla.\mathbf{v}_{h,2} &= \int_{p_M}^{p_S} \nabla.\overline{\mathbf{v}_h} \frac{dp}{g}. \end{aligned} \tag{2.8}$$

Combining Equations 2.7 and 2.8 and using the assumption that $\nabla.\mathbf{v}_{h,1} = -\nabla.\mathbf{v}_{h,2}$ to calculate the gross moist stability $\delta h = h_1 - h_2$, one obtains

$$\delta h = -\frac{\int_0^{p_S} \overline{h} \nabla.\overline{\mathbf{v}_h} \frac{dp}{g}}{\int_{P_M}^{p_S} \nabla.\overline{\mathbf{v}_h} \frac{dp}{g}} = -\frac{\int_0^{p_S} \overline{h} \nabla.\overline{\mathbf{v}_h} \frac{dp}{g}}{\nabla.\mathbf{v}_{h,2}} \tag{2.9}$$

δh is a measure for the efficiency of the large-scale circulation to transport energy (Geen et al., 2020; Inoue and Back, 2015; Raymond et al., 2009). The gross moist stability is usually denoted as Δh (Neelin and Held, 1987) or Δm (e.g. Seo et al., 2017, Kang et al., 2009). Since Δ is reserved for changes between the perturbed and control climate in this thesis (e.g. ΔP for precipitation changes), we denote the gross moist stability as δh.

The gross moist stability can also be expressed in terms of energy and mass transports rather than their divergences (Wei and Bordoni, 2018; Frierson, 2007;

Seo et al., 2017) as

$$\delta h = \frac{\int_0^{p_S} \overline{h\mathbf{v}_h} \frac{dp}{g}}{\int_0^{p_M} \overline{\mathbf{v}_h} \frac{dp}{g}} \tag{2.10}$$

or in the form of 'normalised gross moist stability' as

$$NGMS = \frac{\int_0^{p_S} \nabla.(\overline{h\mathbf{v}_h}) \frac{dp}{g}}{\int_0^{p_S} \nabla.(\overline{s\mathbf{v}_\mathbf{h}}) \frac{dp}{g}} \tag{2.11}$$

i.e. the moist static energy flux divergence divided by the dry static energy flux divergence vertically integrated over the entire column (Inoue and Back, 2015; Raymond et al., 2009).

Applying the Reynolds decomposition (e.g. Peixoto and Oort, 1992, p. 324) to Equation 2.5

$$F_{MSE} = \int_0^{p_S} \nabla.\overline{(h\mathbf{v})} \frac{dp}{g} = F_{net} \tag{2.12}$$

and assuming that vertical velocities at $p = 0$ and p_s are zero leaving only the horizontal velocity vector $\mathbf{v}_h$, the time-mean moist static energy flux divergence can be split into

$$\nabla.\overline{(h\mathbf{v}_h)} = \nabla.(\overline{h}\overline{\mathbf{v}_h} + \overline{h'\mathbf{v}'_h}) = \overline{h}\nabla.\overline{\mathbf{v}_h} + \overline{\mathbf{v}_h}.\nabla\overline{h} + \nabla.(\overline{h'\mathbf{v}'_h}). \tag{2.13}$$

Primed quantities are deviations from the time mean (i.e. transients). Dropping the transients and $\overline{\mathbf{v}_h}.\nabla\overline{h}$ from $F_{net} = \int_0^{p_S} \nabla.\overline{(h\mathbf{v}_h)} \frac{dp}{g}$, Neelin and Held (1987) obtained

$$-\delta h \nabla.\mathbf{v}_{h,2} \approx F_{net} \tag{2.14}$$

(comparing Eq. 2.9 to Eq. 2.12). In order to justify that $\overline{\mathbf{v}_h}.\nabla\overline{h}$ and $\nabla.(\overline{h'\mathbf{v}'_h})$ can both be neglected, the moist static energy is split into the contribution from dry static energy and latent heat ($h = s + Lq$). Neelin and Held (1987) argued that the advection of dry static energy ($\mathbf{v}_h.\nabla s$) can be neglected in the tropics, where gradients of temperature and geopotential height are small (due to the weak-temperature-gradient approximation, see Section 2.4). The advection of latent heat ($L\mathbf{v}_h.\nabla q$) can be neglected because the moisture field has larger spatial scales than the mean flow (Neelin and Held, 1987). For the assumption that the dry static energy eddy term ($\nabla.s'\mathbf{v}'_h$) can be neglected, Neelin and Held (1987)

referred to Oort (1983), and for neglecting the latent heat transport by eddies ($\nabla.q'\mathbf{v}'_h$) to personal communication on GCM moisture budgets with N. C. Lau.

Equation 2.14 states that in the tropics, the time-mean energy input to the atmosphere is balanced by low-level wind convergence (-$\nabla.\mathbf{v}_{h,2}$) and horizontal structure in the gross moist stability field (δh). Neelin and Held (1987) further pointed out that rainfall is expected to be strong in regions of large low-level convergence, and that δh is small there. According to this relationship, precipitation could be expected to peak where F_{net} – and equivalently F_{MSE} (Eq. 2.12) – have their maxima. In addition, if δh is constant, changes in the net energy input to the atmosphere can be expected to be proportional to changes in low-level convergence and thus – provided there is enough moisture available – precipitation.

Whether δh is small in the unperturbed climate and more importantly whether changes in δh can be neglected following a climate perturbation – and thus ΔP be related directly to ΔF_{net} – can not be universally answered. On the one hand, Neelin and Held (1987) discussed that most of the horizontal structure in low-level convergence must be due to δh for example during an El Niño year, because F_{net} anomalies have much larger spatial scales than $\nabla.\mathbf{v}_{h,2}$. By assuming that δh is dominated by surface temperatures, the authors provided a parameterisation of precipitation on the basis of SSTs both in the climatology and for El Niño events. More recently, Seo et al. (2017) and Wei and Bordoni (2018) showed that δh is not constant in aquaplanet simulations with a doubling of CO_2 and on sub-seasonal timescales.

On the other hand, several studies have successfully shown that the atmospheric energy budget and changes thereof are related to tropical P and ΔP, respectively. Kang et al. (2008) showed that the latitude of the so-called 'Energy Flux Equator' (ϕ_{EFE}), at which the northward moist static energy transport is zero (i.e. changes sign from southward to northward)

$$\left(\int_0^{p_S} [\overline{hv}] \frac{dp}{g} \right)_{\phi_{EFE}} = 0 \tag{2.15}$$

is a good indicator of the ITCZ location, at least close to the Equator (Bischoff and Schneider, 2014; Wei and Bordoni, 2018). By expanding Equation 2.15 to first order around the cross-equatorial flux and using Equation 2.6 evaluated at the Equator, Bischoff and Schneider (2014) obtained following expression for the

ITCZ latitude (ϕ_{ITCZ})

$$\phi_{ITCZ} = -\frac{1}{a}\frac{\left(\int_0^{p_S}[\overline{hv}]\frac{dp}{g}\right)_0}{[F_{net}]_0} \tag{2.16}$$

where the subscript 0 denotes quantities evaluated at the Equator, and a is Earth's radius. The authors found that this relationship between the ITCZ latitude and the cross-equatorial energy transport and net energy input to the equatorial atmosphere adequately predicts the response of the ITCZ location to global and tropical warming. Using coupled climate models and mixed-layer ocean experiments with continents, Donohoe et al. (2013) and Frierson and Hwang (2012) showed that the meridional atmospheric energy transport is indeed anti-correlated with shifts in the ITCZ under a doubling of CO_2, thus indirectly showing that changes in the gross moist stability can be neglected (Seo et al., 2017).

These studies on the relationship between the ITCZ latitude and the atmospheric energy budget suggest that P and ΔP can in fact be related to F_{MSE} (or F_{net}) and changes thereof, albeit not in all situations (e.g. 2xCO_2 in an aquaplanet, Seo et al., 2017). The relationship between ΔP and ΔF_{net} (or ΔF_{MSE}) will be examined in Chapter 6.

2.9 Monsoons

This section provides a brief overview of summer monsoons and the associated atmospheric dynamics, but is far from complete since the topic is extensive. Summer monsoon regions are commonly defined as having stronger summer than winter precipitation[3] and a seasonal reversal of the surface winds (Geen et al., 2020; Gadgil, 2018).

Historically, summer monsoons were seen as a large-scale land-sea breeze phenomenon caused by the different thermal inertia of land and ocean (Halley, 1687, pp.167). According to this theory, during the summer months – when the land is warm relative to the sea – moisture is drawn in to the region leading to strong rainfall. However, recent studies have shown that monsoon-type be-

[3] In the definition by Wang and Ding (2006), summer precipitation exceeds winter precipitation by 180 mm in a monsoon region.

haviour is observed in aquaplanet simulations with a sufficiently shallow mixed-layer ocean, despite the absence of land (Bordoni and Schneider, 2008). Hence, new theories of monsoons have started emerging during recent decades and are still being developed today (Hill, 2019).

One novel perspective – which can be traced back to Blandford (1886)'s analysis of the Indian monsoon – is that summer monsoons are local manifestations of the migration of the ITCZ over land (Hill, 2019; Geen et al., 2020; Bordoni and Schneider, 2008). The seasonal migration of the ITCZ (and equivalently the ascending region of the Hadley circulation) is in turn driven by the seasonal migration of the Sun (Gadgil, 2018). Around equinox, two weakly circulating cells straddle the Equator (Dima and Wallace, 2003). As the Sun migrates into the summer hemisphere, a solsticial circulation regime evolves which consists of one strong and one weak cell. The strong cell has its upwelling branch in the summer hemisphere and its descending branch in the winter hemisphere. The cross equatorial cell exports MSE from the summer hemisphere to the winter hemisphere, leading to strong rainfall in the ascending regions (Geen et al., 2020; Wei and Bordoni, 2018). The transition from the equinoctial to the solsiticial circulation regime occurs rapidly, and is associated with a reversal in the near-surface MSE gradient (Bordoni and Schneider, 2008).

Privé and Plumb (2007) showed that the ascending region of the Hadley circulation – and thus the ITCZ – is co-located with or slightly equatorward of the 'subcloud' (or near-surface) MSE ('MSE_b'). We will apply this energetic perspective of the monsoons to one of our idealised simulations in Chapter 6 in order to understand seasonal rainfall and poleward migration of the tropical rain band over land versus ocean.

Chapter 3

Methods

3.1 Isca - An overview

This section provides an overview of the Atmospheric General Circulation Modelling framework 'Isca' (Vallis et al., 2018), which is used for all experiments in this thesis. Isca is a very versatile framework which uses the Flexible Modeling System (FMS, https://www.gfdl.noaa.gov/fms/) software infrastructure from the Geophysical Fluid Dynamics Laboratory (GFDL). The model is written in Fortran and is configured using Python scripts. Isca is publicly available on GitHub (https://github.com/ExeClim/Isca).

Like all Atmospheric GCMs, a model designed with Isca is a numerical representation of a planet's atmosphere, while ocean dynamics are not modeled. The state of the atmosphere is calculated at each grid cell for each time step by solving the primitive equations[1]. The model has a spectral dynamical core and the equations are solved in spherical coordinates on sigma pressure levels (Vallis et al., 2018) thus following bottom topography, i.e. pressure p is normalised by surface pressure p_s via $\sigma = p/p_s$.

Various options concerning the configuration of the atmosphere, ocean and land are available in Isca. Earth-like configurations range from aquaplanets (Geen et al., 2018, 2019), via idealised continental shapes (this thesis and Laguë et al., 2020) to realistic continents with topography (Geen et al., 2018; Thomson and

[1] These are the continuity equation (conservation of mass), horizontal momentum equations and hydrostatic balance equation (momentum conservation), and the thermodynamic equation (conservation of energy).

Vallis, 2019; Jiménez-Esteve and Domeisen, 2019). Due to its flexible configuration, Isca can also be used to design models of other planetary atmospheres, such as those of Mars or Jupiter (Thomson and Vallis, 2019) by changing orbital parameters, size and mass of the planet and using appropriate radiation schemes. Penn and Vallis (2018) used Isca to study the atmosphere of terrestrial exo-planets with varying rotation rates.

Even using the most realistic options available, an Atmospheric GCM designed with Isca is still considered an 'idealised' model. While parameterisations are used in all GCMs in order to represent sub-grid scale processes which need to be included but can not be resolved (Schneider and Dickinson, 1974), several of the parameterisations used in Isca are simplified compared to those used in complex GCMs. For example, state-of-the-art Earth System Models include land models which have dynamic vegetation meaning that as climatic conditions change, so do the plant functional types populating a grid cell, affecting carbon, energy and water fluxes between the surface and the atmosphere (Clark et al., 2011; Best et al., 2011). In those models, leaf-scale processes such as respiration and the effect of ozone on leaf photosynthesis are parameterised (Clark et al., 2011). In contrast, the most complex land-surface scheme included in Isca so far is the 'bucket hydrology' by Manabe (1969) (see Section 3.2), which was used in the first generation of land surface models in the 1970s (Bonan, 2008). In this scheme, evaporation from a land grid-cell is parameterised based on the availability of soil moisture. Another idealisation in Isca is that the framework currently does not yet include a cloud scheme. Several convection parameterisations and radiation schemes are available in Isca, ranging from highly idealised to more realistic (see Section 3.3). The benefits of using an idealised Atmospheric GCM instead of a comprehensive one will be discussed in Section 3.5.

The ocean is represented by a non-dynamical mixed-layer ('slab') of specified depth (i.e. heat capacity) and albedo. In this thesis, where a slab ocean is used the ocean depth is set to 20m (e.g. in Chapter 6). In order to obtain a realistic planetary albedo in the absence of clouds the ocean albedo is set to $\alpha_{oc} = 0.25$, which is relatively bright compared to the real ocean albedo of $\alpha_{oc} < 0.1$. Instead of the responsive slab ocean, a climatology of sea surface temperatures (SSTs) can be prescribed (e.g. in Chapters 4 and 5). In this thesis, the prescribed SSTs are usually a zonally uniform climatology derived from the observation-

based Atmospheric Model Intercomparison Project (AMIP, Gates, 1992) SSTs, with the annual-mean temperature maximum located to the North of the Equator (Fig. 3.1). At the more realistic end of Isca's modelling spectrum, the user has the option to add a parameterisation of horizontal ocean heat transports to the slab ocean. These ocean heat transports are derived from a given SST distribution (see Section 3.4). This option will be used briefly in Chapter 4.

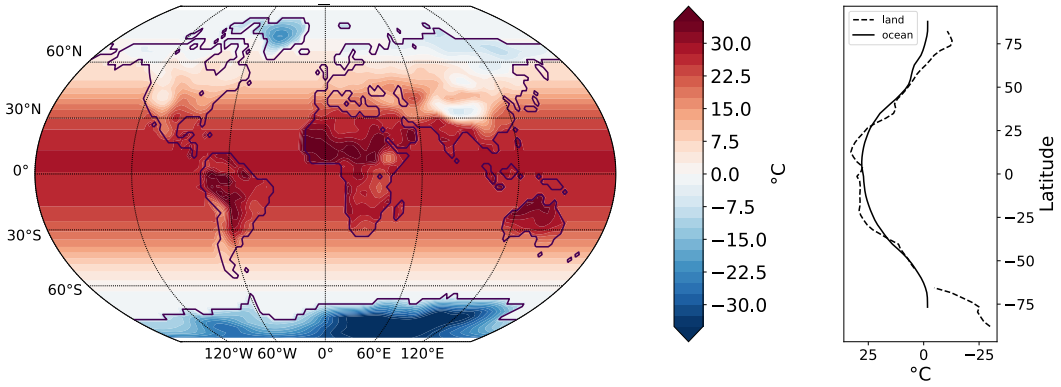

Figure 3.1: Annual mean surface temperatures when the zonally uniform SST climatology derived from AMIP is prescribed, plotted here with realistic continents. The panel on the right shows zonal mean surface temperatures over ocean (solid) and land (dashed).

Land can be represented at varying levels of complexity, the simplest option being a continent of idealised shape, lower heat capacity (i.e. shallower mixed-layer depth) and limited evaporation compared to the ocean. As discussed above, realistic continents with or without topography are available in Isca. As on Earth, the albedo of a land surface will generally be set to be higher than that of the ocean. In most simulations in this thesis, the land is 1.3 times brighter than the ocean, comparable to dark soil or forest on Earth. The heat capacity of the land is typically equivalent to a 2m deep slab ocean throughout this thesis, and in the interest of simplicity, the surface roughness over land is the same as the ocean in all simulations, with a roughness length of $2 \cdot 10^{-4}$ m.

3.2 Parameterisation of Evaporation

In Isca, evaporation from the ocean surface (in kg/(m^2·s)) is parameterised by the bulk formula

$$E_{OC} = \rho \cdot C_D \cdot |\mathbf{V}| \cdot (q_S^* - q) \tag{3.1}$$

where ρ is the density of the atmosphere (units of kg/m^3), C_D is the unitless drag coefficient which depends on the surface roughness, $|\mathbf{V}|$ is the magnitude of the velocity (in m/s) and q is the specific humidity (in kg/kg) – all in the lowest model layer (Vallis et al., 2018; Manabe, 1969). The saturation specific humidity at surface temperature is given by q_S^*. Land surface evaporation is parameterised as

$$E_L = C_L \cdot E_{OC} \tag{3.2}$$

where C_L is a unitless factor which represents moisture conductance by the soil. The simplest approach is to set C_L to a constant value (e.g. Voigt et al., 2016). In that case, the land is essentially a shallower ocean with less evaporation (sometimes called a 'jello' continent). A constant evaporative conductance implies an infinite supply of moisture, which we find yields unrealistic precipitation changes over tropical land (see Chapter 4). Therefore, a more sophisticated method – the 'bucket model' (Manabe, 1969) – is used throughout this thesis.

In contrast to C_L = const., the 'bucket model' sets C_L depending on water availability in the soil. Soil moisture increases when P exceeds E until the soil reaches saturation, in which case the excess $P-E$ is treated as runoff. By setting $C_L = 1$ where soil moisture (W, in meters) exceeds 75% of the maximum water holding capacity of the soil (or 'field capacity', W_f) and to $C_L = W/(0.75 \cdot W_f)$ elsewhere, evaporation from land surfaces becomes increasingly difficult as the soil dries out (Vallis et al., 2018). In all of our simulations which use the bucket hydrology, the field capacity W_f is set to 0.15 m and the bucket is always initialised full.

In order to study the impact of stomatal closure on ΔP, an additional constraint on E_L is introduced to the above equation – the vegetation pre-factor (C_V, unitless). The new evaporative conductance parameter C' is therefore given by

$$C' = C_V \cdot C_L. \tag{3.3}$$

For full stomatal conductance ($C_V = 1$), the conductance parameter is simply $C' = C_L$, where C_L is calculated using the bucket model. Stomatal closure due to higher CO_2 partial pressure is represented by a decrease in C_V and thus in C'. This parameterisation of stomatal closure with increasing CO_2 will be employed in Chapter 5.

3.3 Radiation and Convection Schemes

In all simulations, the rapid radiative transfer model (RRTM) is used in which transmission of longwave (LW) and shortwave (SW) radiation through the atmosphere is wavelength-dependent due to absorption and scattering by atmospheric constituents including water vapour, CO_2, methane and ozone among others (Clough et al., 2005; Mlawer et al., 1997). This is in contrast to a grey-radiation scheme – which is also available in Isca – where the atmosphere is transparent to SW radiation and absorbs LW radiation with a prescribed, constant absorption profile (Salby, 1995; Frierson et al., 2006).

For all simulations in this thesis the simplified Betts-Miller (SBM) convection parameterisation scheme, developed by Frierson (2007), is used. Other convection schemes available in Isca include the original Betts-Miller scheme (Betts, 1986; Betts and Miller, 1986) and a relaxed Arakawa-Schubert scheme (Moorthi and Suarez, 1992), and an additional convection scheme is currently being implemented in the model. Since these schemes are not used in this thesis, they will not be discussed in detail here.

The Simple Betts Miller scheme relies on the radiative-convective equilibrium theory (RCE, Manabe and Strickler, 1964). The RCE theory derives convective mass fluxes by assuming quasi-equilibrium between radiation and vertical motions. In a static atmosphere, where no vertical motion is allowed and which is only heated from the surface upwards (i.e. SW radiation does not interact with the atmosphere), a steep lapse-rate develops. The atmosphere is in 'radiative equilibrium' but is very unstable in terms of convection. Allowing for 'convective adjustment' reduces the steepness of the lapse rate and leads to more stable conditions (Manabe and Strickler, 1964; Yano and Plant, 2012). As in other convection schemes, the SBM scheme calculates precipitation by relaxing vertical profiles of temperature and humidity towards reference profiles, but the reference profiles are simplified.

Frierson (2007) showed that using only large-scale condensation (i.e. precipitation occurs when saturation is reached) leads to grid-cell sized storms in the tropics and a tropical atmosphere that is convectively unstable. A very strong Hadley circulation develops, which is still unable to export sufficient energy from the tropics to the extra-tropics. Allowing for deep convection but no shallow con-

vection corrects some of these issues and leads to intermediate model performance, while the most realistic results are achieved when both types of convective adjustment are active.

3.4 Ocean heat transport

Isca includes scripts for deriving the ocean heat transport from a given distribution of SSTs (Vallis et al., 2018). In our case, an observation-based climatology of monthly-mean SSTs is taken from the Atmospheric Model Intercomparison Project (AMIP, Gates, 1992). This SST climatology is prescribed in a simulation with realistic continents, the bucket model (Section 3.2) and a slab ocean of 20m depth. The resulting surface energy balance is compared to the SST distribution, and a climatological ocean heat transport is derived, which distributes energy across the planet to match the prescribed SST distribution. The ocean heat transport (or 'q-flux' F_q, in W/m^2) is computed as follows (Vallis et al., 2018, following Russell et al., 1985):

$$F_q = C_m \frac{\partial T}{\partial t} - F_S \tag{3.4}$$

$$F_S = SW - LH - SH - LW \tag{3.5}$$

The mixed layer's heat capacity C_m (in units of J/(K $\cdot$ m^2)) is given by $C_m = c_p \rho_w D$, where c_p in this case is the specific heat capacity of water ($\approx$ 4000 J/(kg $\cdot$ K)), ρ_w is the density of sea water ($\approx$ 1035 kg/m^3) and D is the mixed layer depth in meters. The rate of change in mixed layer temperature ($\frac{\partial T}{\partial t}$, in K/s) is given by the respective SST climatology. The surface flux (F_S in W/m^2, positive downward) is computed from the upward latent and sensible heat fluxes (LH and SH, respectively), the net LW radiation (positive upward) and net SW radiation (positive downward) all in W/m^2. All of those components are taken from the 'prescribed SST' experiment.

While the ocean heat transport parameterisation is the same in the perturbed and in the unperturbed climate, the ocean is able to respond freely to a CO_2 forcing. The advantage of using a parameterised ocean heat transport is that it captures Earth's ocean currents such as the Gulf Stream, Kuroshyo current and cold tongue in the East Pacific (see Fig. 3.2). The option to prescribe an ocean heat transport will be used briefly in Chapter 4.

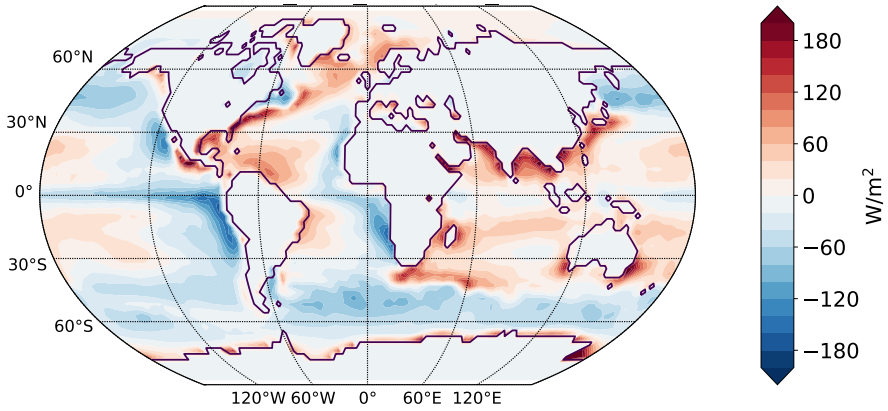

Figure 3.2: Annual mean ocean heat transport (in W/m^2) derived from AMIP for realistic continents with topography and bucket hydrology. A positive ocean heat transport (red) compensates for too little heating of the slab ocean by the surface flux from the 'prescribed-SST' run compared to the SST climatology, whereas a negative (blue) ocean heat transport effectively cools the slab ocean.

3.5 The advantage of using idealised models

One advantage of using an idealised model is that it is computationally inexpensive to run. All simulations in this thesis use T42 resolution (approximately 2.8°x2.8°) with 40 unevenly spaced vertical levels and a time-step of twelve minutes for all processes except for radiative transfer, which is calculated with an hourly time-step. In this configuration and using 16 cores, a typical simulation with the radiation and convection schemes used in this thesis (see Section 3.3) takes merely one day per ten years of model simulation.

The other major advantage is that Isca offers the possibility of designing modelling experiments of varying degrees of complexity – a 'hierarchy of models' – to bridge the gap between highly idealised simulations and comprehensive GCMs (Maher et al., 2019; Schneider and Dickinson, 1974). At the simple end of the climate modelling hierarchy, idealised models help advance our understanding of the atmosphere at a fundamental level at the expense of realism (Maher et al., 2019; Held, 2005, 2014). At the complex end of the spectrum, the development and improvement of comprehensive GCMs is motivated by the need for accurate projections of climate change (Polvani et al., 2017). GCMs are also required in order to 'validate' idealised models when performing idealised climate change simulations (Maher et al., 2019): An important requirement for idealised models

is that they capture the processes one is interested in. Geen et al. (2018) and similarly Thomson and Vallis (2019) and Jiménez-Esteve and Domeisen (2019) all included comparisons of their most realistic Earth-like Isca simulations to observations and/or reanalyses, finding sufficient model fidelity to draw conclusions about Earth's climate system from their idealised modeling results.

While complex models provide much-needed projections of climate change, they do not necessarily enhance our understanding of the climate system (Schneider and Dickinson, 1974; Polvani et al., 2017; Held, 2014). Hence idealised models or modelling frameworks of sufficient complexity to capture key features of the climate system – such as Isca – are required (Held, 2005; Polvani et al., 2017). One example of a successful application of idealised models for the understanding of complex climate processes has already been discussed in Section 2.9: Aquaplanet simulations exhibit monsoon-type behaviour, despite the absence of land-sea contrasts (Bordoni and Schneider, 2008; Geen et al., 2018; Wei and Bordoni, 2018). As a result, the theory of summer monsoons has started to shift away from the classical 'large-scale land-sea breeze' paradigm towards viewing monsoons as a regional manifestation of the ITCZ migration over land (Geen et al., 2020; Hill, 2019; Gadgil, 2018).

Another example of how idealised simulations can help elucidate processes in Earth's climate system regards the stronger warming of the polar regions compared to the low-latitudes (which was briefly mentioned at the beginning of Chapter 1). This 'polar amplification' is often associated with a positive feedback loop from warming-induced melting of sea-ice, which exposes dark ocean surfaces leading to more absorption of shortwave radiation and thus further warming. However, in a simple aquaplanet simulation in Isca, polar amplification occurs in the absence of sea-ice (Fig. 3.3), indicating that other processes (discussed by e.g. Pithan and Mauritsen, 2014 and Stuecker et al., 2018) must contribute to the amplified warming in the high-latitudes on Earth.

3.6 Experiments

In this section, the most important Isca experiments for each chapter are briefly outlined. Detailed descriptions of these and additional experiments can be found

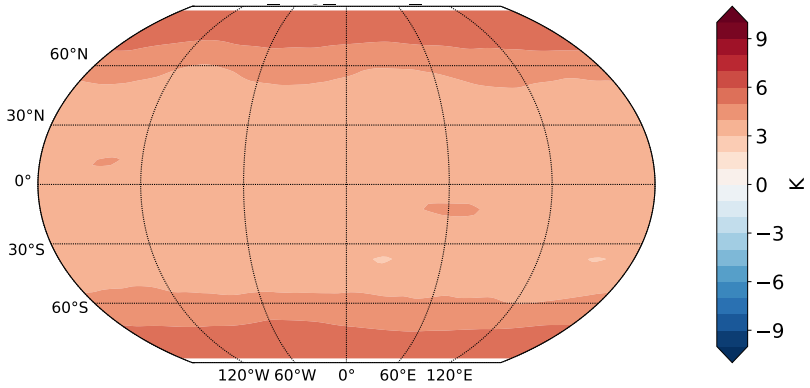

Figure 3.3: Stronger warming of the polar regions demonstrated by an aquaplanet simulation in Isca with a slab ocean of 20m depth and albedo of 0.25. The change in annual mean surface temperatures (in Kelvin) following a doubling of CO_2 from 300 to 600 ppmv is shown.

in the respective chapters. The continental configurations used in this thesis include realistic continents with and without topography, and idealised flat, rectangular continents. The idealised continents cover the whole tropical band between 30° South and 30° North and are thus hemispherically symmetric.

Rectangular continents have been the subject of several idealised modelling studies such as Chou et al. (2001), Byrne and O'Gorman (2013), Maroon et al. (2016), and the Tropical Rain belts with an Annual cycle and a Continent Model Intercomparison Project (TRACMIP, Voigt et al., 2016), to name a few. Our simulations are similar to the TRACMIP set-up with a tropical continent spanning 30° South to 30° North, albeit with the important difference that Voigt et al. (2016) used a constant soil moisture conductance (C_L = 0.5 in Equation 3.2) over land whereas we use a land surface hydrology parameterisation (either the bucket model or a simple vegetation scheme, see Section 3.2). This is because we find that a constant soil moisture conductance yields unrealistic ΔP patterns over land under a doubling of CO_2 (see Section 4.3).

The CO_2 concentration in the unperturbed climate is 300 ppm. In 'global warming' or 'doubling of CO_2' experiments, the CO_2 concentration is instantaneously increased to 600 ppm. For all experiments in this thesis, the control and perturbed simulations are run for 40 years each. Differences between the perturbed and control experiment are calculated based on the last 30 years of each experiment (years 10 to 40), discarding the first 10 years as 'spin-up' or equilibra-

tion time. Model output is saved in the form of monthly means. In this thesis, the atmospheric fields are always interpolated from σ levels to pressure levels.

In Chapters 4 and 5 we mostly prescribe a zonally uniform SST climatology derived from AMIP SSTs (Fig. 3.1). When prescribed SSTs are used, the climate is perturbed by applying a uniform ocean warming of 2.52K along with the doubling of CO_2. This warming is equivalent to the tropical-mean sea surface temperature increase averaged between 30°S and 30°N in an experiment with realistic continents and prescribed ocean heat transport (see Section 3.4), where the ocean is free to respond to the doubling of CO_2. Due to the uniform ocean warming, SSTs remain zonally uniform in the perturbed experiments. We choose to force the climate both radiatively and by uniformly increasing SSTs in order to avoid transient shifts of precipitation from land to ocean and vice versa, which would be expected whenever top of atmosphere fluxes are substantially out of balance (Lambert et al., 2011 and Section 2.4).

In Chapter 4 we start out with realistic continents and topography and prescribe the zonally uniform SST climatology derived from AMIP. The land has a heat capacity equivalent to 2m of ocean, and a 1.3 times higher albedo than the ocean (α_L = 0.33, α_{oc} = 0.25). We study ΔP under a doubling of CO_2 and uniform ocean warming of 2.52K for the bucket model and for a constant soil moisture conductance of C_L = 0.7 in Equation 3.2.

The main focus of Chapter 4 are set-ups with flat, rectangular continents representing South America (0° - 40° longitude) and Africa (80° - 140° longitude) at the distance of the Atlantic Ocean apart. Both continents span the entire tropical band (30°S-30°N). The land has the same properties as described above for the realistic continents and the bucket hydrology is used. The same SST climatology as in the realistic simulations is prescribed. We study simulations with both continents, and with the idealised American and African continent on their own.

In Chapter 5 we return to the realistic continents with topography, prescribed zonally-uniform SSTs and bucket hydrology over land. This time, the effect of stomatal closure with increasing CO_2 is parameterised (see Section 3.2). We study tropical rainfall changes with and without the parameterisation of stomatal closure under a doubling of CO_2 and uniform SST increase of 2.52K. Furthermore, we study idealised continents of varying longitudinal extent (3° - 100°) with different degrees of stomatal closure (0% - 100%) in the perturbed climate. We

also revisit the experiments with idealised Africa and America to study their sensitivities to changes in stomatal conductance.

In the last results chapter (Chapter 6), four types of surface warming are studied in order to gain a better understanding of the Matsuno-Gill theory described in Section 2.3. Starting out from an aquaplanet simulation with 20m mixed-layer depth and ocean albedo of $\alpha_{oc} = 0.25$, a patch of ocean is darkened, then replaced by a land surface, then a doubling of CO_2 is imposed to the simulation with land, and finally the land is darkened. In the above simulations, the solar insolation profile is based on the annual mean and thus resembles a 'perpetual equinox simulation' (where the insolation profile of March or September is used year-round). In an additional experiment, the seasonal migration of the ITCZ over land and ocean is studied.

Chapter 4

The presence of Africa and limited soil moisture contribute to future drying of South America

This chapter is largely based on our publication in *Geophysical Research Letters* (Pietschnig et al., 2019), although some structural changes have been made to incorporate the article into this thesis and minimise repetition in the introduction and methods sections. The simple scaling approach presented in Section 6 and Appendix A of the journal article has been omitted from this thesis, as it was mostly derived by my supervisor, Dr. Hugo Lambert. In contrast to the publication, the model output has been interpolated onto pressure levels from the model-native σ-levels, which generally makes a small difference in the absence of topography and does not change our results and conclusions. Merely Figure 4.7 is affected noticeably, albeit the interpretation stays the same. The supplementary information from the publication has been merged into the chapter, and an additional experiment with constant evaporative conductance has been included for the idealised continents, which was not part of the publication.

The key findings discussed in this chapter are

1. The limits on land-surface evaporation due to soil moisture availability contribute to the zonally asymmetric rainfall changes over Equatorial Africa (precipitation increase) and the Amazon basin (precipitation decrease) projected by complex GCMs

2. Warming-induced circulation changes over Equatorial Africa contribute to the decrease in precipitation over the Amazon basin

4.1 Introduction

Over oceans and in the zonal mean, pre-industrial patterns of precipitation (P) minus evaporation (E) generally become enhanced in a warming climate (Held and Soden, 2006), but this wet-get-wetter principle does not hold over land (see Section 2.1, Byrne and O'Gorman, 2015, Chadwick et al., 2013 and Roderick et al., 2014). Precipitation change (ΔP) is directly related to $\Delta(P - E)$, because changes in evaporation (ΔE) are relatively uniform (Held and Soden, 2006). We are particularly interested in understanding why the Amazon basin is projected to dry out whereas Equatorial Africa is likely to receive more rainfall in the future in the Coupled Model Intercomparison Project - Phase 5 (CMIP5, Taylor et al., 2012) multi-model mean, comparing 1986-2005 to 2081-2100 (Fig. 1.1 and IPCC, 2013). This response to warming cannot be understood in terms of the wet-get-wetter principle since precipitation exceeds evaporation in both regions in the current climate (Fig. 1.2, Trenberth et al., 2007, Kang and Ahn, 2015).

In contrast to the ocean, E over land does not only depend on the atmospheric moisture demand, but also on the availability of water (Manabe, 1969), which is provided by P. As a consequence, $P - E$ cannot be negative over land in the long-term mean (Byrne and O'Gorman, 2015). An initial decrease in P can reduce soil moisture, which leads to a decrease in E that can potentially further reduce precipitation. Hence, in a land-locked region that depends on continental evaporation for precipitation this feedback loop can cause said land region to dry out under global warming.

ΔP cannot solely be understood in terms of changes at the surface, because atmospheric circulation changes play an important role (Chadwick et al., 2013, 2016). The Matsuno-Gill theory of the tropical circulation presents a useful framework for understanding part of those dynamical changes (see Section 2.3). According to Gill (1980) the tropical continents can be seen as localized surface heat sources which cause convection over the continent and subsidence to the east and west. The relative humidity (r) of sinking air decreases (e.g. Charney,

1975), hence subsidence regions are associated with dry conditions (Rodwell and Hoskins, 1996), whereas ascent is associated with P. The subsidence to the east of the heat source is associated with a Kelvin wave and surface easterlies, and to the west with a Rossby wave and surface westerlies (Gill, 1980). Cook et al. (2004) utilized the Matsuno-Gill theory in order to study the teleconnection between Africa and South America in the present-day climate. The authors showed that in austral summer, heating over the African continent results in a zonal circulation with a subsiding branch over South America. This subsidence suppresses convection and P over the North-Eastern part of Brazil.

In this chapter, the zonally asymmetric ΔP features in the tropics are investigated, with a particular focus on the P decrease (here: 'drying') of the Amazon basin and P increase (here: 'wetting') over Equatorial Africa. The modeling framework 'Isca' (Vallis et al., 2018 and see Section 3) is used to design idealised Atmospheric General Circulation Models (AGCMs) with different continental configurations. In the following section, the model simulations used in this chapter are introduced, including set-ups with realistic continents and two idealised, rectangular land masses representing tropical Africa and America. The results are discussed in two sections: In Section 4.3, the contribution of soil-moisture limitations on land evaporation to the zonal asymmetries in ΔP are discussed. In Section 4.4, the impact of warming-induced circulation changes over Equatorial Africa on drying over the Amazon basin is investigated in simulations with rectangular continents. In the conclusions section, the findings from this chapter are summarised and ideas for future work presented.

4.2 Model Simulations

We use the AGCM framework Isca (Vallis et al., 2018) described in Chapter 3 to study tropical precipitation change under global warming for different continental configurations. All experiments from this chapter are summarised in Table 4.1. Experiment 'RC' has realistic continents with topography, and land evaporation is parameterised with the bucket model (Manabe, 1969) as described in Section 3.2. Experiment 'RC07' has the same continental configuration but a constant soil moisture conductance of $C_L = 0.7$ in Equation 3.2 instead of the bucket model.

For the idealised continents, we use two flat, rectangular continents representing America and Africa. Idealised America and Africa span 40° and 60° in longitude, respectively, and cover the entire tropical band in the meridional direction (30°S to 30°N). In 'AM' and 'AF', idealised America and idealised Africa, respectively, are studied in isolation. In experiment '2C', both continents are present at a distance of 40° longitude to each other, which is approximately the width of the Atlantic Ocean basin. In all simulations, the land albedo is set to 0.33, which is 1.3 times greater than the ocean albedo of 0.25.

In the control experiments, a climatology of zonally uniform SSTs derived from the Atmospheric Model Intercomparison Project (AMIP, Gates, 1992) is prescribed (see Fig. 3.1). The climate is perturbed by abruptly doubling CO_2 from 300 ppm to 600 ppm and imposing a globally uniform ocean warming of 2.52 K as discussed in Section 3.6. By using zonally uniform SSTs, the same climatology can be prescribed for the realistic and idealised continents, and nonsensical patterns avoided in the latter (Cook et al., 2004).

In order to show that ΔP in our simulation with realistic continents is relatively insensitive to SST patterns and changes thereof, and thus that our method of prescribing SSTs and applying a uniform ocean warming is appropriate, an additional experiment ('RC OHT') is conducted with parameterised ocean heat transports based on AMIP SSTs (see Section 3.4). This allows the use of a mixed-layer ocean ('slab', here with 20m mixed-layer depth), and thus for ocean temperatures to adapt freely to the doubling of CO_2, producing Δ SST patterns.

Additional experiments with realistic and idealised continents are performed where a zonally uniform SST climatology is prescribed with the annual mean temperature maximum centered at the Equator ('RC EquatorMax' and '2C EquatorMax'). This SST climatology was derived from a simulation with the two idealised continents, bucket hydrology and a slab ocean of 20m depth, where the ocean was free to respond to the doubling of CO_2.

Furthermore, a simulation is performed where the latitudinal extent of idealised America is reduced to 40° ('2C short AM') in order to be more representative of the extent of real South America. Finally, the AM, AF and 2C simulations are also performed using the constant soil moisture conductance of $C_L = 0.7$ ('AM07', 'AF07' and '2C07', respectively).

Name	Continents	Hydrology	Ocean	Perturbation
RC	realistic, topography	bucket	zon. symm. SSTs	2xCO_2 + 2.52K
RC07	realistic, topography	C_L = 0.7	zon. symm. SSTs	2xCO_2 + 2.52K
RC OHT	realistic, topography	bucket	ocean heat transport	2xCO_2 + 2.52K
AM	idealised America 30°S - 30°N, 0° - 40°E	bucket	zon. symm. SSTs	2xCO_2 + 2.52K
AF	idealised Africa 30°S - 30°N, 80° - 140°E	bucket	zon. symm. SSTs	2xCO_2 + 2.52K
2C	AM + AF	bucket	zon. symm. SSTs	2xCO_2 + 2.52K
RC EquatorMax	realistic, flat	bucket	zon. symm. SSTs annual mean max at Equator	2xCO_2 + 2.52K
2C EquatorMax	2C	bucket	zon. symm. SSTs annual mean max at Equator	2xCO_2 + 2.52K
2C short AM	AM (30°S-10°N) + AF	C_L = 0.7	zon. symm. SSTs	2xCO_2 + 2.52K
AM07	idealised America	C_L = 0.7	zon. symm. SSTs	2xCO_2 + 2.52K
AF07	idealised Africa	C_L = 0.7	zon. symm. SSTs	2xCO_2 + 2.52K
2C07	AM + AF	C_L = 0.7	zon. symm. SSTs	2xCO_2 + 2.52K

Table 4.1: Experimental set-ups used in Chapter 4 in order of their appearance.

4.3 The importance of soil moisture

Precipitation change in our simulation with realistic continents and soil moisture limitations on evaporation (Fig. 4.1a) qualitatively compares well with the CMIP5 multi-model mean (Fig. 1.1 and IPCC, 2013). Maritime P increases over the Equator and in the mid-latitudes and decreases in parts of the subtropics in our idealised model and in CMIP5. Our simulation also captures the pronounced P decrease in the tropical Atlantic to the west of Africa. Equatorial Africa (roughly between 10°S and 10°N) shows a clear precipitation increase in the complex models and our simple model. In RC, the P response over the Amazon basin is mixed, with P increasing along the Equator and decreasing to the north and south, whereas in the CMIP5 multi-model mean, P decreases in this region.

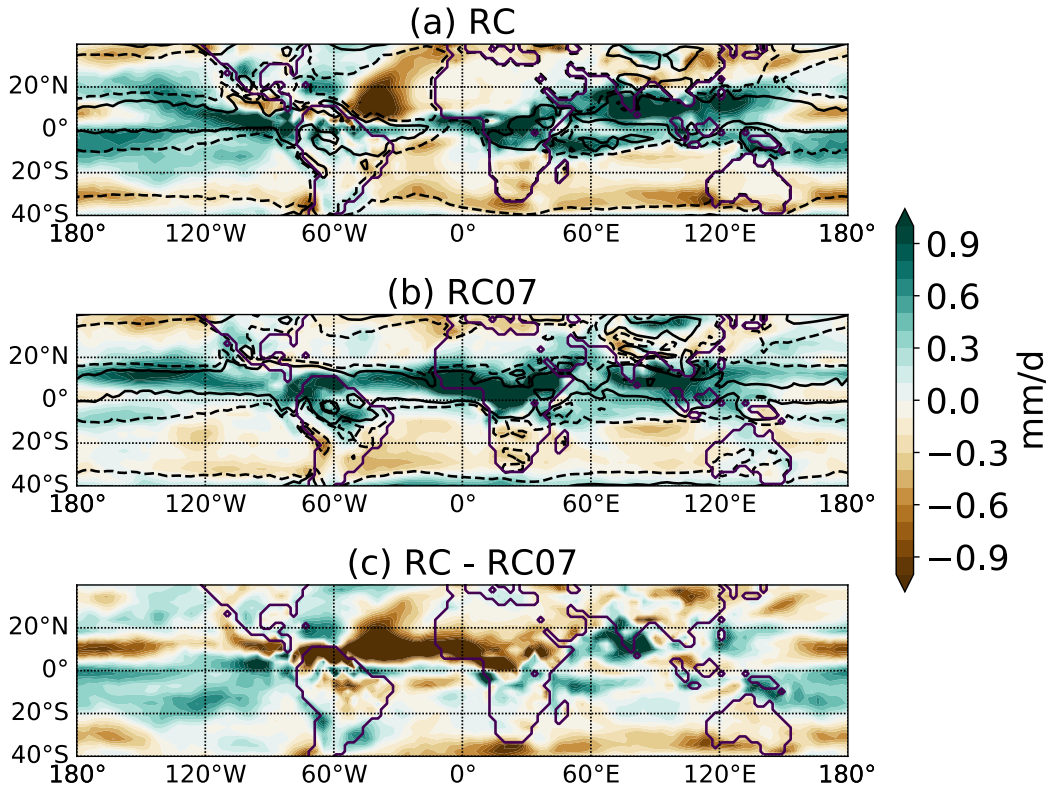

Figure 4.1: Annual mean ΔP (colours) for a) RC and b) RC07, and the difference between the two (c). Contours in (a) and (b) show -1.0 (dashed) and 1.0 (solid) $(P - E)_{ctl}$ in mm/day.

Over oceans ΔP roughly follows the wet-get-wetter principle, meaning that positive/negative ΔP coincides with positive/negative $(P - E)_{ctl}$. This is true for both our RC simulation (Fig. 4.1a) and the CMIP5 multi-model mean (Figs. 1.1

and 1.2). In contrast, over land $(P - E)_{ctl}$ rates over Equatorial Africa exceed 5 mm/day, and even 9 mm/day in the Amazon basin in our experiment, but ΔP is positive over the former and both negative and positive over the latter. Therefore, ΔP cannot be understood as a simple enhancement of $(P - E)_{ctl}$ over tropical land.

Soil moisture feedbacks cannot be neglected in the model if ΔP projections comparable to complex GCMs shall be obtained. If land evaporation is not limited by soil moisture (Fig. 4.1b), ΔP is zonally quite uniform and follows the wet-get-wetter principle over ocean and land. Large parts of South America and Africa see a stronger drying in response to warming when soil moisture is limited compared to unlimited evaporation, as shown by Figure 4.1c. This result suggests that soil moisture controls on evaporation over land contribute to the zonal asymmetry of Equatorial ΔP, with a general increase over the ocean and Africa, but a decrease over the Amazon basin.

In the CMIP5 multi-model mean, P changes over tropical land are generally quite uncertain concerning agreement among the models (Fig. 1.1, IPCC, 2013, Kooperman et al., 2018). However, the P changes mostly do exceed natural variability over tropical land. In our RC simulation, ΔP over Equatorial Africa exceeds the natural variability (Fig. 4.2). Over the Amazon basin, ΔP generally does not exceed the natural variability in our study.

The CMIP5 (RCP8.5 scenario) multi-model mean ΔP for the Amazon basin is - 0.39 mm/day and 0.16 mm/day for Equatorial Africa (Kooperman et al., 2018). In the same regions as defined in Kooperman et al. (2018), the estimates from our RC experiment are 0.24 mm/day for the Amazon basin and 0.43 mm/day for Equatorial Africa. Note that the CO_2 concentration increases from roughly 350 ppm (in 1986-2005) to about 900 ppm (2081-2100, Collins et al., 2013) in Kooperman et al. (2018) and the estimates are multi-model means, whereas our simulations are based on a doubling of CO_2 from 300 ppm to 600 ppm in a single model. Similar to our estimates, some of the CMIP5 models also predict an increase in precipitation averaged over the Amazon basin and a stronger increase over Equatorial Africa, such as IPSL-CM5A-LR, MIROC-ESM and CMCC-CESM (Kooperman et al., 2018), albeit the numbers are not directly comparable to our estimates due to the stronger forcing in CMIP5, as discussed above.

As briefly mentioned in Section 4.2, our results are not particularly sensitive to

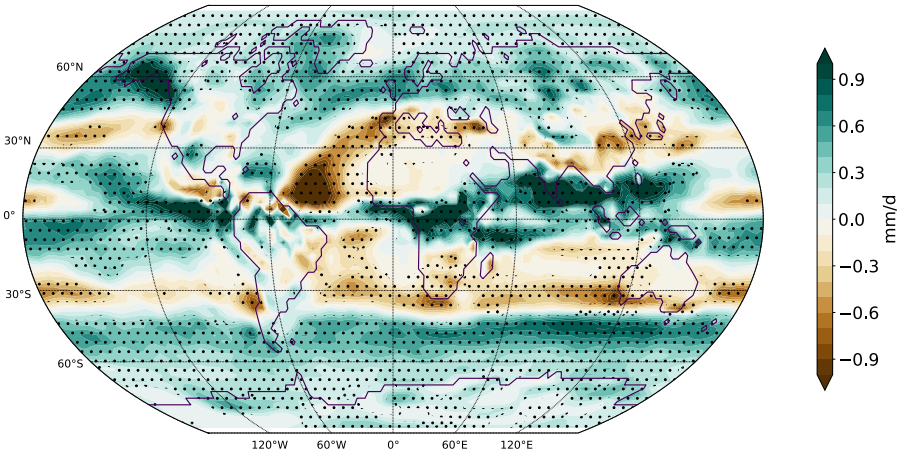

Figure 4.2: ΔP for experiment RC as in Fig. 4.1a. The stippling indicates regions where ΔP exceeds the natural variability. We consider the precipitation change in a grid-point to 'exceed the natural variability' if the time-series of annual mean precipitation in the perturbed climate is significantly different from the time-series in the control climate. We use Welch's t-test – an adaptation of Student's t-test for unequal variances (see Appendix) – to assess in which regions the two timeseries are significantly different from each other. Where the p-value of the t-test < 0.05 (indicated by the stippling), we reject the null-hypothesis that the two time-series have the same long-term mean. Note that in the desert regions of Australia and Africa and in parts of South America the results of the Welch's t-test should be interpreted with caution because the underlying assumptions of normal distribution and/or independence of the data are not strictly fulfilled (see Fig. A3).

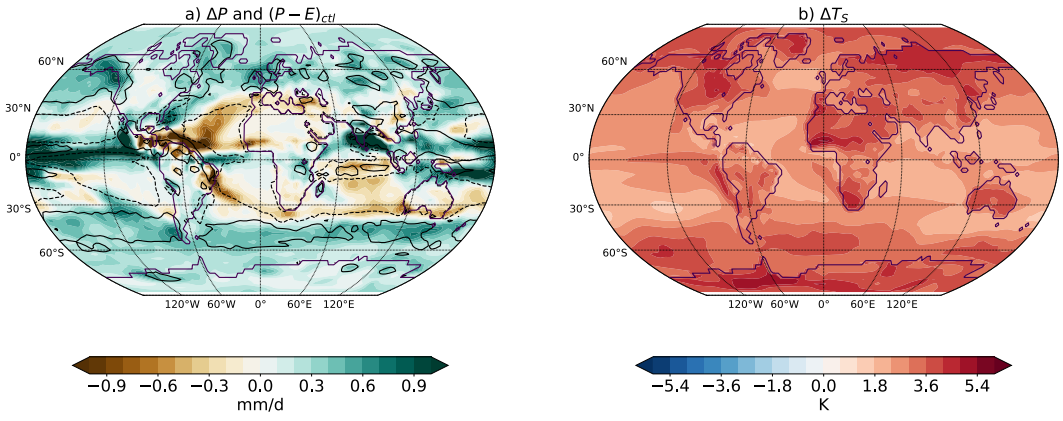

Figure 4.3: a) ΔP (colours) and $(P - E)_{ctl}$ (contours, -1.0 (dashed) and 1.0 (solid) mm/day) for the experiment RC OHT with realistic continents and topography, but with parameterised ocean heat transport. b) Changes in surface temperatures (in K), clearly with a patterned Δ SST.

patterns of ΔSST (Fig. 4.3). In the RC OHT simulation with parameterised ocean heat transport instead of prescribed SSTs, ΔSST patterns (Fig. 4.3b) roughly resemble those projected by coupled models (e.g. Chadwick et al., 2017). Nonetheless, ΔP is similar to the original RC experiment with uniform ocean warming (Fig. 4.1a). This suggests that ΔP in our simulation is not particularly sensitive to ΔSST patterns, and that our method of prescribing zonally uniform SSTs and a uniform ocean warming is suitable for studying ΔP in the tropics.

4.4 The impact of Africa on South America

Comparing our simulation with two idealised continents and bucket model (Fig. 4.4c) to our realistic simulation (RC, Fig. 4.1a) we find that the patterns of ΔP show a striking similarity between the idealised and realistic experiment. In both simulations, there is a clear P increase over Equatorial Africa and a P decrease over America south of the Equator (the 'idealised Amazon basin'). Furthermore, 2C also captures the strong decrease in P over the subtropical Atlantic. Note that the asymmetry in ΔP between the Northern and Southern Hemisphere – for example the stronger increase in P over the ocean at about 10° North compared to 10° South, and stronger drying over idealised America to the south of the Equator in 2C – is related to the fact that the prescribed SST climatology is hemispherically asymmetric. This will be discussed in more detail below (see Fig. 4.9).

The fact that RC and 2C show such similar behaviour is an important finding in itself, as it suggests that most of the tropical ΔP is caused simply by the presence of two large land masses at the appropriate distance to each other and the soil moisture limits on evaporation discussed in the previous section. Furthermore, the comparability of the ΔP patterns in 2C and RC indicates that studying the idealised continents can shine a light on the more complex, realistic continent experiment and thus help us understand tropical precipitation change in coupled climate models.

Each individual continent experiences an increase in P in the Equatorial region (10°S-10°N, Fig. 4.4a and b). However, if both continents are present (Fig. 4.4c), the idealised Amazon basin experiences a widespread decrease in P with

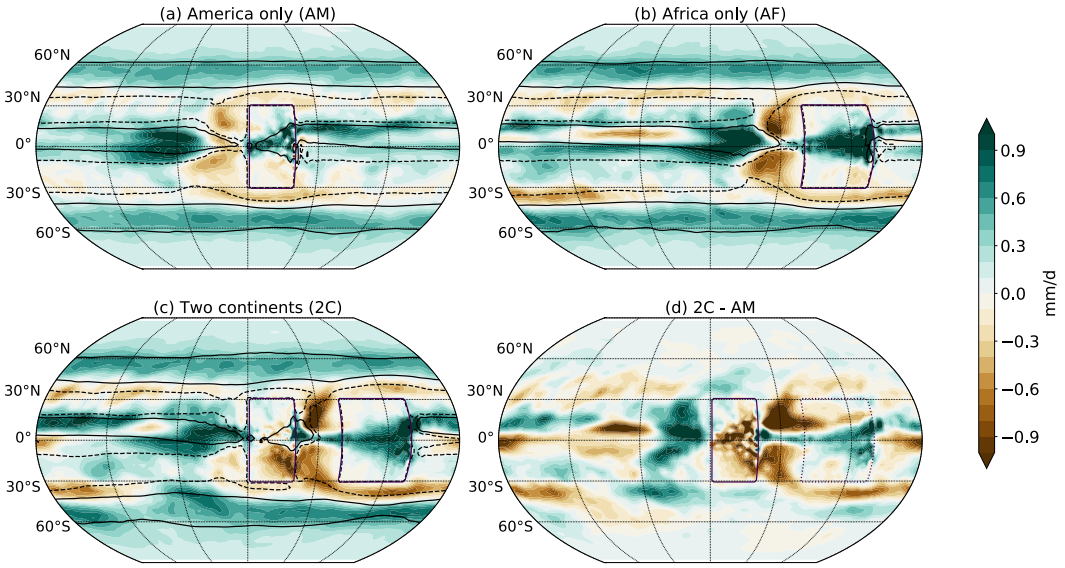

Figure 4.4: Annual mean ΔP for the idealised experiments: (a) AM, (b) AF and (c) 2C-AM, and the difference between 2C and AM (d). Contours show $(P - E)_{ctl}$ values of -1.0 (dashed) and 1.0 (solid) mm/day. The rectangles show the locations of the idealised continents, with the dotted contour in (d) indicating the removal of the African continent from 2C.

warming. The drying over the Atlantic Ocean also appears to be strongly linked to the presence of Africa, since no drying occurs there in the AM experiment. The difference between 2C and AM (Fig. 4.4d) highlights the drying impact of idealised Africa on America. This suggests that the presence of the African continent has an impact on ΔP over the idealised Amazon basin. Since ΔP in 2C is similar to ΔP in the simulation with realistic continents, we infer that the projected P decrease over the Amazon basin in complex GCMs might also be partly caused by the presence of Africa.

In order to understand how the presence of idealised Africa can impact precipitation changes over idealised America, changes in the atmospheric circulation in the Equatorial region are investigated (Fig. 4.5). Individually, each continent experiences increased ascent with warming and anomalous subsidence to the west but also to the east (Fig. 4.5a and b). Regions of anomalous descent are associated with decreases in r and P. The opposite is true for regions of stronger ascent. In the absence of Africa, idealised Equatorial America experiences only its own enhancement of ascent and thus an increase in P. When both continents

are present (Fig. 4.5c), the convection increase over idealised Equatorial America is suppressed by the subsidence associated with the circulation anomaly over Equatorial Africa (Fig. 4.5d). Anomalous convection over idealised Africa thus leads to subsidence over idealised America and a decrease in r, suppressing convection and rainfall in the Equatorial region.

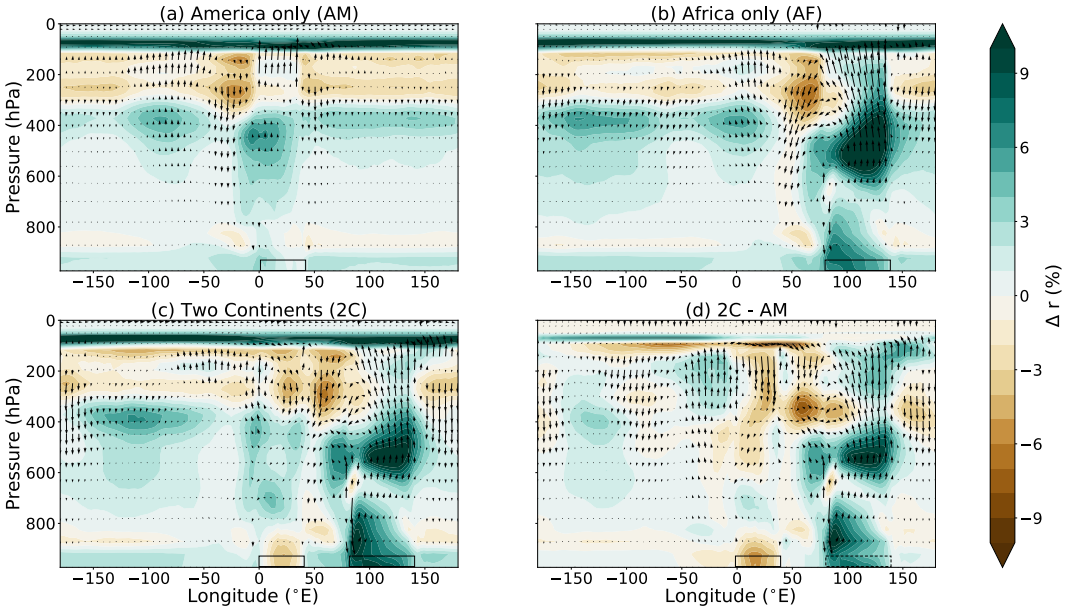

Figure 4.5: Warming-induced changes in r (colours, in absolute %) and the zonal circulation (vectors, in m/s) averaged over the Equatorial region (10°S - 10°N) for each idealised experiment: a) AM, b) AF, c) 2C and the difference between 2C and AM (d). The boxes show the locations of the continents. The change in the vertical velocity has been amplified by a factor of 8000 following Nie et al. (2010)

Warming-induced increases in near-surface specific humidity (q) over idealised Equatorial America and the Atlantic Ocean are also reduced in 2C compared to AM (see Fig. 4.6). This indicates that – due to the anomalous subsidence caused by enhanced ascent over Equatorial Africa – the air close to the surface is drier over the Atlantic Ocean than in the absence of idealised Africa. This drier air is then advected from the region of anomalous subsidence over the Atlantic Ocean onto the idealised American continent, ultimately resulting in a decrease in precipitation with warming. Cook et al. (2004) provided evidence for a similar teleconnection in the present-day climate.

The warming-induced ascent over idealised Africa, which leads to subsidence over idealised Equatorial America, can be understood in terms of the Matsuno-

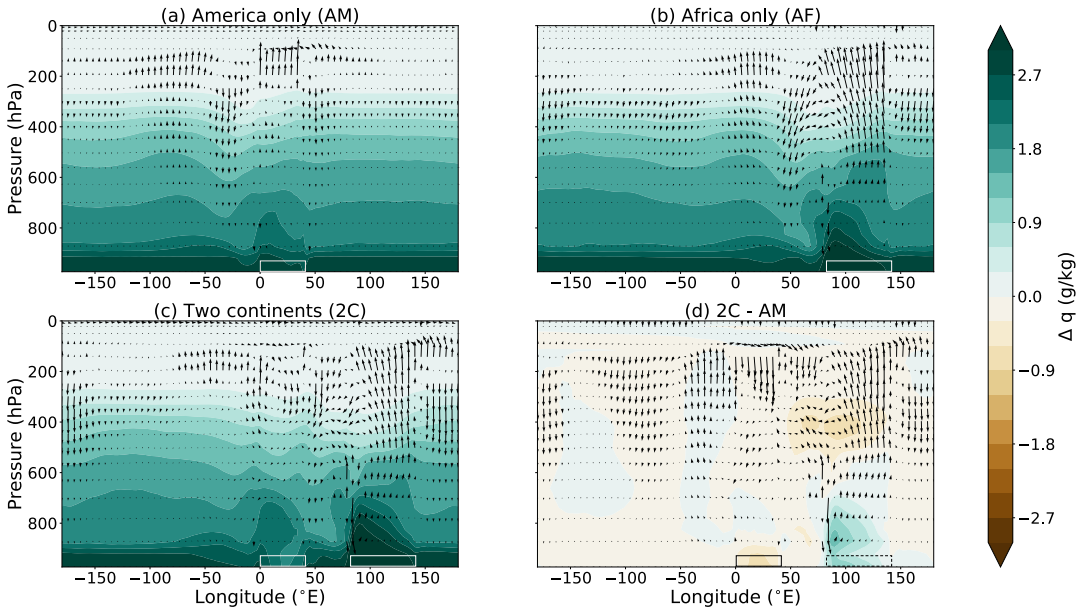

Figure 4.6: As in Figure 4.5 but here colours show changes in specific humidity (q, here in g/kg).

Gill circulation (Fig. 4.7). As expected from the theory, there is a clear warming-induced Rossby-wave response over western idealised Africa, consisting of a weak cyclone pair near the surface and a strong anti-cyclone pair aloft. According to the theory and as shown in Figs. 4.4 and 4.5, the Rossby-wave response is associated with subsidence and drying to the west of idealised Africa.

The idealised African continent is relatively insensitive to the presence of idealised America (Fig. 4.8). This is also indicated by the fact that rainfall and circulation anomalies in the Equatorial region are almost the same in 2C as in AF (comparing panel c to b in Figures 4.4 and 4.5). The fact that the influence of America on Africa is smaller than the other way around (Fig. 4.4d) has been explained for the present-day climate by Cook et al. (2004): The anomalous ascent over the continent leads to descent primarily to the west of the continent. The heating-induced low-level convergence over the continent leads to deceleration of the easterlies on the west side of the continent. This reduces wind speeds and surface heat fluxes, leading to a cooler lower atmosphere and favorable conditions for descent. To the east of the continent, the prevailing easterly winds are enhanced by the low-level convergence towards the continent. This leads to stronger heating of the lower atmosphere through surface heat fluxes and thus unfavourable conditions for subsidence to the east of the continent.

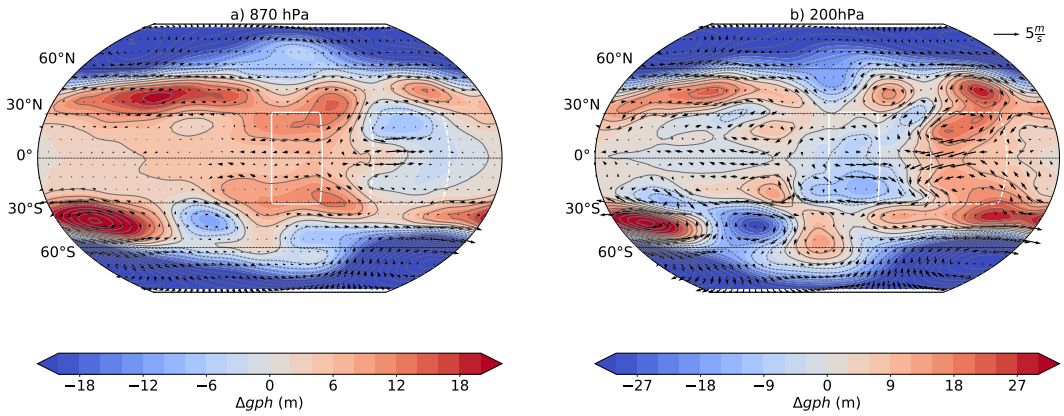

Figure 4.7: Warming-induced changes in the a) 870 hPa and b) 200 hPa geopotential height (gph, colours and contours) for 2C minus AM. Blue colours depict a decrease, red colours an increase in gph. The vectors show the change in the horizontal wind field at respective pressure levels, roughly following geostrophic balance (i.e. perpendicular to the pressure gradient). The white contours show the position of the continents (solid for America which is present in both experiments, dotted for Africa which is only present in 2C but not in AM).

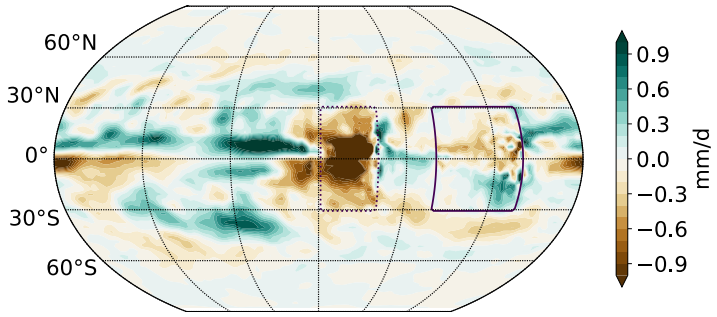

Figure 4.8: ΔP (colours) for the idealised continents (2C) minus Africa alone (AF), to show the influence of America (dashed contour) on Africa (solid contour).

As discussed earlier, ΔP in our simulation with realistic continents and topography is relatively insensitive to changes in SST patterns (Fig. 4.3), and thus prescribing zonally uniform SSTs and imposing a uniform ocean warming has been deemed an appropriate approach. However, rainfall changes do appear to be sensitive to the meridional distribution of the zonally uniform SSTs, both for the realistic and the two idealised continents. In the 'EquatorMax' simulations, where the annual mean SST maximum is centered at the Equator, precipitation increases along the Equator over South America and its idealised equivalent, and there is no clear decrease in precipitation in the idealised and realistic Amazon

basin (Fig. 4.9). Both experiments suggest that the drying over the Amazon region could be connected to the displacement of the SST maximum to the North of the Equator on Earth.

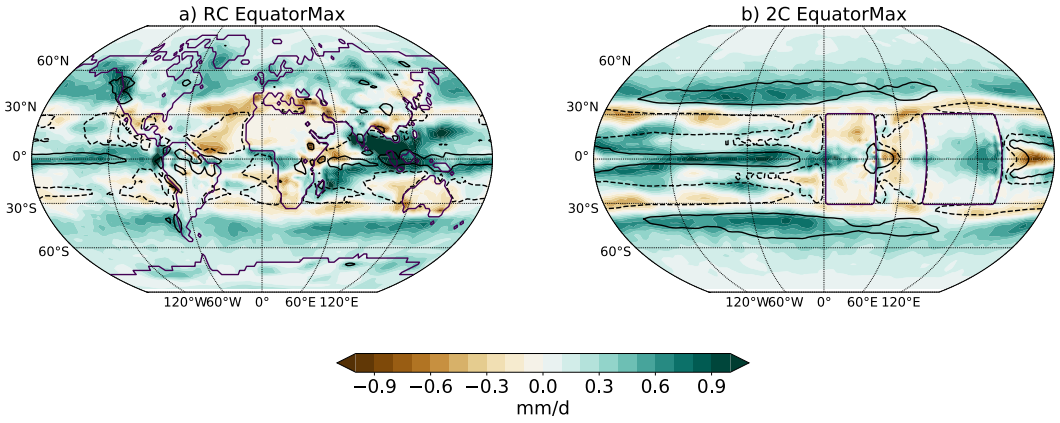

Figure 4.9: ΔP (colours) and $(P-E)_{ctl}$ (contours, -1.0 (dashed) and 1.0 (solid) mm/day) with the annual mean SST maximum located at the Equator for a) realistic continents with topography and b) the idealised two continents.

In our set-up, the continents are hemispherically symmetric with a constant width across the entire tropical band. This is appropriate for the representation of tropical Africa, but South America only extends to about 10°N, northward of which the continental width is very small. The '2C short AM' experiment is closer to realistic continents, but is not hemispherically symmetric which adds another level of complexity to the simulation. Despite the shorter American continent, precipitation decreases over the idealised Amazon basin and increases over Equatorial Africa in 2C short AM (Fig. 4.10), similar to our original 2C experiment (Fig. 4.4c). Therefore, our original 2C set-up is deemed appropriate in order to keep the simulation as simple as possible, but as complex as necessary to capture the ΔP features we are interested in.

Similar to the realistic continents with topography (Fig. 4.1b), a constant soil moisture conductance over land leads to a zonally uniform precipitation response to warming for the idealised continents (Fig. 4.11c). In contrast to the simulations with bucket hydrology (Fig. 4.4), the strong rainfall increase over Africa does not have a drying influence on idealised South America (Fig. 4.11d). This finding is surprising in the sense that idealised America is somewhat passive in the mechanism described above, where enhanced ascent over idealised Africa leads to subsidence and drying over idealised America.

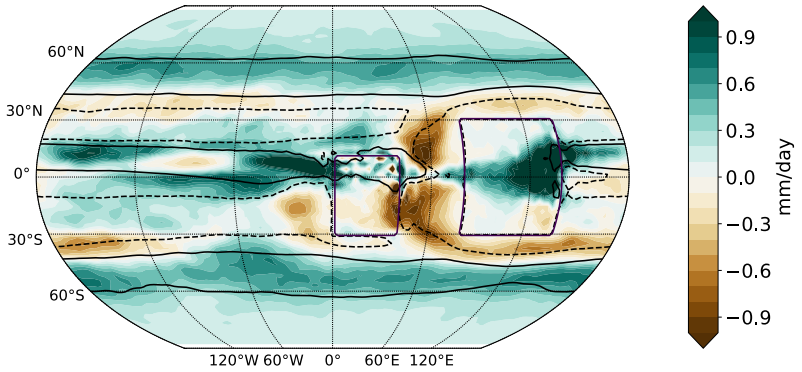

Figure 4.10: ΔP (colours) and $(P-E)_{ctl}$ (contours, -1.0 (dashed) and 1.0 (solid) mm/day) for 2C short AM, a similar set-up as 2C but with a shorter latitudinal extent on the idealised American continent (30°S-10°N).

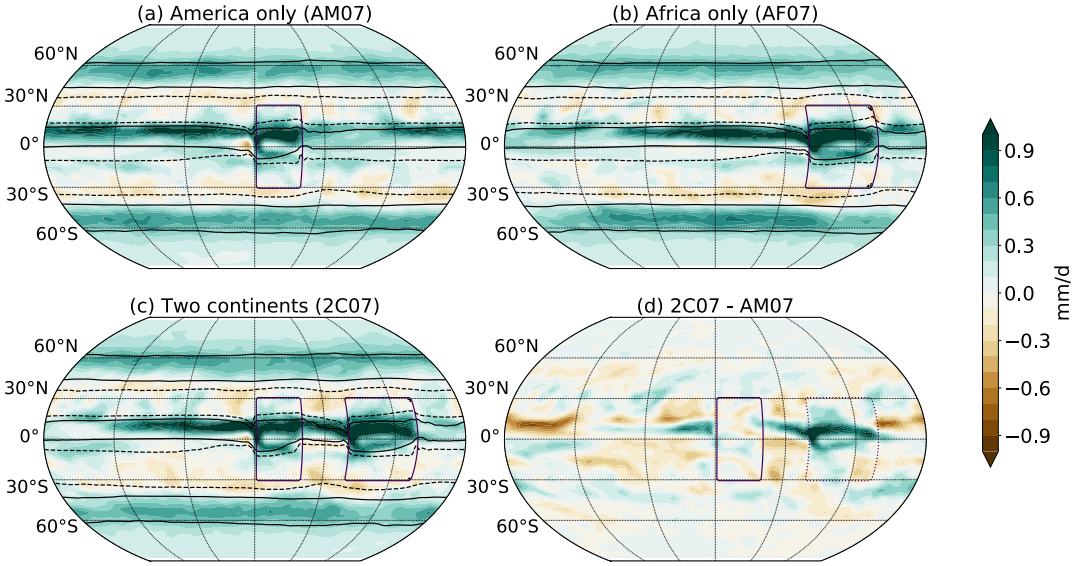

Figure 4.11: ΔP (colours) and $(P-E)_{ctl}$ (contours, -1.0 (dashed) and 1.0 (solid) mm/day) for the idealised continents with a constant soil moisture conductance of $C_L = 0.7$, in analogy to Fig. 4.1.

The P increase instead of drying over the idealised Amazon basin could be due to a weaker circulation anomaly over idealised Africa and thus less subsidence to the west. The circulation anomaly over idealised Equatorial Africa is in fact weaker, which is suggested by the fact that there is no P decrease over the ocean to the west of the continent in AF07 (Fig. 4.11b), and is shown in Figure 4.12. The reason for the weaker circulation anomaly is currently unclear and merits further investigation in future work.

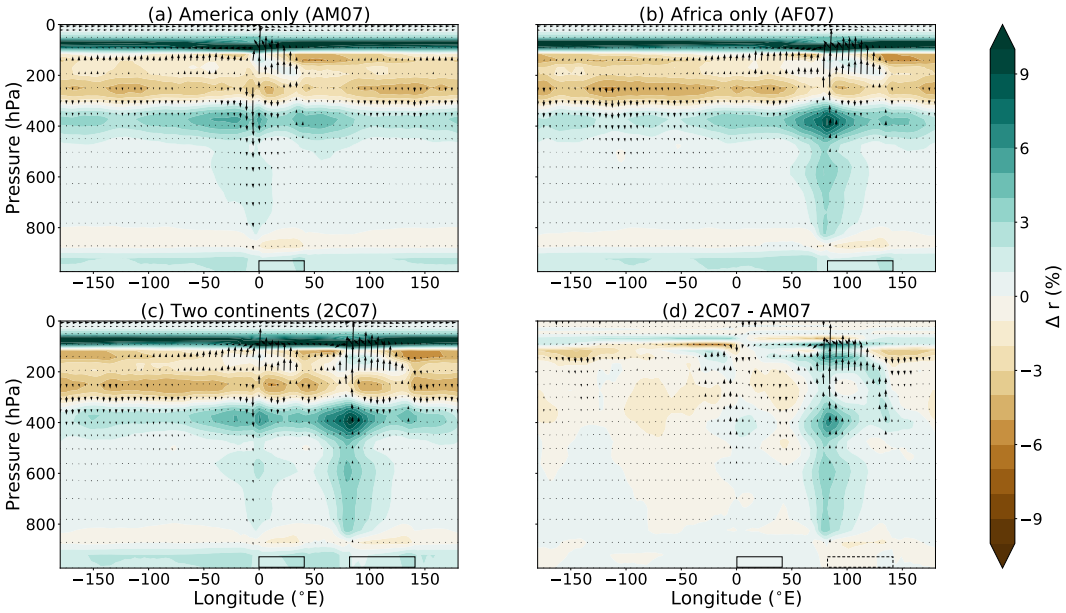

Figure 4.12: Warming-induced changes in r (colours, in absolute %) and the zonal circulation (vectors, in m/s) averaged over 10°S - 10°N for a) AM07, b) AF07, c) 2C07 and d) 2C07-AM07. The boxes indicate the locations of the continents. Just like in Figure 4.5, the change in the vertical velocity has been amplified by a factor of 8000 following Nie et al. (2010).

In addition to the weaker circulation anomaly, local effects over South America could also contribute to the P response, since evaporation over land is less constrained here than in the original experiment. Whether the idealised American continent is 'passive' or contributes actively to rainfall changes over the Amazon basin will be investigated in future work using a simulation with spatially varying land hydrology with the bucket model active only over idealised Africa while C_L is constant over idealised America.

4.5 Conclusions

In this chapter, the zonal asymmetry between ΔP over Equatorial Africa and the Amazon basin was investigated. Both regions receive ample rainfall in the present-day climate, but projected ΔP is positive over the former and negative over the latter. This does not follow the simple wet-get-wetter principle and poses the interesting question of what the different mechanisms are for ΔP in those two regions.

We used Isca (Vallis et al., 2018 and see Chapter 3) to design idealised Atmospheric General Circulation Models with different continental configurations. The main focus was on three experiments using rectangular, flat continents representing America and Africa, but first rainfall changes in two simulations with realistic continents and topography were studied.

Despite using an idealised model and zonally uniform SSTs, ΔP patterns similar to those projected by CMIP5 models were obtained in the simulation with realistic continents when land-surface evaporation was limited by soil moisture (using the 'bucket model' by Manabe, 1969, described in Section 3.2). In contrast, when evaporation over land was merely reduced by a constant factor compared to ocean evaporation, the P response to warming was zonally uniform, both for realistic and idealised continents. This finding suggests that limited soil moisture over land contributes to the zonally asymmetric ΔP patterns with drying in the Amazon basin and wetting over Equatorial Africa. More generally, the land-surface is clearly an active component of the climate system (Shukla and Mintz, 1982).

In the idealised simulations with two rectangular continents and bucket hydrology we found that the drying over the idealised Amazon basin was related to the warming-induced enhancement of convection over Equatorial Africa through the Matsuno-Gill theory (Gill, 1980). The anomalous ascent over idealised Africa is associated with anomalous subsidence over the Atlantic Ocean and America. This enhanced subsidence suppresses convection, reduces r and, as a result, P in those regions. In the absence of Africa, the idealised Amazon basin received more rainfall with warming. Hence, rainfall changes over South America can not be considered to be independent from changes over Africa.

A similar teleconnection could contribute to the projected drying of the Amazon basin in complex GCMs. This hypothesis is based on the finding that, despite

its simplicity, the set-up with two idealised continents produced most of the ΔP from the realistic-continents case and from coupled GCMs. In addition, Kooperman et al. (2018) suggested that enhanced ascent over Africa could contribute to drying of the Amazon basin in CMIP5 simulations. In future work, it should be investigated whether a similar teleconnection between Africa and South America occurs in a complex GCM or in Isca with realistic continents, by studying South America in isolation and then together with Africa.

The finding that idealised America did not experience a stronger drying in the presence of idealised Africa when soil moisture conductance was set to a constant (C_L = 0.7) is consistent with our conclusions from the simulation with realistic continents, but was somewhat surprising in the context of the teleconnection between idealised Africa and America and merits further investigation, ideally with a spatially varying land-surface hydrology.

So far, the impact of increasing CO_2 levels on land evaporation due to the closure of plant stomata has been neglected (Sellers et al., 1996). The simulations discussed in this chapter are therefore likely to underestimate the precipitation response to increasing CO_2 compared to more comprehensive Earth System Models (Skinner et al., 2017; Chadwick et al., 2017). The impact of stomatal closure on tropical ΔP will be investigated in the next chapter.

Chapter 5

The impact of vegetation on projections of tropical precipitation change

In this chapter, the impact of vegetation on continental precipitation change in the tropics is investigated. Preliminary results for this chapter were obtained and discussed together with Prof. Abigail Swann (University of Washington, Seattle), whom I visited for two months in April and May 2019. This chapter is currently being drafted as a paper and will soon be submitted for peer-review.

The main findings of this chapter are

1. A simple representation of changes in stomatal conductance with increasing CO_2 leads to stronger drying over the Amazon basin and stronger wetting of the Maritime Continent than if the vegetation response is neglected.

2. Over small islands, a decrease in stomatal conductance leads to stronger convection and moisture advection from the surrounding ocean. The consequent increase in precipitation is stronger when stomata are completely closed with warming than when they remain open.

3. Evaporation does not increase in-step with precipitation over South America along the Equator when changes in stomatal conductance are included. Moisture advection from surrounding areas increases, which might contribute to the strong decrease in rainfall over the Amazon basin.

5.1 Introduction

Precipitation changes over some tropical land regions (between 30°South and 30°North) are enhanced when vegetation responses to CO_2 forcing are taken into account compared to when they are neglected in Earth System Models (Chadwick et al., 2017; Swann et al., 2016; Skinner et al., 2017; Kooperman et al., 2018). The precipitation (P) decrease over the Amazon basin and P increase over the Maritime Continent are thus both amplified by plant physiological changes.

Earth System Models (ESMs) include parameterisations of several plant physiological responses to increasing CO_2 which have opposing effects on land-surface evaporation (see Section 2.5). On the one hand, stomatal conductance decreases in response to elevated CO_2 concentrations (Ainsworth and Long, 2005), which can result in reduced evapotranspiration (E_A) over land (Sellers et al., 1996). On the other hand, CO_2 fertilisation can increase the leaf area index (Mahowald et al., 2016; Skinner et al., 2018; Kooperman et al., 2018) potentially resulting in enhanced evapotranspiration. While the net response of vegetation to CO_2 forcing is unclear in natural ecosystems, recent studies suggest that the decrease in stomatal conductance dominates over increases in the leaf area index in Earth System Models (Swann et al., 2016; Swann, 2018; Skinner et al., 2017).

Over land, moisture for rainfall is provided by local evapotranspiration and by advection. Hence, precipitation change (ΔP) over land is tightly coupled to changes in evapotranspiration (ΔE_A), especially in areas where P depends on regional evapotranspiration (Spracklen et al., 2012; Kooperman et al., 2018; Skinner et al., 2017).

The change in E_A due to increasing CO_2 can be separated into two components: changes due to the plant physiological response and due to radiative transfer changes in the atmosphere (see Section 2.6, Swann et al., 2016, Skinner et al., 2017). The first is shown in simulations where only the vegetation is affected by the CO_2 forcing while the radiation component of the model sees pre-industrial conditions ('veg_{CO2}'). The second is shown when only the radiation scheme experiences the CO_2 increase while the vegetation sees pre-industrial CO_2 concentrations ('rad_{CO2}'). The plant physiological response on its own leads to a decrease in E_A over all land regions between about 15°S and 15°N in ESMs (Kooperman et al., 2018; Skinner et al., 2017; Swann et al., 2016). In the

same latitudinal band, the changes in radiative transfer lead to mixed responses in E_A, with increases over the Maritime Continent and Africa, and both increases and decreases over South America (Swann et al., 2016).

The relationship between ΔP and ΔE_A varies from one tropical land region to another. For example, in the veg_{CO2} simulations, P increases over the Maritime Continent and decreases over the Amazon basin, even though E_A decreases over both regions (Skinner et al., 2017; Saint-Lu et al., 2019; Kooperman et al., 2018). Recent studies suggest that the P increase over the Maritime Continent is due to a warming-induced enhancement of convection over the islands, which draws moisture in from the surrounding oceans (Saint-Lu et al., 2019; Kooperman et al., 2018; Chadwick et al., 2019). Over the Amazon basin, the response of P to a change in E_A is more complicated with regional differences between the Atlantic side of the Amazon basin and the Andes side. Saint-Lu et al. (2019) and Langenbrunner et al. (2019) both found that the Andes play a key role in the circulation response to CO_2. Saint-Lu et al. (2019) also highlighted the importance of the pre-industrial circulation regime over the Amazon basin.

In this chapter, we investigate the amplification of ΔP due to plant physiological changes over the Maritime Continent and the Amazon basin using the University of Exeter's framework for the idealised modeling of planetary atmospheres 'Isca' (Vallis et al., 2018 and see Section 3). In the following section, the Fu (or Budyko) curve is introduced, an important concept which elucidates the two limits on evaporation over land: energy and water availability. In Section 5.2.3, the parameterisation of stomatal closure in Isca is described. The simulations in this chapter include realistic continents with and without tropography, and idealised rectangular tropical continents of varying longitudinal extent. These set-ups are described in Section 5.2.4. The results are presented in three sections, starting from the impact of stomatal closure on ΔP over tropical land in simulations with realistic continents with and without topography (Section 5.3). In Section 5.4, the contributions from local evaporation and from moisture advection to ΔP are discussed for the idealised continents of varying width. In the last results section (Section 5.5), the impact of energetic and moisture constraints on E_A over an idealised American and idealised African continent are discussed. In the final section, the findings from this chapter are summarised and ideas for future work are presented.

5.2 Methods

5.2.1 The Fu curve

Potential evapotranspiration (E_P) is a measure for the evapotranspiration which would occur if the surface were saturated with water (Budyko, 1974). Over oceans, E_P is equal to the actual evapotranspiration (E_A). In order to understand the concept of potential evapotranspiration, it is useful to point out that E_P (in kg/(m^2·s)) can be estimated via

$$E_P \approx R_N / L \tag{5.1}$$

where R_N is the net radiation at the surface (in W/m^2) and L is the latent heat of vapourisation ($\approx 2.45 \cdot 10^6$ J/kg, Budyko, 1974). In this approximation, E_P represents the evaporation which would occur if the entire energy input to the surface were balanced solely by the latent heat flux. This simplification captures most of the evaporative behaviour over wet surfaces: Over oceans, roughly 90% of R_N is transformed into latent heat (Budyko, 1974), and about 80% over non-water-stressed soils (Koster and Mahanama, 2012; Milly and Dunne, 2016). Several methods exist to obtain a more accurate estimate of E_P based on the meteorological conditions and R_N, including for example the Penman-Monteith equation (Penman, 1948; Monteith, 1981; Milly and Dunne, 2016; Scheff and Frierson, 2014).

Potential and actual evapotranspiration are related via the Fu-equation, a more general form of the traditional Budyko-equation (Budyko, 1974) for different catchments

$$\frac{E_A}{P} = 1 + \frac{E_P}{P} - [1 + (\frac{E_P}{P})^{\omega}]^{1/\omega} \tag{5.2}$$

where ω is a catchment-specific parameter (Zhang et al., 2004). ω can be estimated from the climatological E_P, E_A and P for each region of interest by finding the minimum of

$$\sum_i \{\frac{(E_A)_i}{P_i} - \{1 + \frac{(E_P)_i}{P_i} - [1 + (\frac{(E_P)_i}{P_i})^{\omega}]^{1/\omega}\}\}^2 \tag{5.3}$$

where i indicates the year. The curve-shape parameter ω indicates how much of the available water (P) is evaporated (E_A) given the available energy (E_P, Li et al., 2013, Yang et al., 2008). For ω = 2.6, the Fu equation is equal to the traditional Budyko equation (Osborne and Lambert, 2018).

The Fu (or Budyko) curves help categorize land regions into moisture versus energy-limited (Fig. 5.1, Budyko, 1974, Milly, 1994, Zhang et al., 2004, Osborne and Lambert, 2018). In regions where E_P is less than P ($E_P/P < 1$), E_A is classed as 'energy-limited'. Where $E_P/P > 1$, E_A is termed 'moisture-limited'. E_P can be considered an upper limit for E_A, since no land regions are located on the other side of the $E_P = E_A$ line in the Budyko space (blue dashed line in Fig. 5.1).

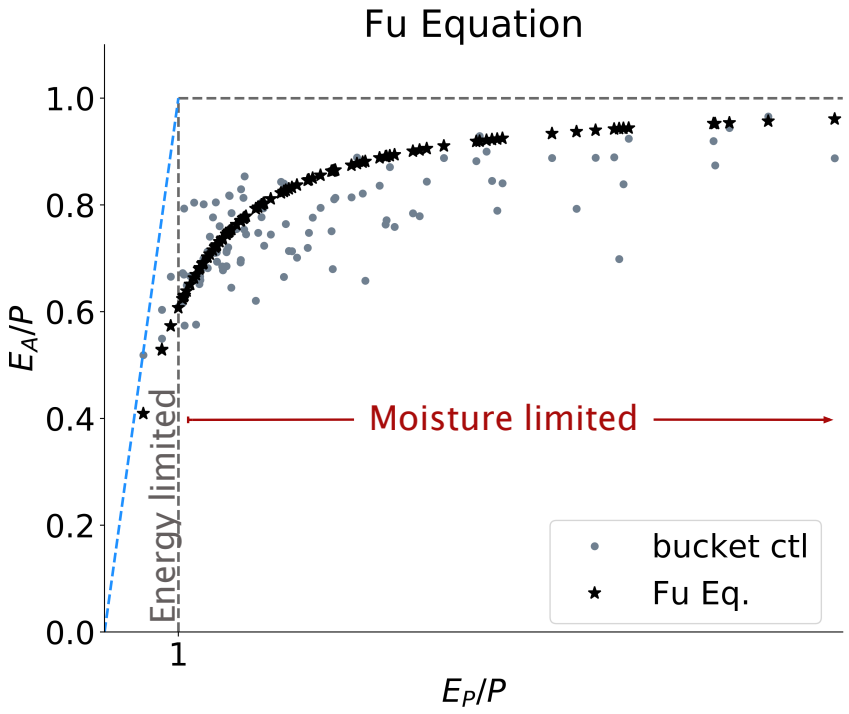

Figure 5.1: An example of the Fu curve (black asterisks) for data from one of our idealised control simulations. Each grey dot represents a land grid point between 10°S and 10°N. Most regions fall into the moisture-limited regime (E_P/P >1), whereas E_A is considered to be energy-limited (E_P/P <1) in only a few locations. The blue dashed line indicates $E_P = E_A$. In this example $\omega = 2.09$ for the Fu curve.

5.2.2 Moisture Budget Decomposition

In order to determine whether local changes in precipitation minus evaporation ($P - E$) are dominated by changes in specific humidity or circulation changes, the moisture budget of the atmosphere is split into the 'thermodynamic' (ΔTH), 'mean circulation dynamics' (ΔMCD), 'transient eddy' (ΔTE) and 'residual' (R) contributions following Seager et al. (2010). The long-term mean (denoted by the

overbars) atmospheric moisture budget is given by

$$\overline{P-E} = -\int_0^{p_S} \nabla.(\overline{q\mathbf{v}})\frac{dp}{g} \tag{5.4}$$

(see Eq. 2.3, Seager et al., 2010 and Trenberth and Guillemot, 1995). In this equation, q is specific humidity (in kg/kg), $\mathbf{v}$ is the three-dimensional velocity vector and $g \approx 9.81$ m/s^2 is the gravitational acceleration on Earth. The integral is performed over the entire atmospheric column ($p = 0$ at the top of the atmosphere, and $p = p_S$ at the surface), and $P - E$ is in units of kg/(m^{2}s). By applying the Reynolds decomposition (analogous to Eq. 2.13) to $\overline{q\mathbf{v}}$, we obtain

$$\overline{P-E} = -\int_0^{p_S} \overline{q}\nabla.\overline{\mathbf{v}} + \overline{\mathbf{v}}.\nabla\overline{q} + \nabla.(\overline{q'\mathbf{v}'})\frac{dp}{g} \tag{5.5}$$

where the primes denote deviations from the time mean. Since $\nabla.\mathbf{v} = 0$ in pressure coordinates (Holton, 2004, p.59), and

$$\Delta(A \cdot B) = A_{ctl}\Delta B + B_{ctl} \cdot \Delta A + \Delta A \cdot \Delta B \tag{5.6}$$

where the subscript ctl denotes quantities from the unperturbed climate, the three terms contributing to changes in $P - E$ can be written as

$$\Delta TH = -\int_0^{p_S} \overline{\mathbf{v_{ctl}}}.\nabla(\overline{\Delta q})\frac{dp}{g} \tag{5.7}$$

$$\Delta MCD = -\int_0^{p_S} (\Delta\overline{\mathbf{v}}).\nabla\overline{q_{ctl}}\frac{dp}{g} \tag{5.8}$$

$$\Delta TE = -\int_0^{p_S} \nabla.\Delta(\overline{q'\mathbf{v}'})\frac{dp}{g}. \tag{5.9}$$

The residual is calculated as

$$R = \Delta(P-E) - \Delta TH - \Delta MCD - \Delta TE \tag{5.10}$$

and captures the non-linear term ($\Delta NL = \Delta\overline{\mathbf{v}}.\nabla(\Delta\overline{q})$, see Eq. 5.6) as well as computational inaccuracies. Note that while the circulation is held constant in the thermodynamic term, changes in the circulation do affect the distribution of specific humidity (Seager et al., 2010).

5.2.3 Model

We use 'Isca' (Vallis et al., 2018) to design Atmospheric General Circulation Models (AGCMs) in order to study the impact of plant physiological changes on continental ΔP. The modeling framework was described in detail in Chapter 3.

As discussed in Section 3.2, in Isca, land evaporation (E_L) is parameterised as

$$E_L = C_L \cdot E_{OC} \tag{5.11}$$

(see Eq. 3.2), where $C_L \leq 1$ represents the conductivity of the soil to moisture and thus reduces evaporation over land compared to ocean (E_{OC}). The bucket model following Manabe (1969) sets C_L depending on the available soil moisture, with moisture being replenished by precipitation and lost through evaporation (see Section 3.2).

In this section, another limiting factor for land evaporation is introduced to the above equation, namely the vegetation pre-factor C_V (as discussed in Section 3.2). In Equation 5.11, the conductivity C_L becomes

$$C' = C_V \cdot C_L \tag{5.12}$$

(see Eq. 3.3), where C_V represents the impact of stomatal closure on moisture conductance by the land. When C_V = 1 and C_L is given by the bucket hydrology, land surface evaporation is only limited by soil moisture. When C_V <1, stomatal closure is taken into account in addition to the soil moisture limitation.

Potential evaporation (E_P) is directly saved as model output in Isca as the evaporation which would occur if the soil were saturated with water ($C_L = 1$). Note that E_P takes changes in stomatal conductance into account, since at 100% conductance (C_V = 1) the pre-factor C' = 1 for a full bucket (C_L = 1) , but $C' <$ 1 when stomatal conductance (C_V) is reduced even when the bucket is full. For other GCMs, E_P is not a standard output and is usually calculated offline via the Penman-Monteith equation (Penman, 1948; Monteith, 1981; Milly and Dunne, 2016; Scheff and Frierson, 2014).

5.2.4 Model Simulations

Several different continental configurations are studied in this chapter, starting from realistic continents with topography and then turning to idealised continents of various widths. The simulations for this chapter are summarised in Table 5.1. As in Chapter 4, atmospheric CO_2 concentrations are set to 300 ppm in the control climate and a zonally uniform sea surface temperature (SST) climatology based on the Atmospheric Model Intercomparison Project (AMIP, Gates, 1992)

SSTs is prescribed (see Fig. 3.1). The climate is perturbed by doubling the CO_2 concentration and uniformly increasing SSTs by 2.52 K as in Chapter 4.

In this chapter, the impact of plant physiological changes on continental precipitation is examined using a simple parameterisation of stomatal closure (see Section 5.2.3). In the control climate, the stomatal conductance is 100%. In the perturbed climate, stomatal conductance is either held the same at 100% ('bucket') or is reduced to 0% ('0%cond'), 20% ('20%cond'), 50% ('50%cond') or 70% ('70%cond') by setting C_V in Equation 5.12 to 1.0, 0.0, 0.2, 0.5 and 0.7, respectively. Inferring from Ainsworth and Rogers (2007), C_V for natural ecosystems might lie somewhere between 0.5 and 0.8 for an increase in the CO_2 concentration from 300 ppm to 600 ppm, depending on the plant functional type. The exact value will also vary based on the geographical location and environmental stress factors (Ainsworth and Long, 2005, Ainsworth and Rogers, 2007 and see Section 2.5). We focus mostly on the 50%cond case because it produces clearer ΔP changes than the 70%cond case, without leading to an extreme drying almost everywhere as in the 20%cond case (see Fig. 5.4).

Changes in P or E_A due to the doubling of CO_2 are calculated as the difference between the perturbed (pert) and control (ctl) climates, e.g. (50%cond pert) - (bucket ctl) or (bucket pert) - (bucket ctl). Unless otherwise specified, '0%cond' always refers to (0%cond pert) - (bucket ctl), '50%cond' to (50%cond pert) - (bucket ctl) and so on, and 'bucket' refers to (bucket pert) - (bucket ctl).

First, a simulation is run with realistic continents with topography using the bucket hydrology in the control and perturbed climate ('RC bucket'), and then with a 50% reduction in stomatal conductance in the perturbed climate ('RC 50%cond'). The same land hydrologies are used for simulations with realistic continents but without topography ('RCflat bucket' and 'RCflat 50%cond').

Idealised rectangular flat continents of various widths are used (see Fig. 5.4), namely 3° lon (roughly corresponding to the width of Sulawesi in the Maritime Continent), 6°, 12°, 24°, 40° lon (resembling South America, 'AM'), 60° lon (representing Africa, 'AF') and 100° lon, which could be compared to the supercontinent Pangaea. All of those simulations are run with varying degrees of stomatal closure, with stomatal conductance in the perturbed climate ranging from 0% (no evaporation over land) to 100% (equivalent to the bucket hydrology). Following on from Chapter 4, we also study two neighboring continents at the distance of

the Atlantic Ocean (40° longitude) apart: idealised America and idealised Africa ('2C') and two America-sized continents ('2AM'), also with different stomatal conductances in the perturbed climate. Note that the 'bucket' experiments for RC, AM, AF and 2C are equivalent to the simulations 'RC', 'AM', 'AF' and '2C' from Chapter 4.

In order to decompose ΔP for '50%cond' into the contribution from CO_2-induced radiative transfer changes and plant physiological changes (in our case changes in stomatal conductance), simulations with 50% stomatal conductance in the control climate are performed for the idealised continents with 3° to 100° longitudinal extent. The change in precipitation in these 'stomata' experiments is then calculated as (50%cond ctl) - (bucket ctl), which is our equivalent to 'CO_2phys' from Swann et al. (2016) and 'CO2_Stomata' from Skinner et al. (2017). The component due to radiative transfer changes in our case is simply given by the 'bucket' experiment where stomatal conductance remains at 100% in the perturbed climate, i.e. (bucket pert) - (bucket ctl) as above. This is equivalent to the 'CO_2rad' experiments in Swann et al. (2016) or Skinner et al. (2017).

Name	Continents	Hydrology		Ocean	Perturbation
		control	perturbed		
RC bucket	realistic, topography	bucket	bucket	zon. symm. SSTs	2xCO_2 + 2.52K
RC 50%cond	realistic, topography	bucket	C_V=0.5	zon. symm. SSTs	2xCO_2 + 2.52K
RCflat bucket	realistic, flat	bucket	bucket	zon. symm. SSTs	2xCO_2 + 2.52K
RCflat 50%cond	realistic, flat	bucket	C_V=0.5	zon. symm. SSTs	2xCO_2 + 2.52K
3°	flat rectangle 30°S - 30°N, 0° - 3°E	bucket	C_V=0; 0.5; 1	zon. symm. SSTs	2xCO_2 + 2.52K
6°, 12°, 24°, AM, AF, 100°	Same as 3° but with 6°, 12°, 24°, 40°(AM), 60°(AF) and 100° longitudinal extent with C_V=0 (0%cond), C_V=0.2 (20%cond), C_V=0.5 (50%cond), C_V=0.7 (70%cond) or C_V=1 (bucket) in the perturbed climate and bucket hydrology in the control				
2C and 2AM	Same as above but for two continents (AM + AF, and AM + AM) at 40°lon distance				
'stomata'	exps: 3° - 100°	bucket	C_V = 0.5	zon. symm. SSTs	None

Table 5.1: Experimental set-ups used in Chapter 5 in order of their appearance.

5.3 Sensitivity of precipitation change to stomatal closure

Precipitation changes are amplified over the Amazon basin and the Maritime Continent in our simulation with realistic continents and a 50% decrease in stomatal conductance (Fig. 5.2), as expected from Earth System Models (Chadwick et al., 2017; Swann et al., 2016; Skinner et al., 2017; Kooperman et al., 2018). When stomatal conductance is held at control levels ('bucket', Fig. 5.2b), most Equatorial land regions (between 10°S and 10°N) receive more rainfall with warming, except for South America where P increases along the Equator and decreases to the north and south (see also Section 4.3). When stomatal closure is included, the Amazon basin exhibits a much clearer P decrease (i.e. 'drying') tendency (Fig. 5.2a). Over the Maritime Continent, the P increase (i.e. 'wetting') is much stronger in '50%cond' than in the 'bucket' simulation. Over Equatorial Africa the response to stomatal closure is mixed, which is also in line with more comprehensive models (Chadwick et al., 2017; Kooperman et al., 2018). Our simple representation of vegetation – only including changes in stomatal conductance – is thus able to capture a similar sensitivity of ΔP to vegetation changes as ESMs.

Topography affects ΔP in our simulations, particularly over South America, consistent with e.g. Saint-Lu et al. (2019) and Langenbrunner et al. (2019). In a simulation with flat continents and bucket hydrology (Fig. 5.3b), P increases strongly over tropical South America, whereas with topography (Fig. 5.2b), P decreases to the north and south of the Equator and the increase along the Equator is weak. ΔP over Africa and the Maritime Continent appear to be less affected by topography in the simulations with simple bucket hydrology.

Topography also has an influence on the sensitivity of continental ΔP to stomatal closure. In the absence of topography (Fig. 5.3b), stomatal closure still leads to a drying over parts of the Amazon basin as in the simulations with topography (Fig. 5.2b). However, the drying influence of stomatal closure is stronger in the case with topography (Fig. 5.2c) than with flat continents (Fig. 5.3c). Over the Maritime Continent, the response of ΔP to stomatal closure is mixed in the flat-continents case. This is in contrast to the simulation with topography, where ΔP is clearly enhanced when stomatal closure is taken into account. Hence, to-

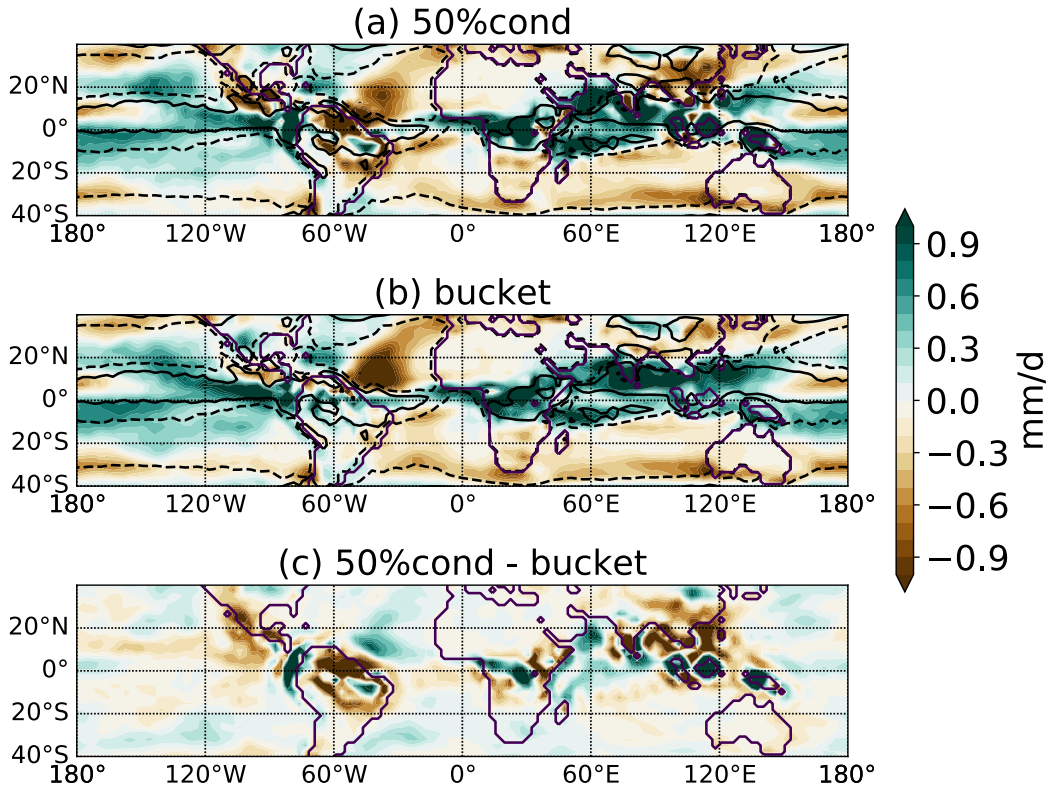

Figure 5.2: Annual mean ΔP in response to a doubling of CO_2 for the realistic continents (RC) with (a) and without (b) parameterisation of the stomatal closure effect. Panel c shows the difference between the two.

pography clearly modifies the response of P to warming and stomatal closure over the Amazon basin and over the Maritime Continent. While the influence of topography on the sensitivity of ΔP to stomatal closure is certainly an interesting finding which merits further investigation, the present study focuses on more fundamental aspects of the continents such as size and evaporative resistance.

5.4 Moisture advection versus local evapotranspiration

In a simulation with two idealised, rectangular continents and bucket hydrology (Fig. 5.4: row 2C, column 'bucket') the ΔP response is surprisingly similar to the realistic continents (Fig. 5.2b). P increases over idealised Africa and decreases over parts of idealised South America, as it does in the simulation with realistic continents (see also Section 4.3 for a more detailed discussion).

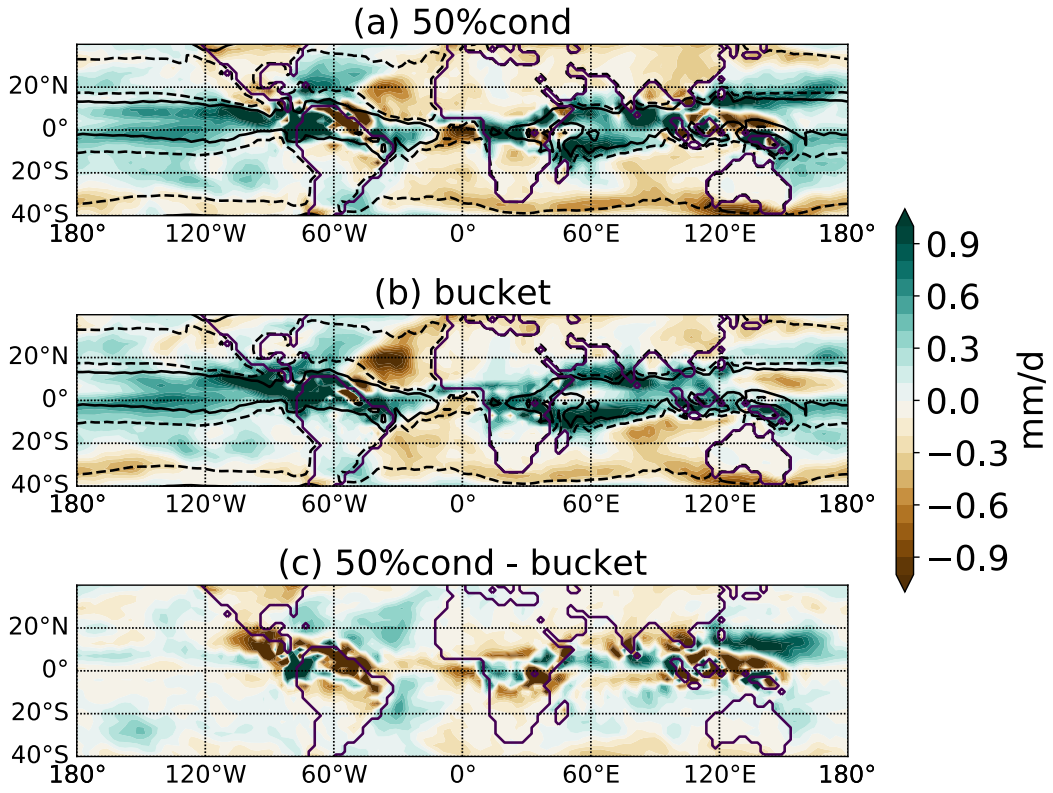

Figure 5.3: ΔP for RCflat a) with and b) without parameterisation of the stomatal closure effect, and the difference between the two (c).

More importantly, the simulations with two idealised continents reveal a sensitivity to changes in stomatal conductance which is similar to the response over the realistic continents. In 2C with 50% stomatal closure (Fig. 5.4: 2C, '50%cond'), the drying over idealised South America is enhanced compared to the 'bucket' case, while the African continent shows no clear ΔP response to the change in stomatal conductance. Similar to the Maritime Continent, the narrowest continent also sees a stronger P increase along the Equator when stomatal conductance decreases with warming compared to the 'bucket' simulation (Fig. 5.4: 3°, comparing the '50%cond' column with the 'bucket' column).

The fact that the idealised continents exhibit a similar ΔP behaviour to the realistic continents – which in turn capture some of the behaviour of more complex models – suggests that the insight gained from our idealised continent experiments could contribute to our understanding of some of the warming-induced rainfall changes seen in more complex ESMs in response to vegetation changes.

Humidity for continental rainfall is provided by moisture advection and by local evapotranspiration (E_A). The role of moisture advection for ΔP can be investi-

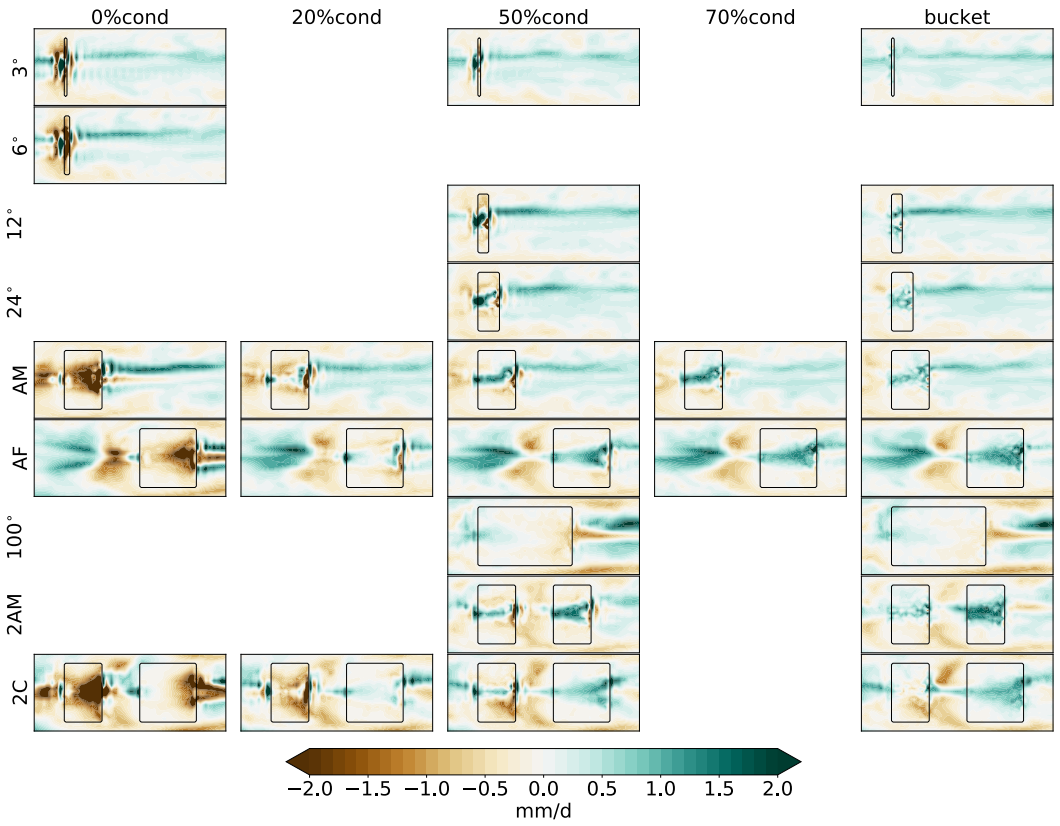

Figure 5.4: ΔP for the idealised continents with different stomatal conductances in the perturbed climate (x-axis) and different continental widths (y-axis). Note the different range of the colourbar compared to the previous two figures.

gated best in the extreme stomatal closure scenario, where no evaporation occurs over land surfaces in the perturbed climate ('0%cond'). This results in a P decrease over all land regions for any continent wider than 3° longitude. In this case, the narrowest island sees a strong increase in Equatorial P (Figs. 5.4 and 5.5: 3°, '0%cond'). The P increase is much stronger in '0%cond' than when the stomata remain completely open in the perturbed climate ('bucket').

For the narrow island (3°) in the '0%cond' case, temperatures at the surface and in the lower troposphere increase (Fig. 5.6a) since the land surface cannot release energy in the form of latent heat through evapotranspiration (Manabe et al., 1991; Dong et al., 2009). This triggers an enhancement of ascent and low-level convergence over the island, which acts to advect moisture from the surrounding ocean. Therefore, relative humidity (Fig. 5.7a) and thus P increase over the island, despite the fact that moisture cannot be provided locally by the land surface. This finding confirms recent studies which propose this mechanism

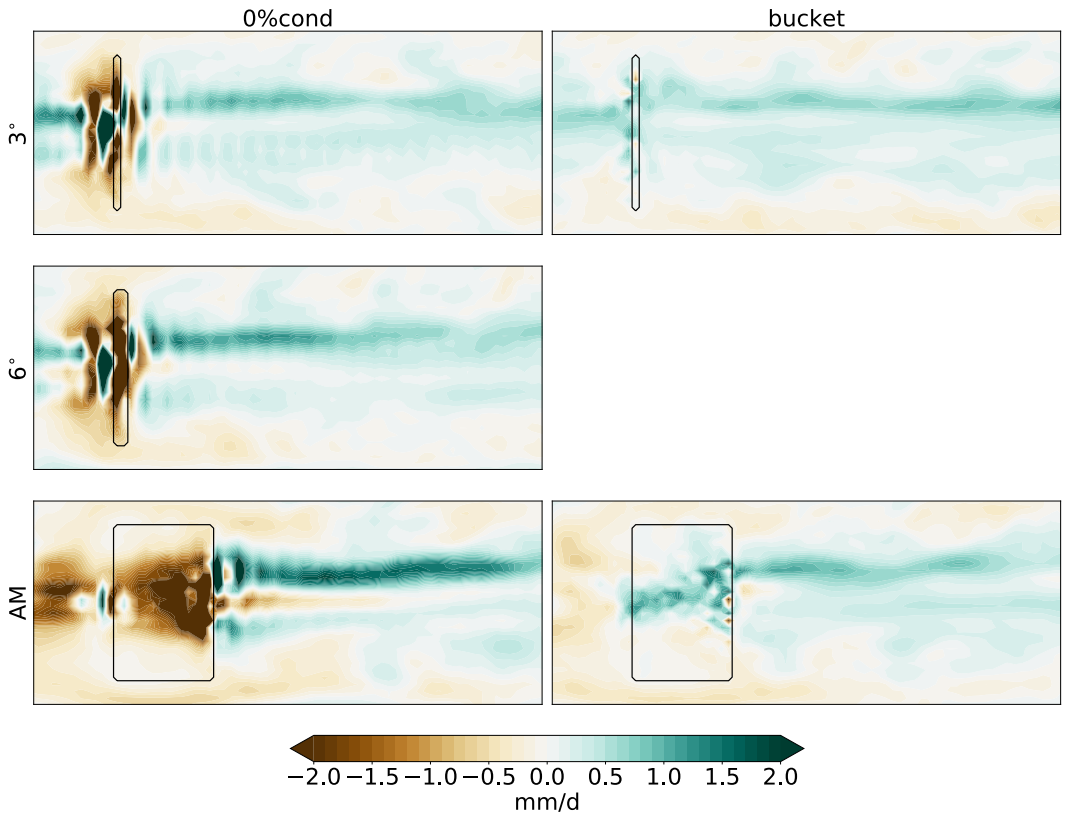

Figure 5.5: Precipitation changes as in Figure 5.4 but only for the 3°, 6° and AM continents and stomatal conductances of 0% and 100% (bucket) in the perturbed climate.

as explanation for the vegetation-change induced rainfall increase over the Maritime Continent (Chadwick et al., 2019; Saint-Lu et al., 2019; Kooperman et al., 2018).

The circulation and P responses over the 3° continent and the surrounding ocean are strong when evaporation over land is decreased to zero in the perturbed climate. In comparison, when stomatal conductance remains at 100% (bucket), the temperature and circulation responses are much weaker (Fig. 5.6b). As a result, moisture convergence and P increase less than when evaporation from land surfaces is completely switched off in the perturbed climate. The '50%cond' case shows an intermediate response with more widespread but slightly weaker P increases in the Equatorial region compared to the '0%cond' case (Fig. 5.4: 3°, '50%cond'). Hence, maybe counter intuitively, P over a narrow island such as the Maritime Continent is enhanced much more when E_A over land ceases with the CO_2 increase ('0%cond') than when moisture can be provided by local evapotranspiration ('bucket' and also '50%cond').

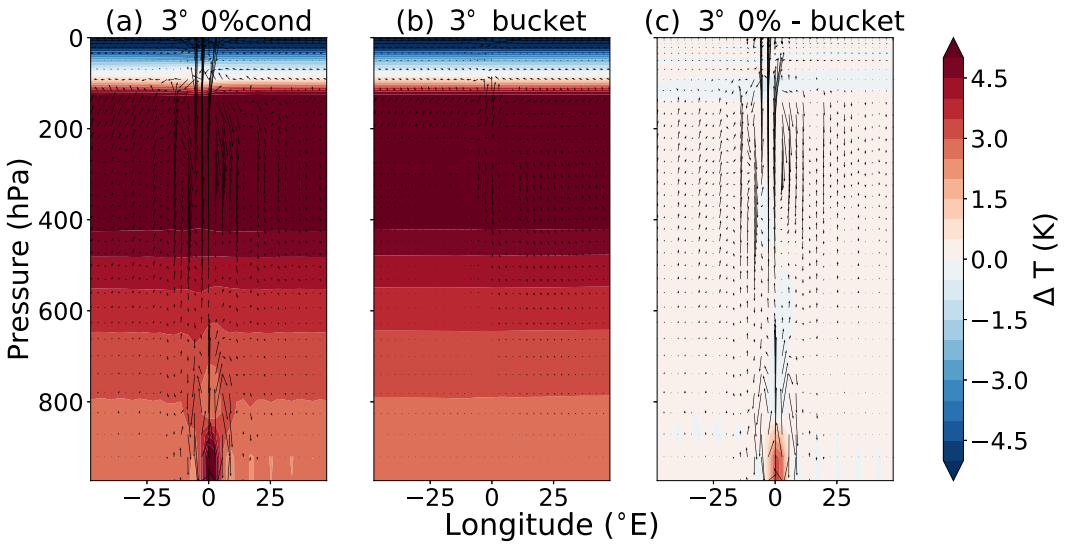

Figure 5.6: Doubling of CO_2 induced changes in temperature (ΔT, colours, in Kelvin) and the zonal circulation (vectors, in m/s) averaged over 10°S - 10°N for the narrowest continent (3° lon) with a) 0% and b) 100% (bucket) stomatal conductance in the perturbed climate, and the difference between the two cases (c). The continent is located at 0° lon and has a negligible extent in this graphic. The change in the vertical velocity has been amplified by a factor of 3000 following Nie et al. (2010)

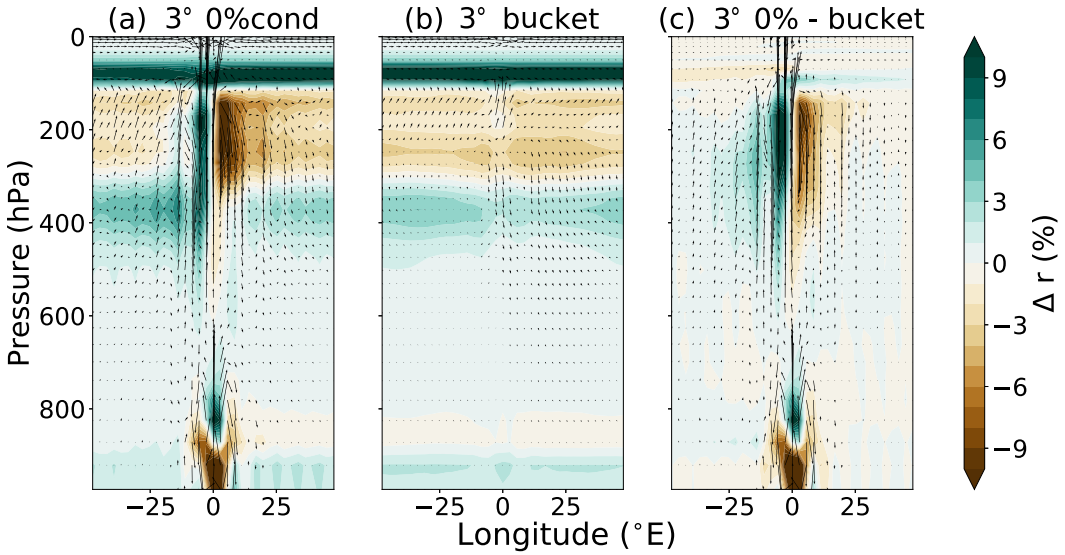

Figure 5.7: Same as Figure 5.6 but with changes in relative humidity (Δr in absolute %) instead of ΔT.

While the 3° continent gets wetter along the Equator in the experiment with 0% conductance in the perturbed climate, all continents of 6° longitudinal extent or more get drier (Fig. 5.5: column '0%cond'). For all continents wider than 3° longitude, moisture advection from the ocean is no longer sufficient to increase P with warming. Instead, local evapotranspiration is required to provide moisture for rainfall.

Thus, in terms of ΔP there is a balance between the width of the continent and the degree of stomatal closure with increasing CO_2. A very narrow continent sees a strong P increase when stomatal conductance completely ceases with the CO_2 perturbation ('0%cond'), whereas a wider continent dries out in this experiment. The highest stomatal conductance ('bucket') sees weaker ΔP over all continents, but P is able to increase for continents of all widths less than 100° in this case.

Intuitively, one might expect a 50% decrease in stomatal conductance to result in a P decrease over all continents, due to restricted evaporation. However, P and E_A both increase over parts of each individual continent between 10°S and 10°N (Figs. 5.4 and 5.8: row 3° to AF, column '50%cond'). The 'bucket' and 'stomata' experiments help decompose ΔP into the contributions from changes in radiative transfer versus stomatal conductance. Figure 5.9a shows that stomatal closure on its own leads to a P decrease, whereas the change in radiative transfer alone leads to a P increase over the Equatorial region (10°S-10°N) for each individual continent. For idealised Africa, the two components add linearly to give the full ΔP response. For all other continents, the full response lies somewhere between the 'stomata' and radiative-transfer induced ΔP. This indicates that the full ΔP is a combination of increasing P due to changes in the radiative transfer, and the stomatal closure induced P decrease, but non-linear effects are not negligible.

The 'stomata' and 'bucket' experiments can be compared to the 'veg_{CO2}' and 'rad_{CO2}' style experiments from Skinner et al. (2017) or Swann et al. (2016) (albeit the experiments have slightly different names there, see Section 5.2.4). For the 'bucket' experiments, our findings are consistent with Swann et al. (2016) and Skinner et al. (2017) over the Maritime Continent and Equatorial Africa with increases in all cases (Fig. 5.9a, 3° and 60°), but for individual idealised America (Fig. 5.9a, 40°), P increases in our 'bucket' simulation and decreases in these authors' rad_{CO2} style experiments over the Amazon basin. This is likely due to the presence of Africa in the ESMs, which has a drying influence on South

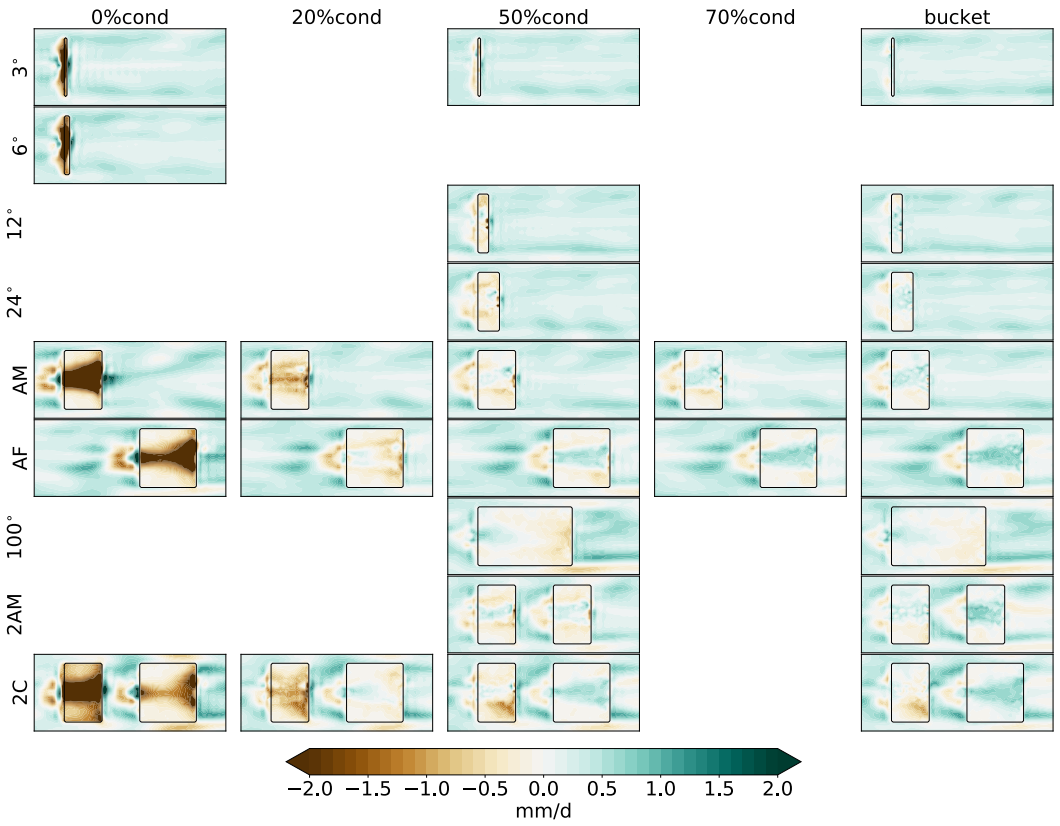

Figure 5.8: Annual mean ΔE_A for different continental widths (y-axis) and degrees of stomatal closure in the perturbed climate (x-axis).

America as we found in Chapter 4. For the 'stomata' experiments, our results are consistent with the veg_{CO2}-style experiments from Swann et al. (2016) and Skinner et al. (2017) over the Amazon basin, but not for Equatorial Africa and the Maritime Continent. Interestingly, in our simulations the radiative transfer changes are clearly required to produce the P increase over the narrow island (Fig. 5.4: 3°, '50%cond'), whereas in ESMs, the vegetation response alone is sufficient to enhance the circulation and rainfall over the Maritime Continent, possibly due to topographic features.

5.5 Limits on evaporation

As briefly mentioned above, in Chapter 4 we showed that the warming-induced enhancement of ascent over idealised Equatorial Africa leads to a decrease in P over idealised America to the south of the Equator (in the 'idealised Amazon basin') for the traditional bucket model. Our simulations with stomatal closure re-

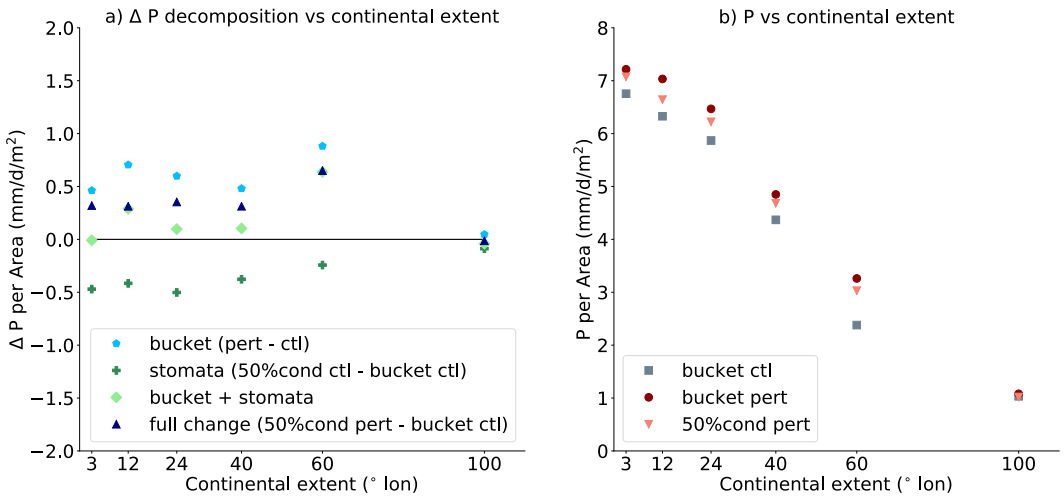

Figure 5.9: a) Decomposition of area-averaged (from 10°S to 10°N) annual mean ΔP for 50%cond ('full change') into the contribution from changes in radiative-transfer ('bucket') and changes in stomatal conductance at control CO_2 levels ('stomata'). b) Annual mean, area weighted P for different continental extents for the control climate with completely open stomata (bucket ctl) and the perturbed climates (bucket pert and 50%cond pert). Precipitation per area decreases by 0.063 (bucket ctl), 0.067 (bucket pert) and 0.066 (50%cond pert) per degree longitude in (b).

veal that the decrease in P with warming over the idealised Amazon basin is even stronger when stomatal conductance is reduced with warming (Fig. 5.4: compare 2C '50%cond' to 2C 'bucket'). This is in accordance with projections from comprehensive GCMs or ESMs (see Section 2.6) and with our realistic simulation (Fig. 5.2). The amplified P decrease over the idealised Amazon basin in '50%cond' could either be caused remotely by a stronger circulation response over idealised Africa (and hence stronger subsidence and drying over the Amazon basin), or by local changes over idealised America, or a combination of both.

The drying impact of idealised Africa on idealised South America does not change significantly when stomatal closure is represented in the model (Fig. 5.10). Hence, the additional decrease in P over idealised South America must largely be the result of local changes. We note that there is a small region on the Equator and to the North where the difference between the 'bucket' and '50%cond' experiments is not zero (Fig. 5.10c). This is not the focus of the present discussion but merits further investigation in future work.

The individual idealised American continent exhibits a stronger sensitivity to

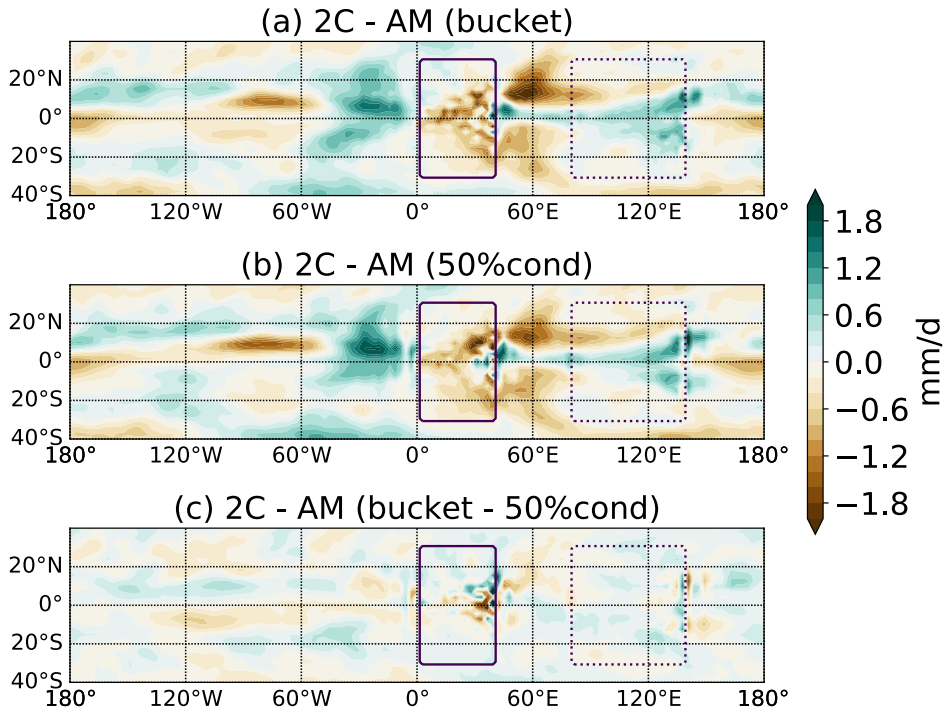

Figure 5.10: ΔP for 2C-AM a) in the bucket simulation, b) in 50%cond and the difference between the two (c). Taking the difference between 2C and AM shows the impact that the presence of Africa in 2C has on the American continent (see also Section 4.4).

changes in stomatal conductance than the idealised African continent (Figure 5.11). When stomatal conductance decreases, idealised America sees a strong P decrease in the idealised Amazon basin (Fig. 5.4: AM '50%cond'). When stomata remain completely open in a warmer climate, P increases or remains the same, but does not decrease anywhere (Fig. 5.4: AM 'bucket'). In contrast, for the idealised African continent the P increase is similar with and without stomatal closure (Fig. 5.4: AF '50%cond' versus AF 'bucket'). The stronger sensitivity of ΔP to changes in stomatal conductance over the American continent compared to the African continent is also reflected in the slopes of the regression lines in Figure 5.11 with k $\approx$ 2 for AM and k $\approx$ 1 for AF. Hence, the warming-induced circulation anomaly over idealised Africa and consequent subsidence over idealised America is similar with or without stomatal closure. This is inferred[1] here from the similar ΔP over Equatorial Africa with and without stomatal closure (Fig. 5.11) and the similar drying impact of idealised Africa on idealised America in Figure 5.10. In the following, we will outline one possible explanation for the higher sensitivity of

[1] This also becomes evident when comparing Fig. 5.21b to Fig. 4.5b.

ΔP to stomatal closure over the smaller idealised American continent compared to the larger idealised African continent.

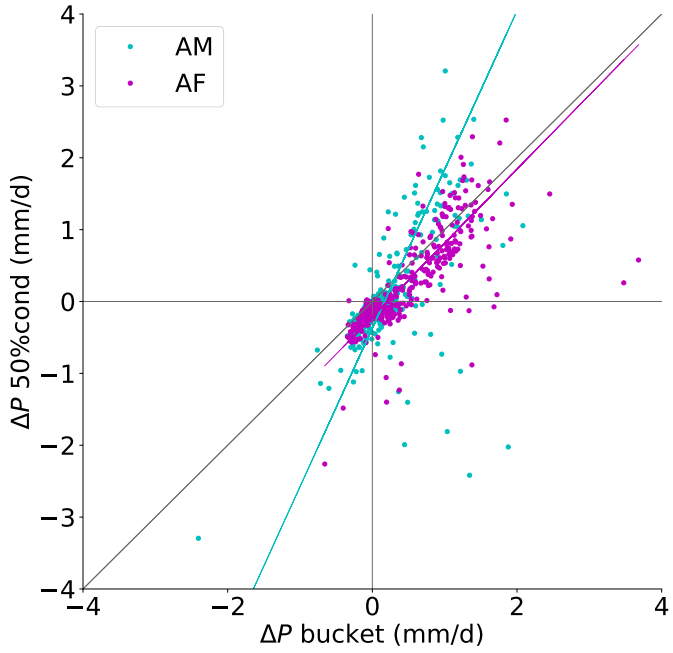

Figure 5.11: Annual mean ΔP for all land points between 10°S and 10°N for individual idealised America (AM, cyan) and idealised Africa (AF, magenta) for the 'bucket' simulation (x-axis) and for 50%cond (y-axis). Total least squares regressions were used to fit the linear regressions. The black line represents $y = x$. The slope of the line for idealised Africa is k = 1.03 with a correlation coefficient of r = 0.77. For idealised America, the slope of the line is 2.21, and r = 0.56.

The increase in E_A over idealised America along the Equator and to the north is weaker in the experiment with stomatal closure compared to the 'bucket' experiment (Fig. 5.8: compare AM '50%cond' with 'bucket'). Somewhat counter intuitively, the P increase is stronger in this region in '50%cond' than in 'bucket'. In contrast, over idealised Africa E_A seems to be tightly coupled to P when comparing the experiments with and without stomatal closure.

But why does E_A over idealised Equatorial America not increase in step with P, whereas it does over idealised Africa, even though the change in stomatal conductance is the same for both continents? The Budyko framework provides helpful insight into the limits on evapotranspiration over those two continents of different size.

In the Fu or Budyko space, control climate E_A over idealised Equatorial Amer-

ica would still be classed as 'moisture-limited' but is close to the energy limit, whereas E_A over idealised Africa is clearly moisture-limited (Fig. 5.12). In the perturbed 'bucket' case, the limits on E_A largely remain the same for both continents. However, in '50%cond' E_A over idealised America becomes energy-limited along the Equator and to the north and remains moisture-limited in the idealised Amazon basin. Over idealised Equatorial Africa, E_A remains moisture limited. As a result, the increase in E_A over idealised America along the Equator and to the north is weaker in '50%cond' than in 'bucket' (Fig. 5.8), even though the P increase is stronger.

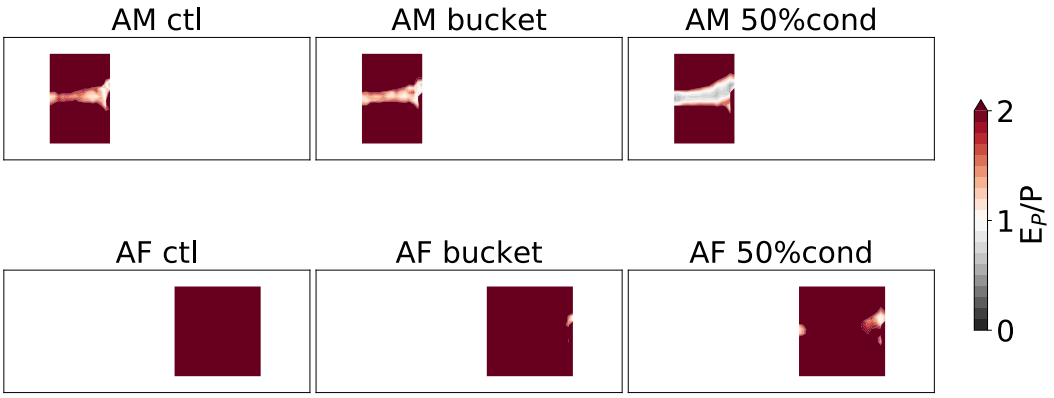

Figure 5.12: Moisture (red) and energy (grey) limited regions for AM and AF in the control and perturbed ('bucket' and 50%cond) climates. White areas lie between the moisture and energy limit.

Since E_A over idealised America along the Equator and to the north is not high enough to provide moisture for the strong P increase, moisture convergence into the region increases (Fig. 5.13). In the idealised Amazon basin moisture divergence increases, possibly as a result of the increased moisture demand in the convergence region along the Equator and to the north. This might explain why the decrease in P in the idealised Amazon basin is stronger in the '50%cond' experiment compared to the 'bucket' case.

The change in $P-E$ for example from Figure 5.13 can be decomposed into the contribution from changes in the specific humidity (the 'thermodynamic' component ΔTH), dynamical changes due to the mean circulation (ΔMCD) and transient eddies (ΔTE), and a residual term (R, see Section 5.2.2 and Seager et al., 2010). In both the 'bucket' and '50%cond' cases, the contributions from ΔTH and ΔMCD are largest, with a small contribution from ΔTE and even smaller resid-

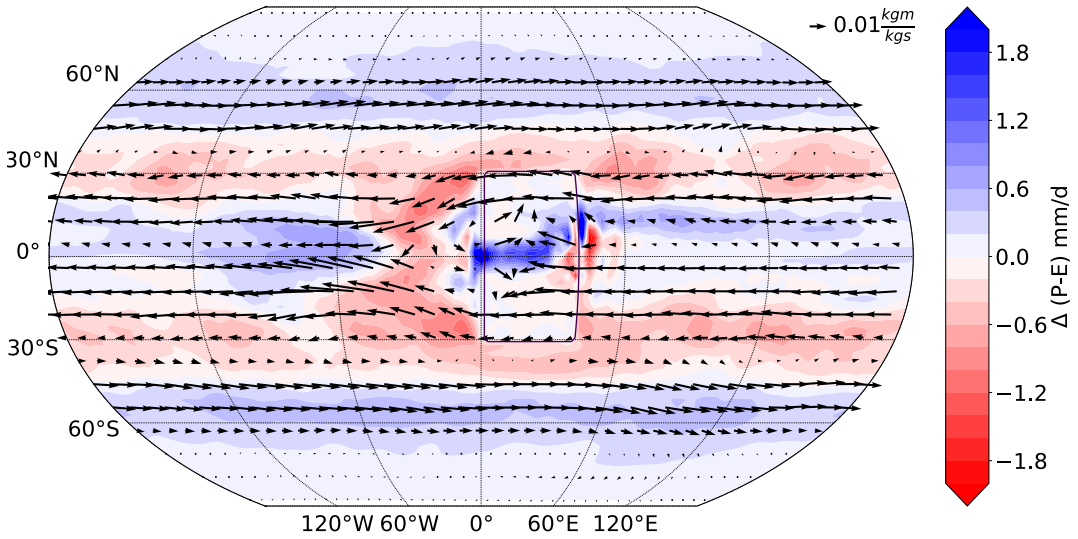

Figure 5.13: Colours show changes in the column-integrated moisture flux convergence or $P - E$ (see Eq. 2.3) and arrows show 870hPa moisture flux for AM 50%cond.

ual (Fig. 5.14), in line with Seager et al. (2010). The same holds true for most of the other continental sizes considered here (between 3° and 100° longitudinal extent), with ΔTH and ΔMCD generally being the largest contributions to the overall changes in $P - E$ (Fig. 5.15).

In the '50%cond' case for idealised America (Fig. 5.14b), ΔTH and ΔMCD have the same sign in some areas of the Equatorial region, but in the idealised Amazon basin ΔMCD leads to a decrease in $P - E$ which overcompensates the increase from thermodynamic changes. For the 'bucket' experiment, ΔMCD partly offsets the thermodynamic changes – which clearly dominate the overall change in $P - E$ (Figs. 5.14a and 5.15a.) – in all Equatorial regions.

Another way of presenting the limits on E_A over idealised America and Africa is the Fu curve (Fig. 5.16). For idealised America, a larger number of land regions move from the moisture-limited section of the Fu curve in the control climate to the energy-limited section for '50%cond' than for the 'bucket' experiment. For the idealised African continent, only very few regions move into the energy-limited regime in both the '50%cond' and 'bucket' experiments. For both continents, the Fu curve shifts downward with warming in the bucket case, and upward in the '50%cond' case. The changes in the shape of the Fu-curve are reflected in changes of the shape parameter ω: Values for idealised America are 2.09 (ctl), 2.01 ('bucket') and 2.27 (50%cond). For idealised Africa, ω = 1.90 (ctl), 1.85

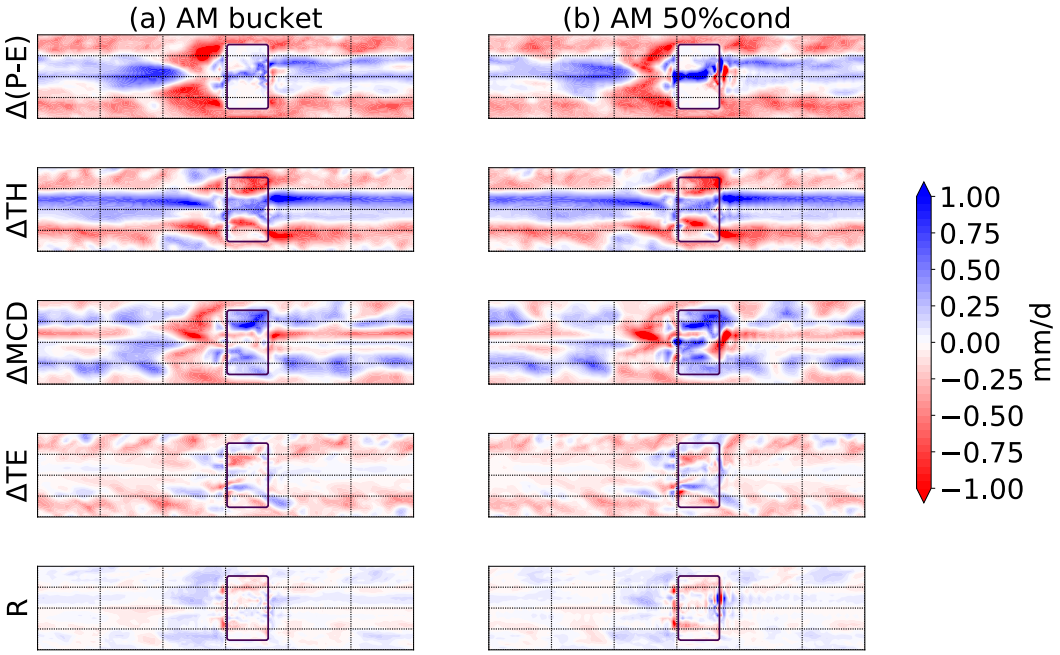

Figure 5.14: Moisture budget decomposition following Seager et al. (2010) for a) the 'bucket' and b) the '50%cond' experiment with idealised America. Changes in $P - E$ (top row) are split into the thermodynamic (ΔTH), mean circulation dynamics (ΔMCD) and transient eddy (ΔTE) contributions, and a residual (R, see Section 5.2.2).

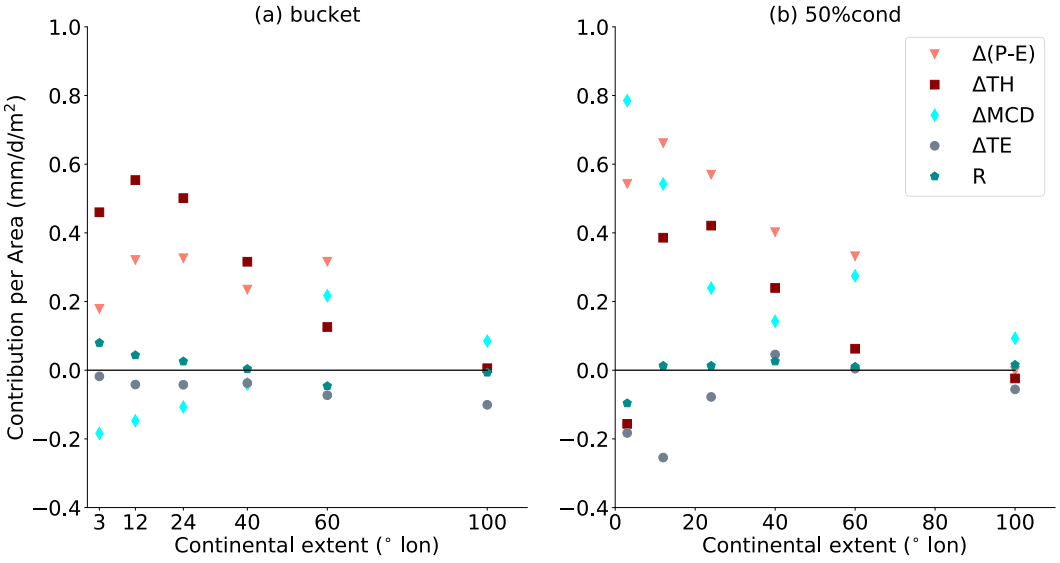

Figure 5.15: Area-averaged moisture budget decomposition into the same components as in Figure 5.14 for all continent sizes from 3° to 100° longitudinal extent for a) the 'bucket' and b) the '50%cond' experiments. The average is taken over the Equatorial region (10°S to 10°N).

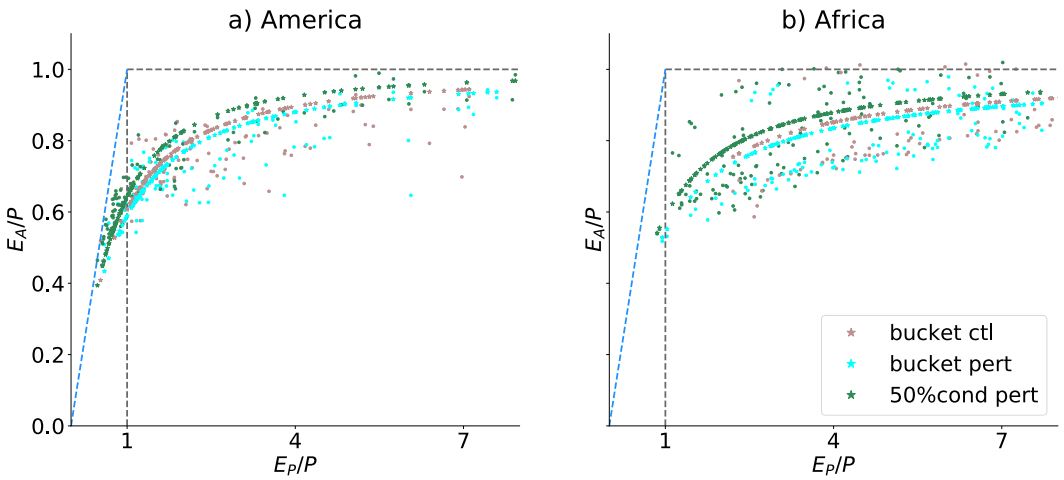

Figure 5.16: Fu curves for a) idealised America and b) idealised Africa for the control climate (sand), the perturbed 'bucket' climate (cyan) and the perturbed 50%cond climate (green). The small dots represent land grid points between 10°S and 10°N, while the asterisks represent the Fu curves fitted to the data.

('bucket') and 2.01 (50%cond).

Since the Fu curve combines E_A and E_P it is helpful to look at those quantities individually with respect to P (Fig. 5.17). E_A tends to be high where P is high due to the availability of soil moisture (Fig. 5.17 a and b). E_P tends to be high where P is low (Fig. 5.17 c and d), due to higher surface temperatures (Fig. 5.18, particularly in the Equatorial region between 10°S and 10°N) and thus more available energy.

E_P increases with warming in the 'bucket' experiment as more energy becomes available at the surface (Fig. 5.17c and d). When stomatal conductance decreases with warming, E_P decreases, because potential evaporation takes changes in stomatal conductance into account. Just like E_P, E_A tends to increase in the 'bucket' simulation, and decrease when stomatal conductance is taken into account (Fig. 5.17a and b). E_A and changes in E_A are much smaller than E_P and changes thereof. E_P is an upper limit for E_A, because E_A is limited by soil moisture in addition to energy (represented by E_P).

Looking at the control P over idealised Africa and idealised America gives an indication as to why E_A becomes energy limited over the latter, while it remains moisture limited over the former. Figure 5.9b shows that the larger the continent is, the less P per unit area it receives. This is true for the control and perturbed ('bucket' and '50%cond') climates. The lower P, the more likely E_A is

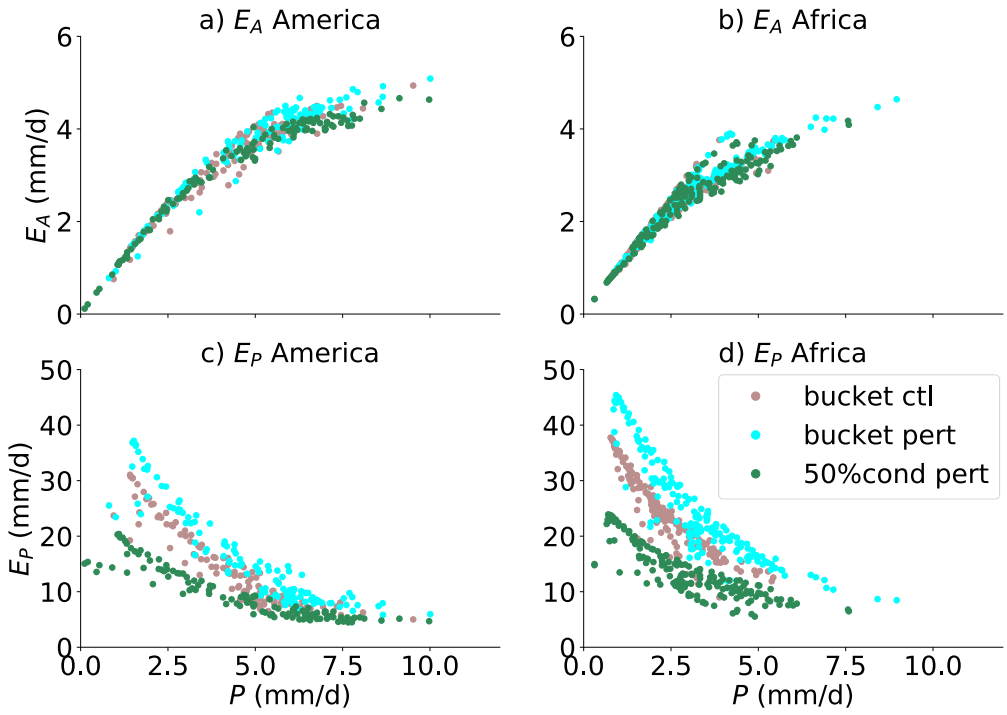

Figure 5.17: E_A and E_P versus P for all land points between 10°S and 10°N for AM and AF in the control simulation ('bucket ctl') and perturbed climates ('bucket pert' and '50%cond pert').

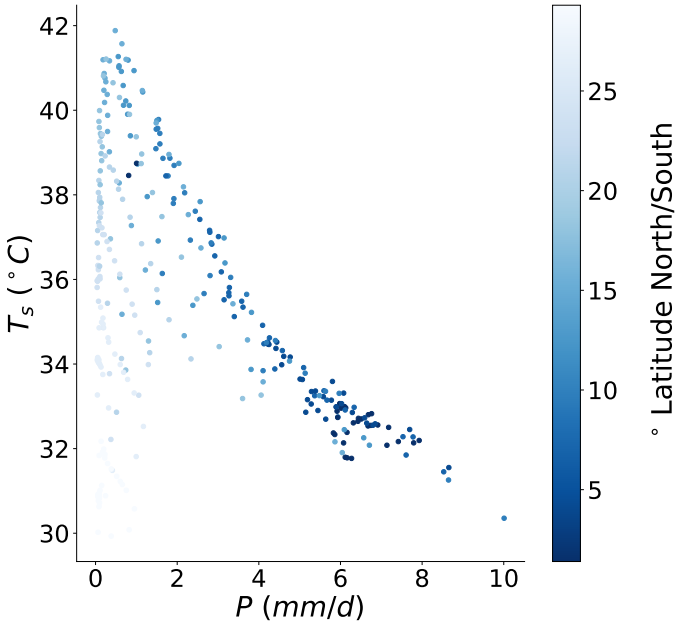

Figure 5.18: Relationship between P and T_S over land in the perturbed climate from the AM 'bucket' experiment. Marker colours indicate the latitude (North or South) with darker colours closer to the Equator and brighter colours further towards the subtropics.

to be moisture-limited ($E_P/P > 1$) rather than energy-limited ($E_P/P < 1$) for two reasons. A small amount of P leads to a greater value of E_P/P directly, as the denominator is small. In addition, surface temperatures – and thus E_P – over land tend to be high where P is low, particularly in the Equatorial region between 10°S and 10°N (Fig. 5.18).

If P increases in a region with low P_{ctl} (for example over Equatorial Africa, see Fig. 5.9b), then E_A increases proportionally. In this case, E_A is limited by the available soil moisture, and thus by rainfall. However, if P is already high in the control climate (as is the case for idealised Equatorial America) and thus soil moisture is abundant, a further increase in P does not result in an equivalent E_A increase. This is because evaporation becomes limited by the available energy (captured by E_P) rather than the available moisture (P).

Returning to the two continents experiment discussed at the start of this section, the strong P decrease over the idealised Amazon basin in the 2C '50%cond' experiment can be understood as a combination of local drying due to stomatal closure, and a remotely-forced drying due to circulation changes over Africa. In fact, the remotely forced and the local drying combine almost linearly to give the full P response (Fig. 5.19).

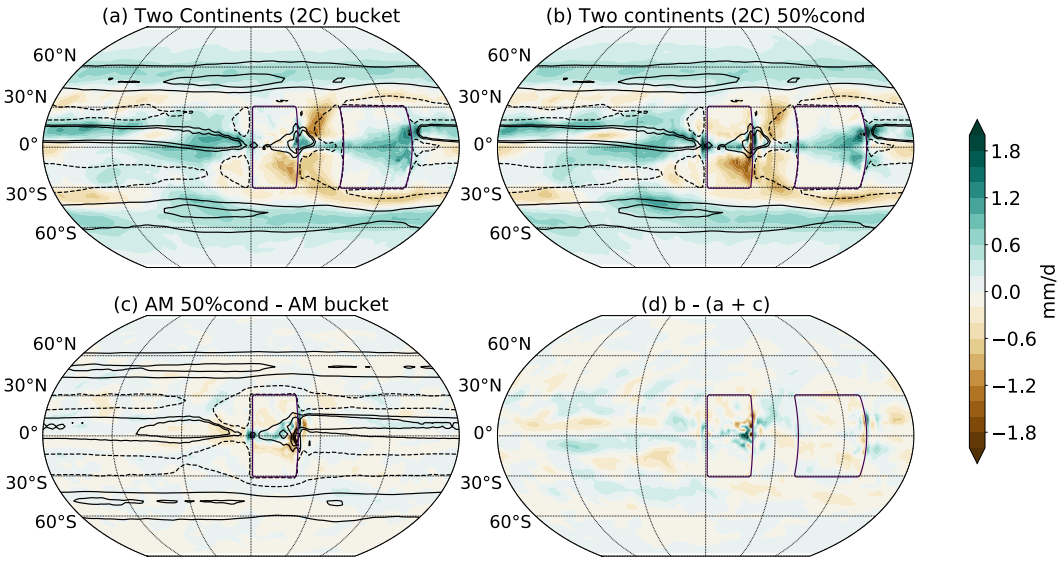

Figure 5.19: ΔP for a) 2C 'bucket', b) 2C '50%cond', c) AM '50%cond' - AM 'bucket', and d) the difference between the full experiment (2C '50%cond') and the linear addition (2C 'bucket' plus AM '50%cond' - AM 'bucket').

Adding ΔP from the two continents experiment without stomatal closure (2C

'bucket', Fig. 5.19a) to the ΔP over idealised America which is attributable to stomatal closure (Fig. 5.19c) gives a similar ΔP over the idealised Amazon basin as 2C '50%cond' (Fig. 5.19b) and the residual is small everywhere except for a small region close to the Equator, which is not the focus of the present study (Fig. 5.19d)[2]. The changes in the idealised Amazon basin thus seem to be mostly due to a combination of the ΔP changes in 2C bucket due to the teleconnection between idealised Africa and America (see Section 4.4) and local changes over idealised America due to stomatal closure.

When the Africa-sized continent is replaced by a second America-sized continent (2AM in Fig. 5.4) the drying influence of the East Continent on the idealised Amazon basin is much weaker (compare Fig. 5.20d to Fig. 5.10b). This is due to the fact that there is less subsidence and drying to the west of idealised America compared to idealised Africa (Fig. 5.21a,b). The weaker circulation response can also be inferred from the much weaker P decrease over the ocean to the west of the continent for idealised America than for idealised Africa (Fig. 5.20a,b). Therefore, the influence of an idealised American continent on the western American continent is smaller than that of an Africa-sized continent.

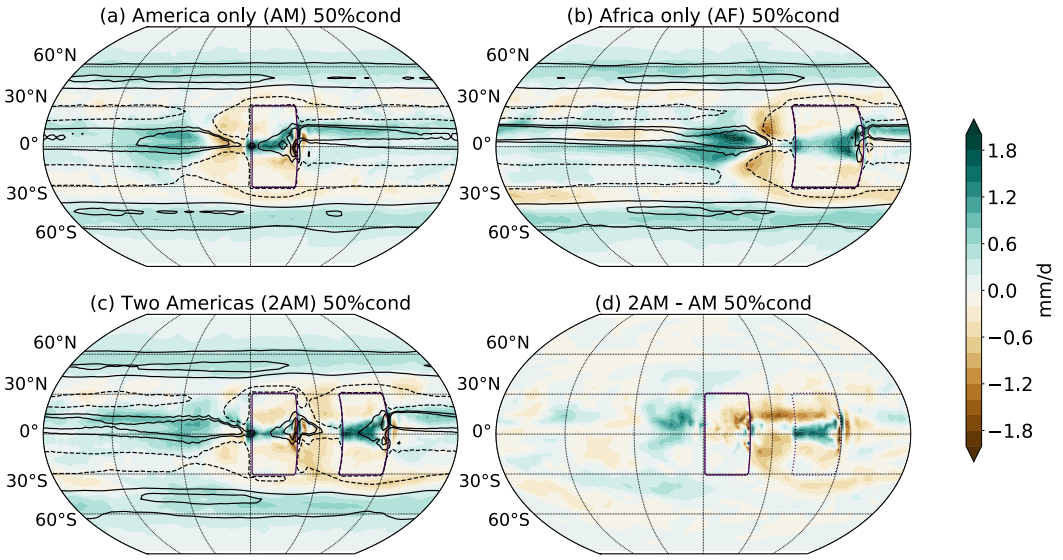

Figure 5.20: ΔP for a) AM, b) AF, c) 2AM and the drying influence of an America sized eastern continent on western AM (d) for the 50%cond experiment.

The hypothesis that lower E_P/P over parts of idealised America in '50%cond' compared to the 'bucket' experiment might partly explain a stronger P decrease

[2]Panel d is the same as Figure 5.10c but with opposite signs.

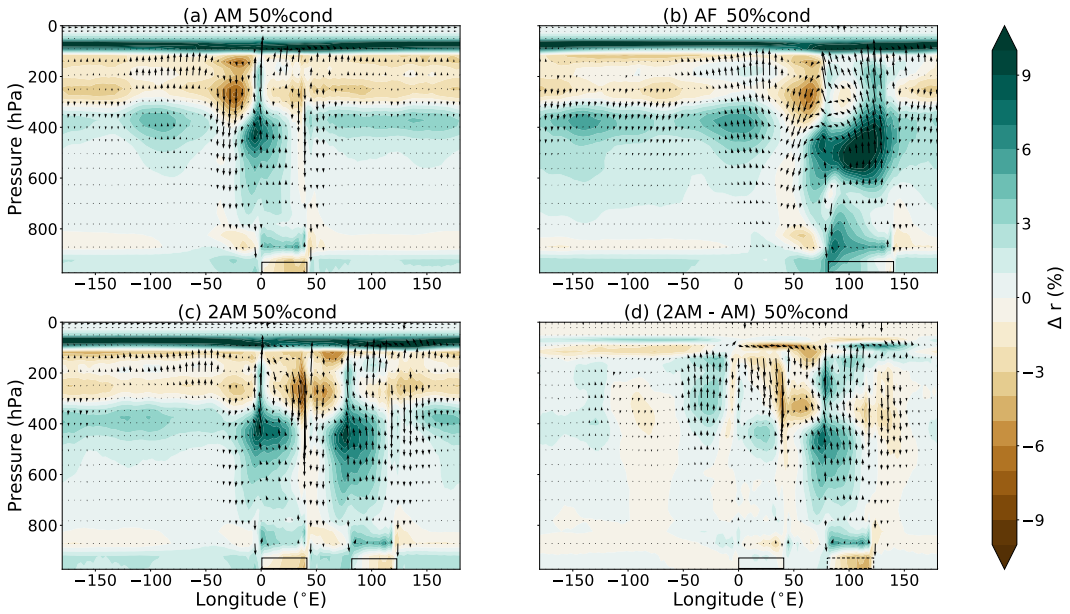

Figure 5.21: Warming-induced changes in r (colours, in absolute %) and zonal circulation (vectors, in m/s) averaged over 10°S - 10°N for a) AM, b) AF, c) 2AM and the difference between 2AM and AM (d) for the '50%cond' experiment. The boxes indicate the locations of the continents. The change in the vertical velocity has been amplified by a factor of 8000 following Nie et al. (2010).

over the idealised Amazon basin when stomatal closure is taken into account is investigated in a simulation with realistic continents and topography. In '50%cond', evaporation is close to the energy limit in the Eastern Amazon basin (Fig. 5.22c), but not in the 'bucket' experiment (Fig. 5.22b). In '50%cond', moisture convergence increases into the energy limited region and divergence increases elsewhere, particularly over northern South America (Fig. 5.23). Hence, a similar mechanism as outlined above for the idealised continents might contribute to the drying of parts of tropical South America in the realistic simulation.

The presence of topography and the other continents in the simulation with realistic continents will also likely influence P and thus also E_A over South America and Africa. As an intermediate step, the limits on E_A are shown for the 2C simulation in Figure 5.24. For the control and '50%cond' climates (Fig. 5.24a,c), the behaviour barely differs[3] from simply combining the two continents in Figure

[3]For the perturbed 'bucket' climate (Fig. 5.24b) the behaviour over idealised America in 2C does change compared to when the continent is on its own (Fig. 5.12), consistent with the fact that in isolation, idealised America receives more rainfall with warming in the 'bucket' case (see Fig. 5.4: AM 'bucket') and hence is more likely to be close to the energy limit (Fig. 5.12), whereas

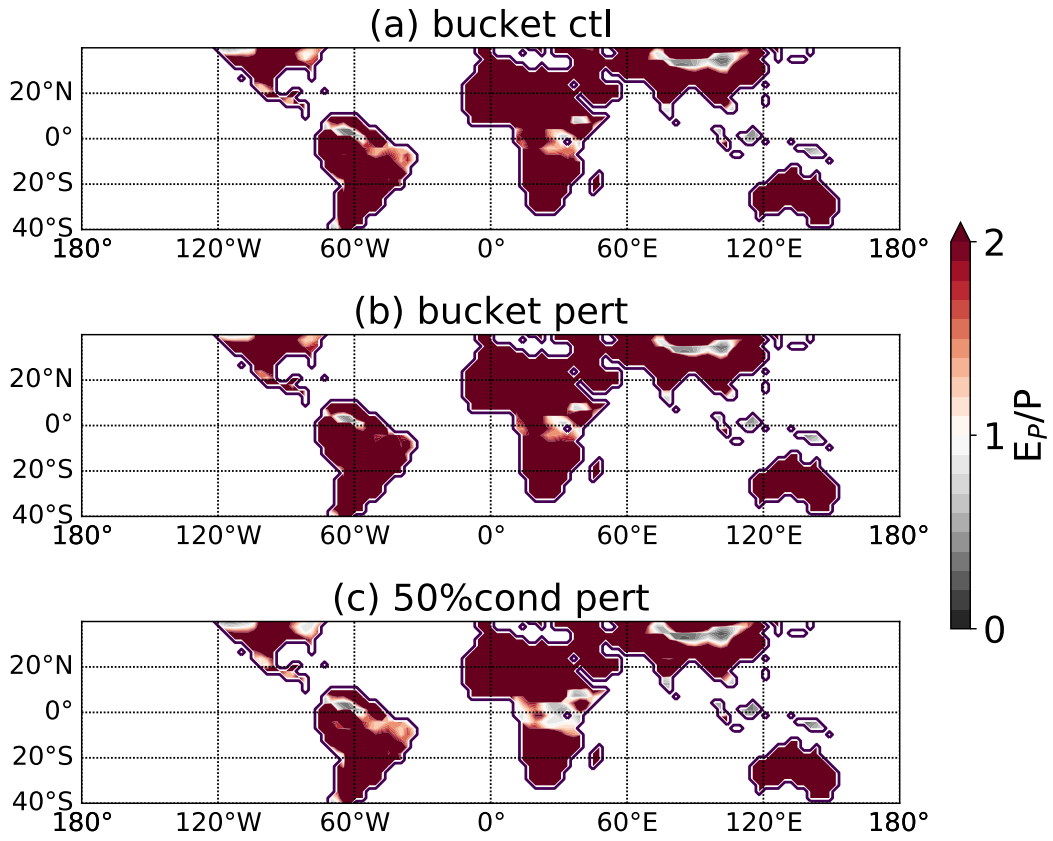

Figure 5.22: Moisture (red) and energy (grey) limited regions for RC a) in the control climate, b) in the perturbed 'bucket' and c) in the perturbed 50%cond climate. White areas lie between the moisture and energy limit.

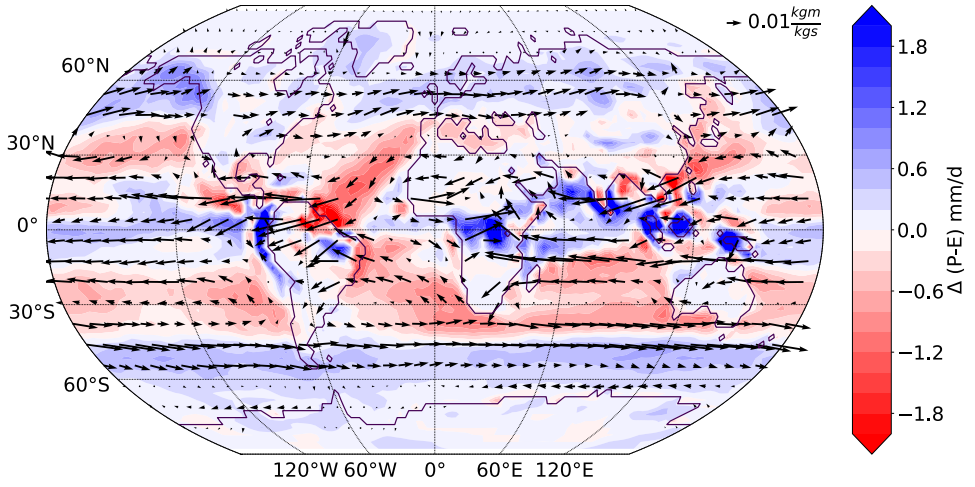

Figure 5.23: Colours show changes in column-integrated moisture flux convergence or $P - E$ (see Eq. 2.3) and arrows show 870hPa moisture flux for RC 50%cond.

5.12, while not quite capturing the behaviour of the realistic continents particularly over Equatorial Africa. Hence, topography and potentially other land masses might play an important role in setting the limits on evapotranspiration in the realistic continents case. In future work, the hypothesis will be tested in simulations with realistic South America and Africa in isolation with and without topography, in order to disentangle the contributions from topography and other continents.

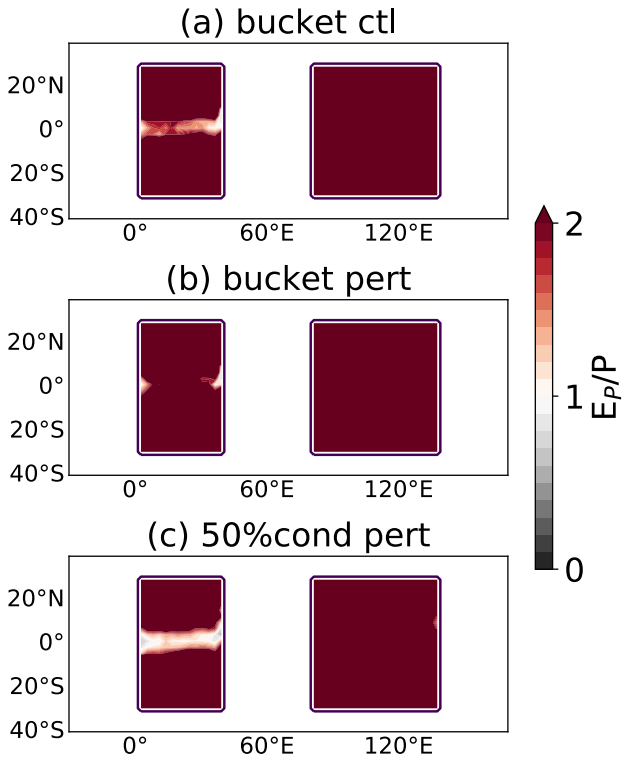

Figure 5.24: As in Figure 5.22 but for 2C.

5.6 Conclusions

The motivation for this chapter was to understand the projected amplification of the drying over the Amazon basin and wetting over the Maritime Continent in response to plant physiological changes (Kooperman et al., 2018; Chadwick et al., 2017; Skinner et al., 2017; Swann et al., 2016). Using Isca (Vallis et al., 2018 and see Section 3), we designed idealised Atmospheric General Circulation Models with realistic continents and idealised rectangular continents of varying width,

in combination with Africa, idealised America receives less rainfall with warming (see Fig. 5.4: 2C 'bucket', and Chapter 4) and hence is more likely to be moisture limited (Fig. 5.24b).

spanning the entire tropical band (30°S-30°N). A simple representation of vegetation was included in Isca, representing changes in stomatal conductance in response to CO_2 forcing.

In a simulation with realistic continents and topography, a 50% reduction in stomatal conductance with a doubling of CO_2 resulted in a stronger and more widespread drying over the Amazon basin and stronger wetting over the Maritime Continent than when the vegetation changes were neglected, in accordance with ESM projections. For one, this finding provides further evidence that the land-surface influences atmospheric processes (Shukla and Mintz, 1982; Bonan, 2008). This is similar to the findings from Chapter 4 concerning the impact of soil moisture-limited evaporation on continental precipitation. Furthermore, the strong drying over the Amazon basin in response to a decrease in stomatal conductance implies that deforestation in the Amazon basin could result in strong precipitation decreases (Spracklen et al., 2018, 2012; Wright et al., 2017), since removal of trees essentially corresponds to a very strong decrease in stomatal conductance (albeit evaporation from the soil and grass would still occur).

The simulations with two rectangular, flat continents representing Africa and America, and with a single narrow continent representing for example Sulawesi in the Maritime Continent showed a similar sensitivity of ΔP to vegetation changes compared to their realistic counterparts. This suggests that our idealised model simulations pose valuable tools for understanding the processes dominating precipitation change in the realistic simulations and in ESMs.

Somewhat surprisingly, the narrow continent experienced a stronger P increase when stomata were completely closed with warming (and thus no evaporation occurred over land) than when stomata remained open (allowing for moisture to be provided locally). Convection increased over the continent due to increasing surface temperatures caused by the lack of evaporation over land. The increase in convection led to moisture advection onto the island from the surrounding ocean. This finding confirms recent studies by Chadwick et al., 2019, Saint-Lu et al., 2019 and Kooperman et al., 2018.

In a simulation with idealised Africa and America and no change in stomatal conductance with warming, a Matsuno-Gill type circulation anomaly over idealised Africa leads to subsidence and drying over the idealised Amazon basin, as shown in Chapter 4. This teleconnection had roughly the same strength in

an experiment with the two idealised continents when stomatal conductance was reduced by 50% in the perturbed climate. The stronger drying over the idealised Amazon basin in the stomatal-closure experiment was therefore a combination of the remotely-forced drying and local changes.

Over idealised America in isolation, rainfall increased strongly along the Equator and to the north, but decreased in the idealised Amazon basin. Since evaporation near the Equator did not increase in-step with precipitation, humidity had to be provided by advection from surrounding land regions such as the idealised Amazon basin, inhibiting rainfall there. We hypothesised that high rainfall rates in the unperturbed climate could be the underlying reason for the weak increase in evaporation along the Equator and ultimately for the drying of the Amazon basin. The impact of the pre-industrial circulation regime over the Amazon basin has been shown to play a key role in projected P changes (Saint-Lu et al., 2019).

A similar mechanism as discussed above for the idealised continents was identified in the simulation with realistic continents, and might thus contribute to the projected drying of the Amazon basin in complex models. However, this hypothesis is yet to be tested in a complex GCM or in Isca in simulations with realistic South America and with realistic Africa in isolation and in combination with other continents in order to further disentangle local from remotely-influenced ΔP.

In this study, we have linked the stronger sensitivity of precipitation and evaporation over idealised Equatorial America compared to Equatorial Africa to high pre-industrial precipitation and a consequent shift of evaporation into the energy-limited regime over the former. However, the causality between stronger moisture convergence near the Equator and divergence in other parts of the Amazon basin remains unclear. In future work, we will use data with hourly instead of monthly resolution to investigate whether the $P - E$ increase at the Equator actually precedes the decrease in other parts of the Amazon basin causing drying there, or whether maybe the drying response occurs first.

Chapter 6

The land-sea contrast of tropical rainfall

In this chapter, we investigate the difference between rainfall over land and ocean in very idealised set-ups. This work was inspired by discussions with Prof. Dargan Frierson and also by input from Prof. David Battisti, Dr. Marysa M. Laguë and Dr. Brian Green during my visit to the University of Washington.

The key findings presented in this chapter are

1. The Matsuno-Gill theory cannot be used to interpret rainfall changes for a type of surface warming which is associated with a strong decrease in evaporation. Changes in the atmospheric energy budget provide a better framework in this case.

2. Seasonal rainfall migrates further poleward over land compared to ocean even when the thermal inertia is the same for both. This is connected to limited evaporation and thus strong sensible heating over land especially poleward of 10°.

3. The drying of the Amazon basin due to circulation changes over Africa is strongest when the two continents are roughly 40° apart as they are in the real world.

6.1 Introduction

Compared to ocean, land generally has a higher albedo and surface roughness, a lower thermal inertia, and – as discussed in previous chapters – more constrained evaporation. Over land, evaporation (E) is inhibited by the fact that there is less moisture available than over lakes or oceans, but also due to the resistance of the soil and vegetation to lose water to the atmosphere (Budyko, 1974, Manabe, 1969 and Sections 2.4 and 2.5).

The Matsuno-Gill theory of the tropical circulation states that introducing a surface heat source at the Equator leads to atmospheric ascent over the heating, and subsidence to the east and west, associated with a Kelvin and a Rossby wave, respectively (Gill, 1980 and Section 2.3). This theory has been used to relate strong rainfall over one continent to dry conditions over a land mass to the west (Cook et al., 2004; Rodwell and Hoskins, 1996), and rainfall changes over Africa to drying over the Amazon basin (Pietschnig et al., 2019; Kooperman et al., 2018). As stated by Gill (1980), the tropical continents can be considered such sources of surface heating. Due to limited evaporation over land, the absorbed shortwave radiation is mostly balanced by sensible heat and upwelling longwave radiation, leading to higher surface temperatures (Manabe et al., 1991; Dong et al., 2009).

While changes in surface temperatures have been shown to be a good indicator of tropical circulation and precipitation changes over ocean (the 'warmer-get-wetter' hypothesis, see Section 2.2, Xie et al., 2010 and Chadwick et al., 2014), this framework is less applicable over land. This is partly due to the fact that not only temperature but also relative humidity changes affect ΔP over land (Maroon et al., 2016; Chadwick et al., 2016; Byrne and O'Gorman, 2016; Lambert et al., 2017). The moist static energy (MSE) budget of the atmosphere provides a more comprehensive framework for understanding the distribution of precipitation under a climate perturbation (Maroon et al., 2016; Neelin and Held, 1987; Bischoff and Schneider, 2014; Boos and Korty, 2016; Wei and Bordoni, 2018; Seo et al., 2017), since the moist static energy

$$h = c_p T + g z + L q \tag{6.1}$$

takes temperature (T), humidity (q) and potential energy (z) into account (see Eq. 2.4). In this equation, c_p is the heat capacity of dry air at constant pressure

($\approx$ 1004 J/(kg $\cdot$ K)), $g \approx 9.81$ m/s^2 is the gravitational acceleration on Earth and L is the latent heat of vapourisation ($\approx 2.45 \cdot 10^6$ J/kg).

Maroon et al. (2016) showed that when a subtropical continent is placed on an aquaplanet in the Northern Hemisphere (NH), the NH becomes warmer than the Southern Hemisphere (SH), but the ITCZ shifts into the SH. Based on the notion that surface temperatures control the location of the ITCZ, one would expect a shift of the tropical rain band into the Northern Hemisphere. The Northern Hemisphere gets warmer both over land and ocean due to limited evaporation over the continent. In spite of the temperature increase, the moist static energy of the Northern Hemisphere is lower than that of the Southern Hemisphere. Therefore, the ITCZ shifts into the energetically richer Southern Hemisphere, showing that the energy budget of the atmosphere is a more useful framework than temperatures alone.

As discussed in Section 2.8, the convergence of the vertically integrated low-level horizontal wind ($-\nabla.\mathbf{v}_{h,2}$) and the net energy input to the atmosphere (F_{net}) are related via the gross moist stability δh through

$$-\delta h \nabla.\mathbf{v}_{h,2} \simeq F_{net} \tag{6.2}$$

(see Eq. 2.14, Neelin and Held, 1987). If the gross moist stability can be assumed to be constant under a climate perturbation, ΔF_{net} should be proportional to $\Delta(-\nabla.\mathbf{v}_{h,2})$ and thus ΔP in the tropics (Neelin and Held, 1987). Several studies have successfully applied this energetic framework to changes in rainfall by relating shifts in the ITCZ to changes in the atmospheric energy transport (Frierson and Hwang, 2012; Donohoe et al., 2013). However, changes in δh cannot always be neglected, as shown by Seo et al. (2017) and Wei and Bordoni (2018) for aquaplanet simulations (see Section 2.8).

In recent decades, theories of the monsoon have started to shift away from the classic 'large-scale land-sea breeze' paradigm towards the perception that monsoons are a regional manifestation of the seasonal migration of the ITCZ over land (Geen et al., 2020; Hill, 2019), particularly since monsoon-type behaviour has been observed in aquaplanet simulations (Bordoni and Schneider, 2008, Wei and Bordoni, 2018, Geen et al., 2018 and Section 2.9).

The moist static energy budget of the atmosphere also proves useful for understanding the seasonal migration of the ITCZ over land and over ocean. Privé and

Plumb (2007) showed that the tropical precipitation peak tends to be located near or slightly equatorward of the peak in near-surface moist static energy (MSE_b).

In Chapter 4 (and Pietschnig et al., 2019), we showed that enhanced ascent and rainfall over Equatorial Africa leads to drying over the Amazon basin via a Matsuno-Gill type teleconnection under a doubling of CO_2. As mentioned in Cook et al. (2004) for the pre-industrial climate, the proximity between Africa and South America makes a teleconnection between the two continents possible. This begs the question how this teleconnection changes with increasing or decreasing distance between Africa and South America.

In this chapter, the basic mechanisms which control rainfall over land and ocean are investigated using the modeling framework 'Isca' to design idealised Atmospheric General Circulation Model experiments (Vallis et al., 2018 and see Section 3). The chapter is structured as follows: In the methods section, the theory for relating low-level convergence and thus tropical rainfall to the atmospheric energy budget is briefly outlined (a detailed discussion can be found in Section 2.8), followed by a description of the simulations used here. The findings are presented in four sections: In Section 6.3, four different types of surface warming are studied with aquaplanets or with one rectangular, flat tropical continent. In Section 6.4, rainfall changes for the different surface warming experiments are connected to changes in the atmospheric energy budget. In Section 6.5, the seasonal migration of the ITCZ over land and ocean is investigated in terms of the near-surface moist static energy. In the last results section, the impact of two rectangular continents representing Africa and America on each other is studied in a series of 'continental drift' experiments. In the final section, the results from this chapter are summarised and ideas for future research are presented.

6.2 Methods

The column-integrated moist static energy flux divergence (F_{MSE}) is given by

$$\int_0^{p_S} \nabla.\overline{(h\mathbf{v})}\frac{dp}{g} = F_{MSE} = F_{net} \tag{6.3}$$

where h is the moist static energy, $\mathbf{v}$ is the three-dimensional wind vector and F_{net} is the net energy input to the atmospheric column through the top of the

atmosphere and the surface (see Section 2.8). The integration is performed from $p = 0$ at the top of the atmosphere to the surface ($p = p_S$), overbars denote time means. The overbar has been omitted from F_{MSE} and F_{net} but these quantities denote time means.

Using the Reynolds decomposition on $\overline{h\mathbf{v}}$ yields

$$\int_0^{p_S} \nabla.(\overline{h}\overline{\mathbf{v}} + \overline{h'\mathbf{v}'})\frac{dp}{g} = F_{MSE} = F_{net} \tag{6.4}$$

where primes denote deviations from the time mean. Further, in pressure coordinates $\nabla.\mathbf{v} = 0$ (Holton, 2004, p.59), and so

$$\int_0^{p_S} \overline{\mathbf{v}}.\nabla\overline{h} + \nabla.(\overline{h'\mathbf{v}'})\frac{dp}{g} = F_{MSE} = F_{net}.$$

(e.g. Hill et al., 2017). Since $h = c_pT + gz + Lq$ (Eq. 6.1), this can be split into the contributions from each component to the total divergence of F_{MSE}:

$$F_{c_pT} = c_p \cdot \int_0^{p_S} \overline{\mathbf{v}}.\nabla\overline{T} + \nabla.(\overline{T'\mathbf{v}'})\frac{dp}{g} \tag{6.5}$$

$$F_{gz} = g \cdot \int_0^{p_S} \overline{\mathbf{v}}.\nabla\overline{z} + \nabla.(\overline{z'\mathbf{v}'})\frac{dp}{g} \tag{6.6}$$

$$F_{Lq} = L \cdot \int_0^{p_S} \overline{\mathbf{v}}.\nabla\overline{q} + \nabla.(\overline{q'\mathbf{v}'})\frac{dp}{g} \tag{6.7}$$

so that $F_{c_pT} + F_{gz} + F_{Lq} = F_{MSE} = F_{net}$. The first two terms are often combined to give F_{DSE}, the contribution from dry static energy to the total moist static energy flux divergence (Trenberth and Stepaniak, 2003; Pierrehumbert, 2002).

In the present study, the gross moist stability (δh) is defined as

$$\delta h = \frac{F_{net}}{-\nabla.\mathbf{v}_{h,2}}. \tag{6.8}$$

In contrast to the original definition by Neelin and Held (1987) (see Eq. 6.2 and Section 2.8), the eddy and advective terms of F_{MSE} are taken into account (similar to the definition in Inoue and Back, 2015 or Kang et al., 2009). Thus, since $F_{MSE} = F_{net}$ (see Section 2.8 and Eq. 6.3) we can use the '=' sign here in Equation 6.8 instead of the original '$\simeq$' in Equation 6.2 (Neelin and Held, 1987).

The mass flux divergence in the bottom layer of the atmosphere ($\nabla.\mathbf{v}_{h,2}$), is calculated as

$$\nabla.\mathbf{v}_{h,2} = \int_{p_M}^{p_S} \nabla.\overline{\mathbf{v}_h}\frac{dp}{g} \tag{6.9}$$

(see Eq. 2.8). The mid-tropospheric level p_M, up to which the mass flux divergence is integrated, is defined as the pressure at which the mass streamfunction reaches its maximum (e.g. Wei and Bordoni, 2018). In our simulations, p_M lies between 300 and 350 hPa (similar to Geen et al., 2018 and Thomson and Vallis, 2019 but different to the 700 - 550 hPa used by Kang et al., 2009).

6.2.1 Model Simulations

In this chapter, the atmospheric GCM modelling framework 'Isca' (Vallis et al., 2018 and Section 3) is employed to study simulations without and with seasons. The simulations for this chapter are summarised in Table 6.1.

For the simulations without seasons, an annual mean insolation profile is imposed where the cosine of the solar zenith angle (θ_s) is given by:

$$cos(\theta_s) = 0.25 \cdot [1 + \frac{\Delta_s}{4} \cdot (1 - 3sin^2(\theta))] \tag{6.10}$$

following Frierson et al. (2006). Here, θ is the latitude, and the constant Δ_s determines the meridional temperature gradient. In our simulations, $\Delta_s = 0.95$ best approximates the annual mean insolation profile. This is similar to a 'perpetual equinox' simulation. However, in the latter the temperature gradient between the poles and Equator is stronger than with an annual-mean insolation profile and thus less representative of Earth's climate.

In the first set of simulations ('without seasons'), we use the annual-mean insolation profile and a 20m deep mixed-layer ocean with an albedo of $\alpha_{oc} = 0.25$. In contrast to Chapters 4 and 5 where sea surface temperatures (SSTs) were mostly prescribed, the ocean is free to respond to the energy input from the Sun. This is the control aquaplanet simulation (AP).

In order to study the impact of a warm surface temperature anomaly on the atmospheric circulation we introduce four different perturbations to the system. In the first surface warming experiment, the albedo of a patch of ocean from the AP simulation is reduced to $\alpha = 0.1$ ('AP-dark-patch'). The dark patch is shaped like the idealised American continent (AM) from Chapters 4 and 5, spanning 40°

longitude and extending from 30°South to 30°North. In the second simulation, a patch of ocean is replaced by a continent shaped like AM ('AM-same'). In this simulation, land and ocean have the same albedo ($\alpha_L = 0.25 = \alpha_{oc}$) and heat-capacity (equivalent to that of a 20m deep mixed-layer ocean). Hence, the only difference between land and ocean is the fact that evaporation over land is limited by the available soil moisture through the bucket model (Manabe, 1969 and see Section 3.2). In the third warming scenario 'AM-same-2xCO_2', the CO_2 concentration is doubled from 300 ppm to 600 ppm in AM-same. In the last experiment ('AM-dark'), the continent from AM-same is darkened ($\alpha_L = 0.1$), but the bucket hydrology is still used and land and ocean have the same thermal inertia.

In an experiment with seasons, we investigate the impact of the seasonal migration of the Sun on rainfall over land and ocean in the 'AM-same' set up ('seasons-AM-same'). As described above, the only difference between land and ocean is the higher evaporative resistance over land due to the bucket model, while albedo and heat capacity of the land are the same as over the ocean.

In our final set of experiments, the configuration with two idealised continents representing Africa and America from Chapter 4 is revisited. In order to study the length-scale of the Matsuno-Gill type teleconnection between the two continents, three additional experiments are conducted in which idealised America is located 10° ('2C 10°'), 70° ('2C 70°') and 100° ('2C 100°') longitude to the west of idealised Africa. Those simulations are compared to our original '2C' experiment from Chapter 4 where the two continents are located approximately the width of the Atlantic Ocean apart (40° longitude). As in our original set-up, a zonally uniform SST climatology derived from the Atmospheric Model Intercomparison Project (AMIP, Gates, 1992) SSTs is prescribed (see Fig. 3.1), land albedo is 1.3 times the ocean albedo ($\alpha_L = 0.33$) and the bucket hydrology is used (but no stomatal closure).

Name	Continents	Hydrology	Ocean	Perturbation
'without seasons' : annual-mean insolation profile				
AP	Aquaplanet	none	20m slab, α_{oc} = 0.25	None
AP-dark-patch	Aquaplanet	none	20m slab, α_{oc} = 0.25	AM-shaped dark patch (α = 0.1)
AM-same	AM with α_L=0.25 & 20m heat cap.	none / bucket	20m slab, α_{oc} = 0.25	AM-same on AP
AM-same-2xCO_2	AM-same	bucket	20m slab, α_{oc} = 0.25	2xCO_2
AM-dark	AM-same	bucket	20m slab, α_{oc} = 0.25	α_L=0.1
'seasons' : seasonally varying insolation				
seasons-AM-same	AM-same	bucket	20m slab, α_{oc} = 0.25	None
'continental drift' experiments				
2C10	AM + AF at 10° distance α_L = 0.33 & 2m heat cap.	bucket	zon. symm. SSTs	2xCO_2 + 2.52K
2C	AM + AF at 40° distance	bucket	zon. symm. SSTs	2xCO_2 + 2.52K
2C70	AM + AF at 70° distance	bucket	zon. symm. SSTs	2xCO_2 + 2.52K
2C100	AM + AF at 100° distance	bucket	zon. symm. SSTs	2xCO_2 + 2.52K
Supercontinent	flat rectangle, width = 100° longitude	bucket	zon. symm. SSTs	2xCO_2 + 2.52K

Table 6.1: Experimental set-ups used in Chapter 6 in order of their appearance.

6.3 Precipitation changes for different types of surface warming

In the simplest 'warming' experiment where the albedo of a patch of ocean is reduced (AP-dark-patch), an increase in P occurs over the heat source (Fig. 6.1a). Replacing a patch of ocean with land (AM-same) might be expected to exhibit an increase in rainfall as well, since surface temperatures over land tend to be higher than over ocean due to limited evaporation (Dong et al., 2009), and Gill (1980) mentioned in their paper that the tropical continents can be regarded as surface heat sources. However, P decreases over land in this simulation (Fig. 6.1b).

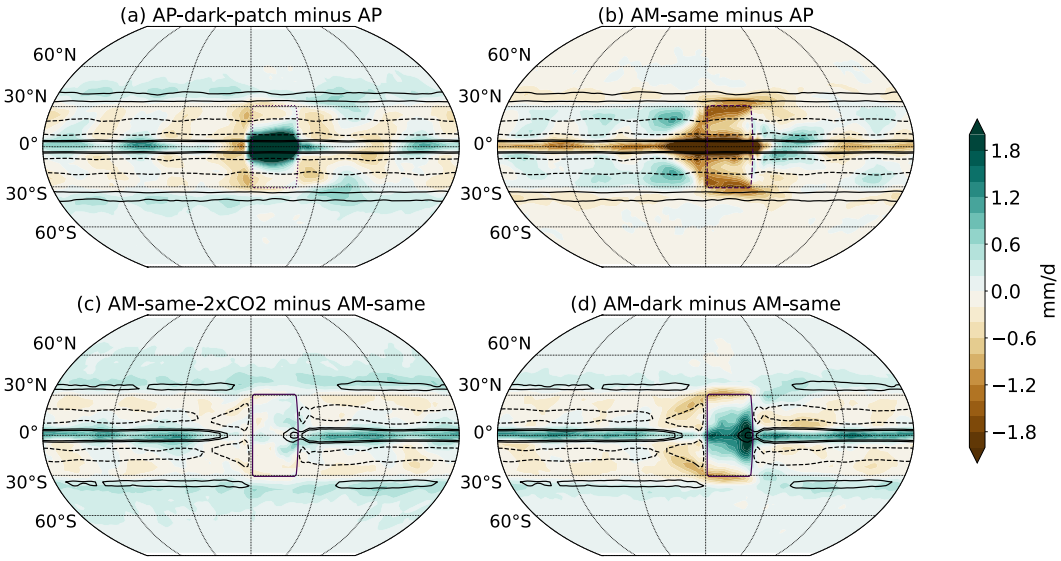

Figure 6.1: Annual mean ΔP for the four warming scenarios: a) darkening an AM-shaped patch of ocean, b) replacing a patch of ocean with an AM-shaped continent, c) doubling CO_2 and d) darkening AM. Contours show control $P - E$ of -2 (dashed), 1 and 2 (solid) mm/day. The rectangular dotted, dashed and solid contours indicate the shape of the idealised American continent.

The AP-dark-patch simulation is a perfect example of a Matsuno-Gill type circulation anomaly. Surface heating leads to convection and precipitation, due to the increases in near-surface relative humidity (r) and specific humidity (q) above the boundary layer (Figs. 6.2a and 6.3a). In contrast, when the same patch of ocean is replaced by a land surface, r and q decrease significantly in the atmospheric column above the continent (Figs. 6.2b and 6.3b), and P decreases (Fig. 6.1b). Instead of stronger ascent, there is anomalous subsidence onto the

continent, despite the fact that near-surface temperatures increase over land (Fig. 6.4b). Hence, the Matsuno-Gill theory is not applicable in this case.

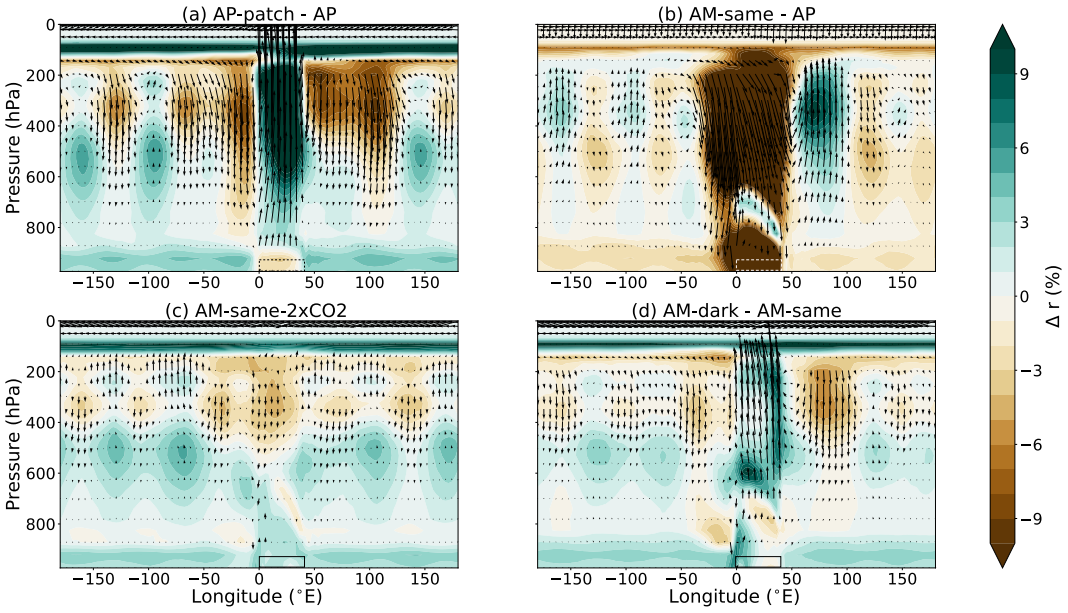

Figure 6.2: Changes in relative humidity r (colours, in absolute %) and the zonal circulation (vectors, in m/s) averaged over 10°S - 10°N for the four surface-warming experiments from Fig. 6.1. Contours near the surface indicate the location of the dark ocean patch in (a) and the continent in (b-d). The change in the vertical velocity has been amplified by a factor of 8000 following Nie et al. (2010).

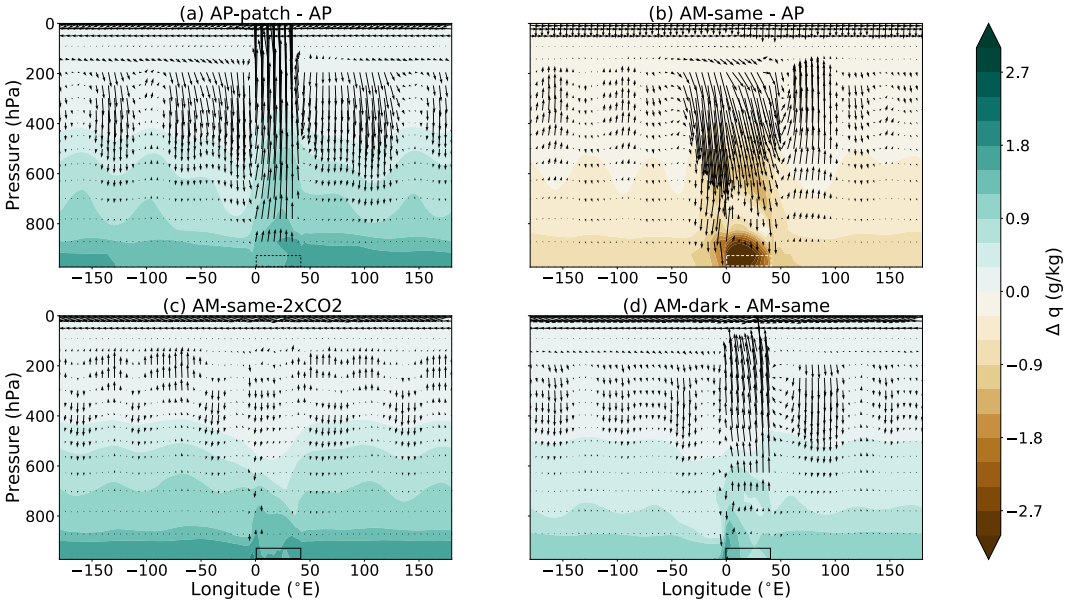

Figure 6.3: Same as Fig. 6.2 but for changes in specific humidity (Δq, in g/kg).

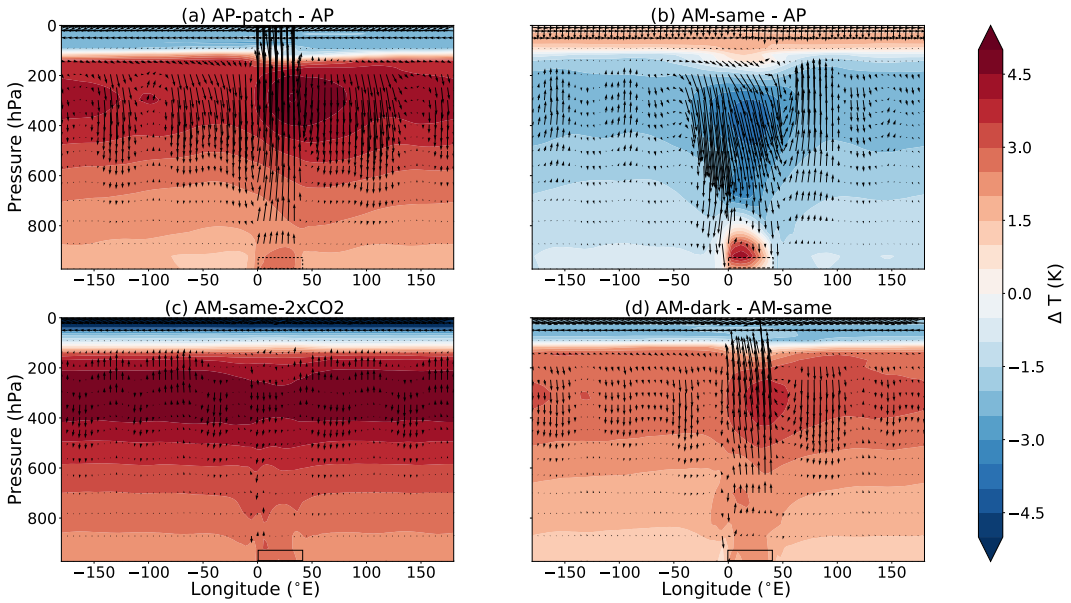

Figure 6.4: Same as Fig. 6.2 but here colours show the temperature changes (ΔT, in Kelvin).

In the case of a doubling of CO_2 for a set-up with one rectangular continent (AM-same-2xCO_2), P increases slightly (Fig. 6.1c). This experiment is different to the one where ocean is replaced by land, because humidity increases over the surface heat source instead of decreasing (Figs. 6.2c and 6.3c). It is therefore conceptually more similar to AP-dark-patch, and the Matsuno-Gill theory is applicable. The circulation is enhanced by the doubling of CO_2 and precipitation increases. This behaviour is also similar to the circulation anomalies discussed in Chapter 4. Note that although the mechanism is similar, this simulation is not directly comparable to the results presented in Chapter 4, because there are no seasons and because there is no inter-hemispheric asymmetry in the annual mean SST distribution (i.e. the maximum is at the Equator, not in the Northern Hemisphere). In addition, land and ocean have the same albedo (and heat capacity, but this is not of central importance due to the absence of seasons). This experiment is also different to the other three warming scenarios, because the forcing is globally uniform and relatively weak, whereas in the other experiments the forcing applies to the AM-shaped patch only and is comparatively strong.

In the last 'warming' scenario, the AM-shaped continent is heated by reducing its albedo (AM-dark), which leads to a clear increase in P (Fig. 6.1d). Conceptually, this case is again similar to darkening a patch of ocean, with similar albeit

weaker increases in convection, mid-tropospheric r, and q and T throughout the column (Figs. 6.2 - 6.4 d). In summary, the Matsuno-Gill theory is applicable in all cases where q does not decrease in the column above the warm surface temperature anomaly. This makes sense in light of the fact that the Matsuno-Gill theory is based on the dry shallow-water equations, and thus does not take changes in the atmospheric moisture content into account (Maher et al., 2019).

6.4 Precipitation from an energetic perspective

The moist static energy budget is a useful framework for understanding the rainfall changes in the four surface warming experiments. For example, when ocean is replaced with land, near-surface T over AM increases more strongly than in the other warming experiments (Fig. 6.4), but rainfall decreases. Hence, changes in temperature alone are not a good metric for understanding changes in P (Maroon et al., 2016). Instead, the energy budget of the atmospheric column should be considered.

Before investigating ΔF_{MSE} and the individual terms contributing to it (see Eqs. 6.5 - 6.7), the terms are discussed for AP and AM-same in the zonal mean (Fig. 6.5). Similar to Trenberth and Stepaniak (2003) we find that in the AP and AM-same climates, in the Equatorial region between roughly 10°S and 10°N, F_{Lq} converges towards the Equator and F_{DSE} diverges away. This is due to the fact that the Hadley circulation transports moisture from the subtropics towards the Equator in its lower branch and dry static energy from the tropics to the subtropics in the upper branch (Fig. 6.7 and Pierrehumbert, 2002). As expected from Trenberth and Stepaniak (2003), F_{c_pT} and F_{gz} – which together give F_{DSE} – are of similar magnitude, but of opposite signs. When the zonal average is taken over the location of idealised America only, the energy flux divergences exhibit the same behaviour as in the global zonal mean, but the terms are of much smaller magnitude over land than over ocean (Fig. 6.6).

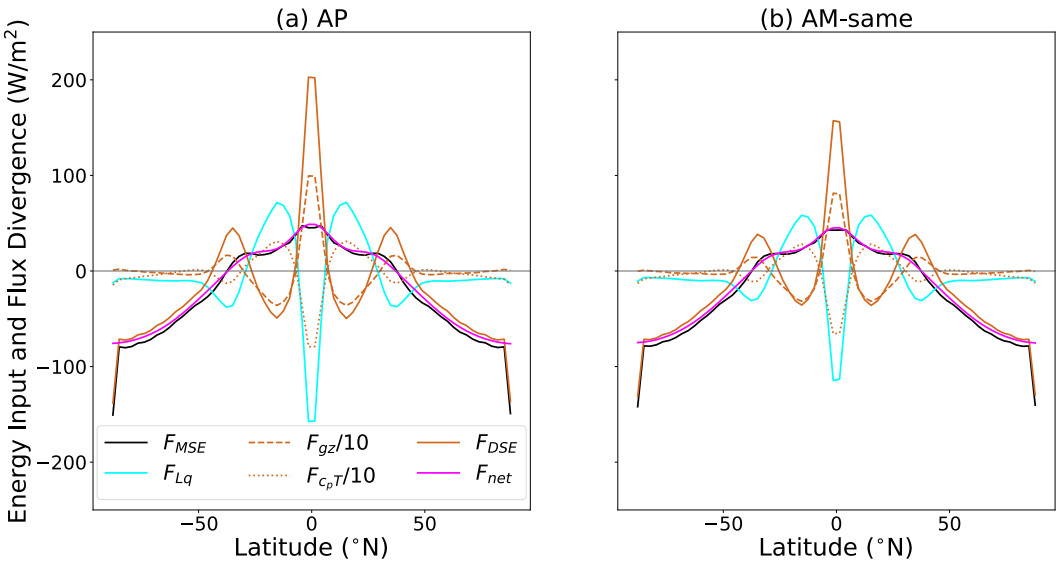

Figure 6.5: Zonal mean, annual mean terms of the column-integrated moist static energy flux divergence in W/m^2 for a) AP and b) AM-same. F_{MSE} (black) is the total flux divergence, which is almost equal to F_{net} (magenta), the net energy input to the atmosphere. F_{Lq} (cyan) is the latent heating component of F_{MSE}. The dry static energy component F_{DSE} (brown, solid) has been split here into the sensible heating (F_{c_pT}, brown, dashed) and potential energy (F_{gz}, brown, dotted) terms, both of which have been scaled by a factor of 1/10 for better visualization.

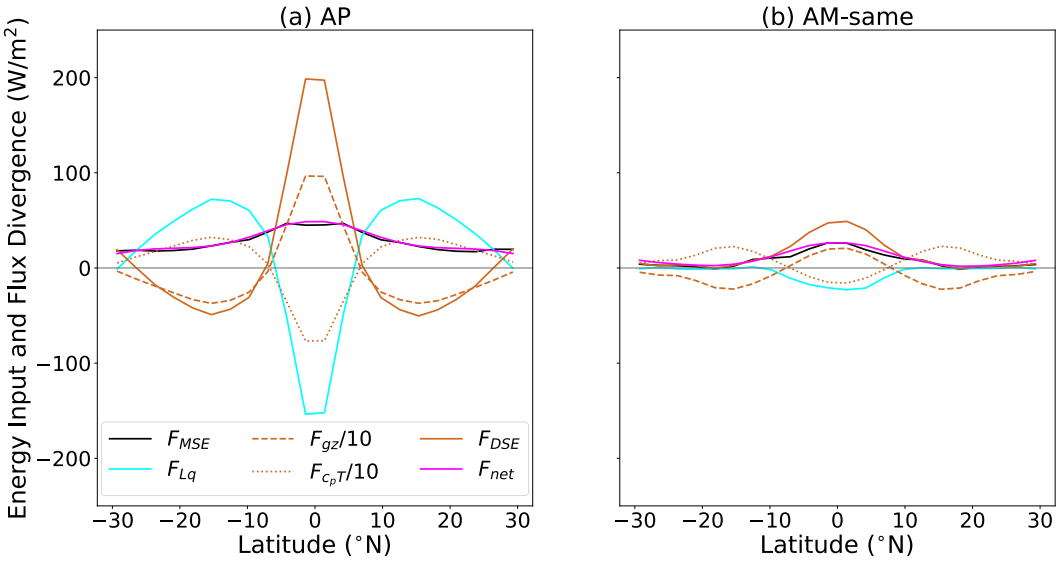

Figure 6.6: As in Figure 6.5, but the zonal average is taken over the location of the idealised American continent only.

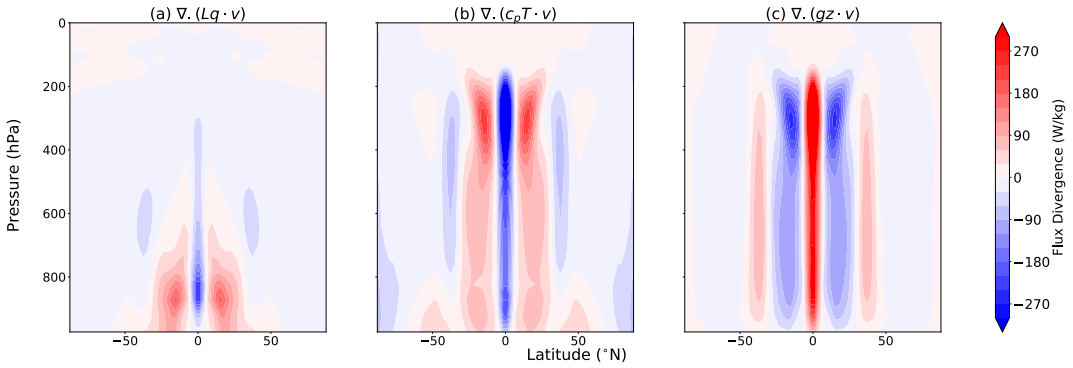

Figure 6.7: Vertical profiles of the zonal mean moist static energy flux divergence components a) $\nabla.(Lq \cdot \mathbf{v})$, b) $\nabla.(c_p T \cdot \mathbf{v})$ and c) $\nabla.(gz \cdot \mathbf{v})$ for the AP simulation. Red areas are regions of flux divergence, blue areas are regions of flux convergence.

If the gross moist stability can be assumed to be constant under a climate perturbation, Equation 6.8 suggests that ΔF_{net} – and thus ΔF_{MSE} (Eq. 6.3) – should be proportional to ΔP in the tropics. Our results suggest that ΔP is in fact related to ΔF_{MSE} over the source of surface warming, both in the zonal mean (Fig. 6.8) and on a regional scale (Fig. 6.9). In the Equatorial region, ΔP is positive/negative where ΔF_{MSE} is positive/negative, albeit the changes in AM-same-2xCO_2 (Fig. 6.8c) are very small.

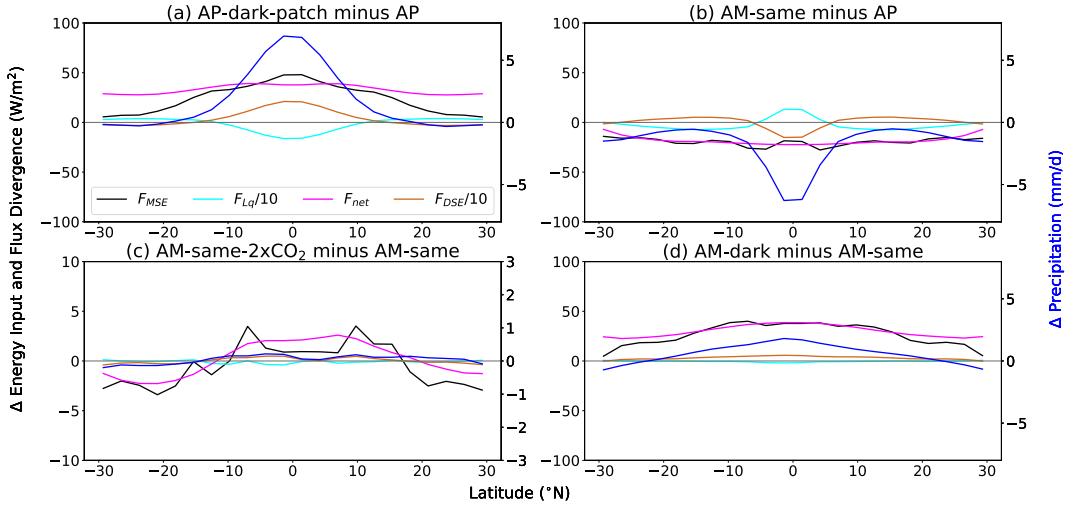

Figure 6.8: Zonal mean changes in F_{MSE} (black), F_{Lq} (cyan), F_{DSE} (brown), F_{net} (magenta) and P (blue, right y-axis) for the four warming experiments. The zonal mean is taken only over the dark patch (a) or over land (b-d). Note the much smaller range on the y-axis in panel c.

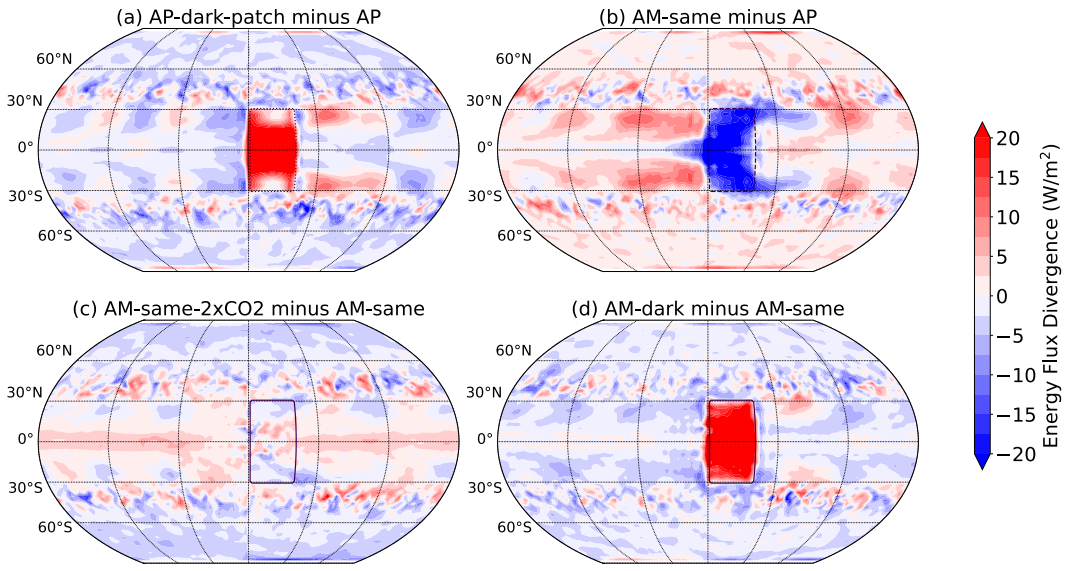

Figure 6.9: Changes in F_{MSE} for the four warming experiments.

In order to further assess whether ΔP is likely to be driven mostly by ΔF_{net} or by changes in δh in our simulations (see Eq. 6.8), we first show that ΔP is proportional to $\Delta(-\nabla.\mathbf{v}_{h,2})$. Figure 6.10 shows that these two quantities are well correlated over the warm surface temperature anomaly. Next, $\Delta(-\nabla.\mathbf{v}_{h,2})$ is correlated with ΔF_{net} (Fig. 6.11) and with changes in δh (Fig. 6.12). The correlation between $\Delta(-\nabla.\mathbf{v}_{h,2})$ and ΔF_{net} is significantly higher than the correlation between $\Delta(-\nabla.\mathbf{v}_{h,2})$ and $\Delta(\delta h)$, suggesting that the rainfall changes might be dominated by changes in F_{net} rather than changes in δh.

Looking at the changes in F_{net} over the warm surface temperature anomaly for AP-dark-patch, AM-same-2xCO_2 and AM-dark (Figs. 6.8a, c, d and 6.9a, c, d), all three show the same signs of change in F_{MSE} and its components. The change in each term of F_{MSE} is simply an amplification of the respective unperturbed climates (Fig. 6.6). For example the convergence of latent heat flux increases (i.e. F_{Lq} decreases) as more moisture converges towards the Equator.

In contrast, when a patch of ocean is replaced by land, moisture convergence towards the Equator decreases (Fig. 6.8b). This means that F_{Lq} increases (more divergence) and F_{DSE} decreases. Thus, despite the strong increase in surface temperatures (see Fig. 6.4b), the total energy flux divergence (F_{MSE}) – and equivalently (by Eq. 6.3) the net energy input to the atmosphere (F_{net}) – in the region decreases and so does the precipitation.

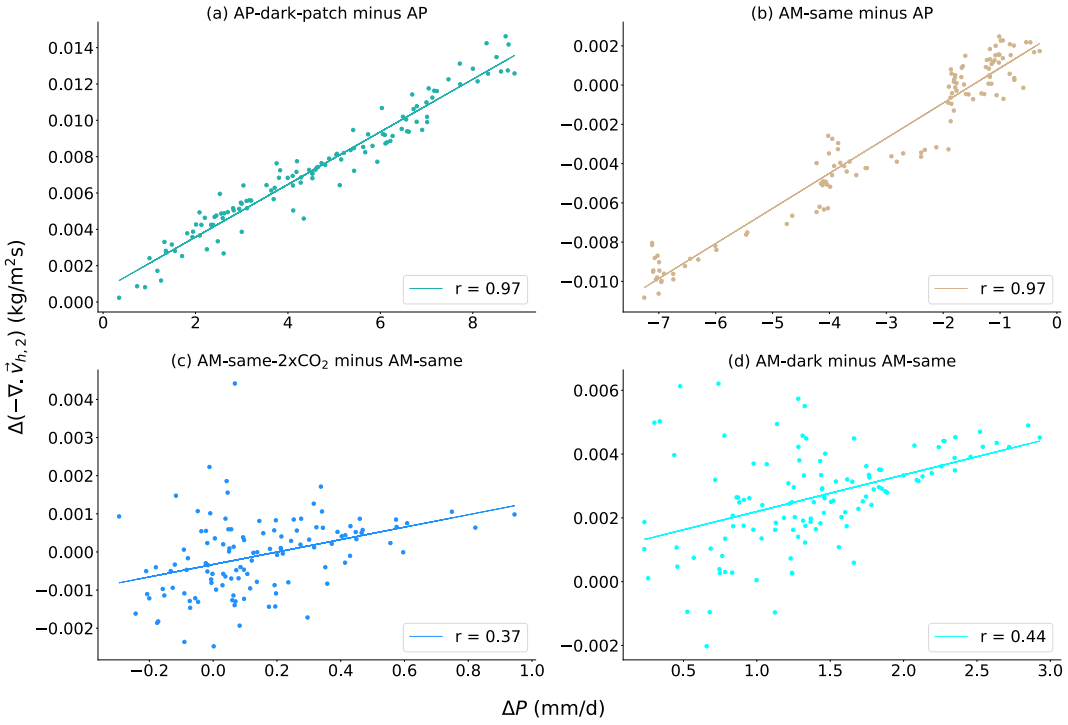

Figure 6.10: Correlation between changes in P (x-axis) and changes in $-\nabla.\mathbf{v}_{h,2}$ (y-axis) for all four warming experiments over a) the dark patch and over land (b-d) between 10°S and 10°N. p-values are less than $3{\cdot}10^{-5}$.

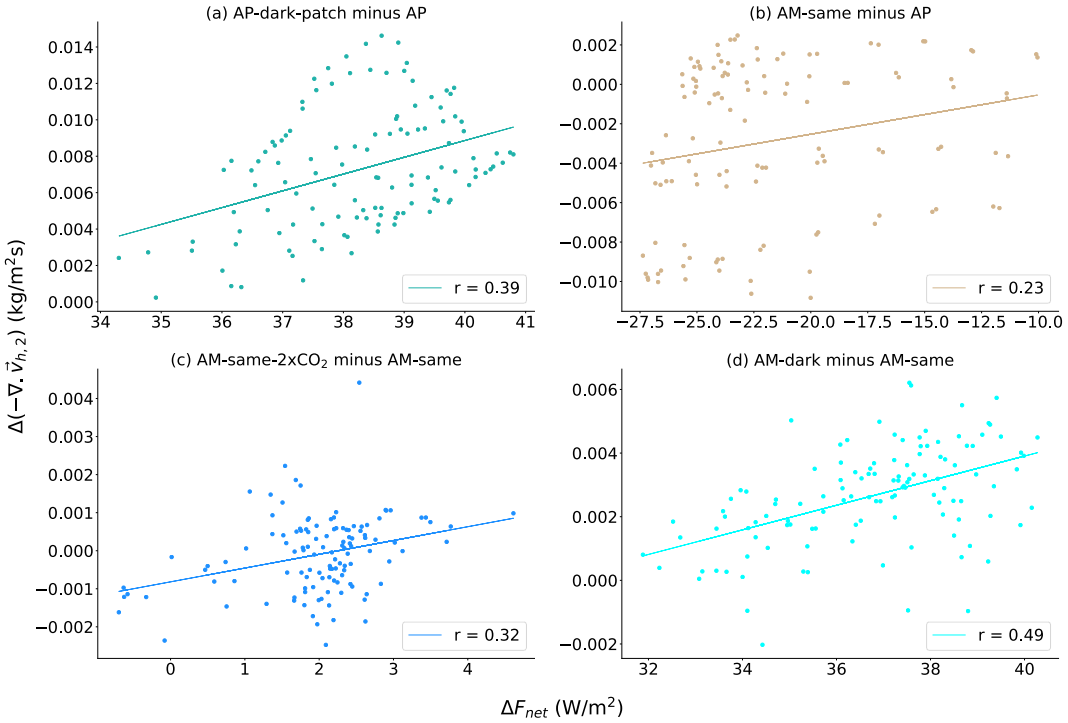

Figure 6.11: As in 6.10, but this time for ΔF_{net} (x-axis) and changes in $-\nabla.\mathbf{v}_{h,2}$ (y-axis). p-values are less than 0.01 (greatest value in panel b).

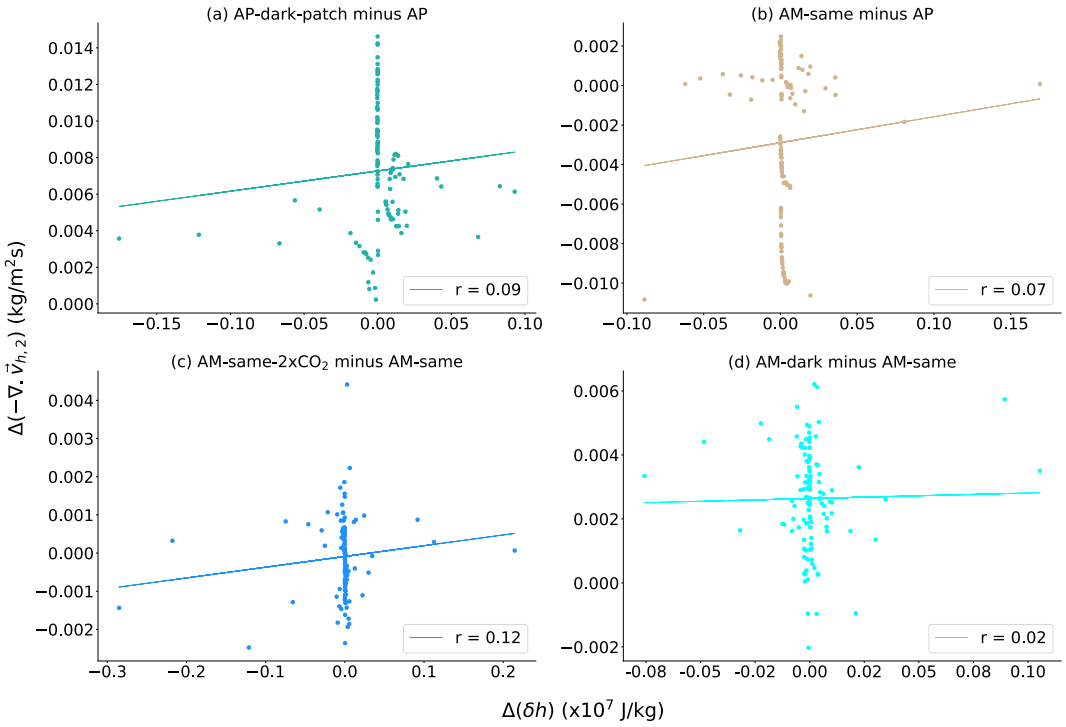

Figure 6.12: As in 6.10, but this time for changes in δh (x-axis) and changes in $-\nabla.\mathbf{v}_{h,2}$ (y-axis). An outlier has been removed in (a) and (b). p-values are a) 0.33, b) 0.43, c) 0.18 and d) 0.84.

We have been careful to distinguish between the terms 'heating' and 'warming' in this chapter. While a surface warming (increase in temperatures) has been imposed in all four simulations, we can not speak of a surface heating (increase in atmospheric energy) in the experiment where the continent replaces a patch of ocean, because the net energy input to the atmosphere (F_{net}) decreases in this case (Fig. 6.9). The results discussed in this section demonstrate that the increase in temperatures in all four warming experiments – which might be expected to lead to an increase in rainfall – are not a good metric for precipitation changes when the warming is caused by a decrease in evaporation, and the moist static energy budget of the atmosphere should be considered instead (Maroon et al., 2016).

6.5 Impact of seasons on continental rainfall

In this section, the impact of the seasonal migration of the Sun on continental and maritime precipitation is investigated. In the experiment studied here, the

only difference between land and ocean is the fact that evaporation over land is restricted by soil moisture availability through the bucket model (as in AM-same). The heat capacities of land and ocean are both equivalent to that of a 20m deep mixed-layer ocean.

In the annual mean, continental *P* in 'seasons-AM-same' is much greater than in the same set-up without seasons (Fig. 6.13). This is due to the fact that this simulation exhibits a monsoon-type *P* behaviour, with seasonally varying rainfall (Fig. 6.14) and a change (albeit not reversal) of near-surface wind direction from North-Easterly in MAM to South-Easterly in SON (Fig. 6.15). During MAM/SON, local rainfall is very high on the East Coast of the continent, but weak towards the west. During JJA/DJF, a weaker rain band traverses the entire continent. In the absence of seasons, the atmospheric circulation remains in this state of weak precipitation year-round, leading to lower annual means because the seasons of intense rainfall are absent.

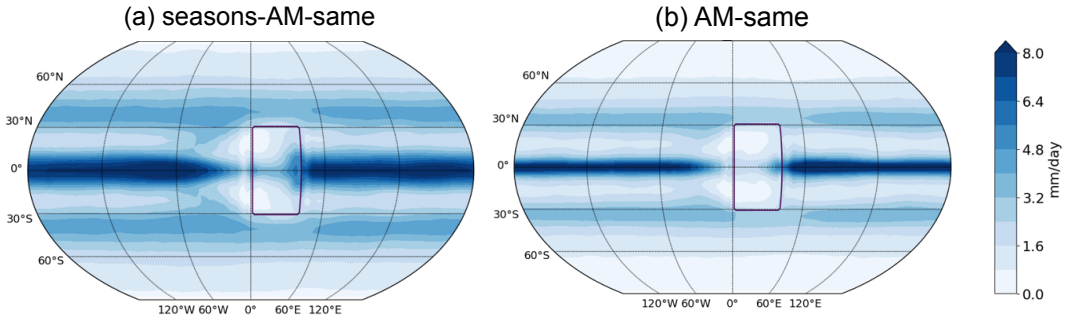

Figure 6.13: Annual mean for AM-same a) with and b) without seasons.

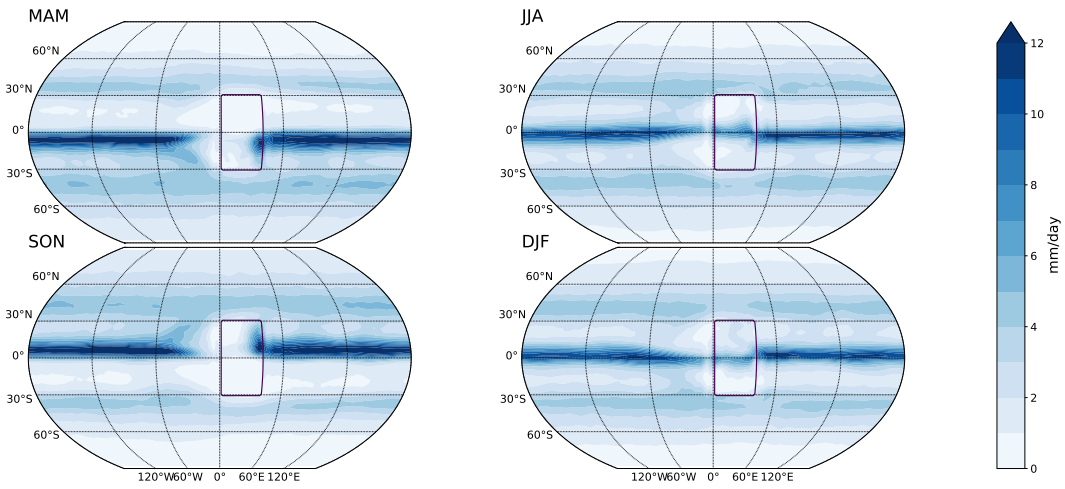

Figure 6.14: Seasonal-mean precipitation for seasons-AM-same.

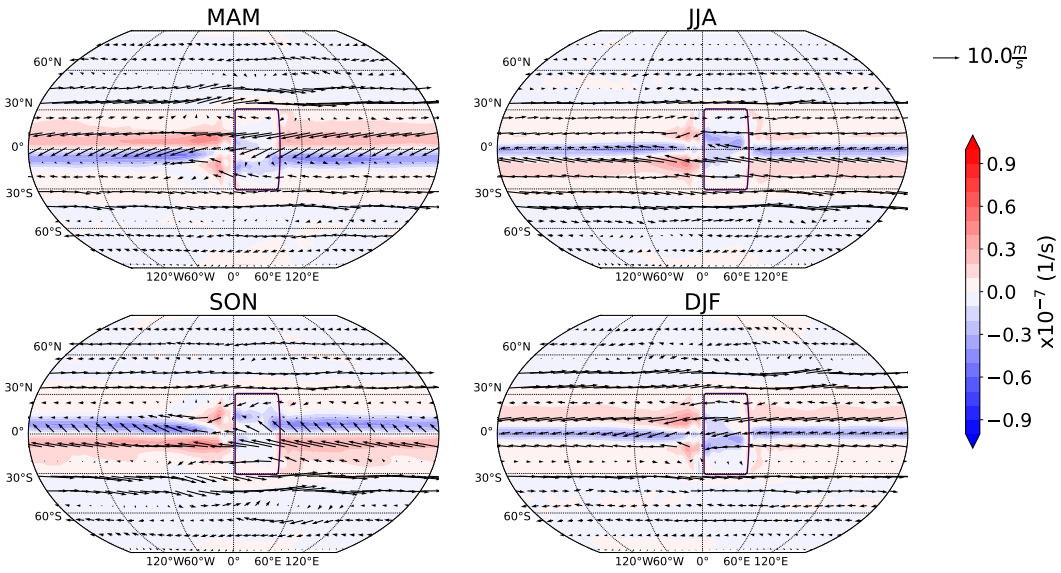

Figure 6.15: Seasonal-mean winds (arrows) and moisture flux divergences (red is divergence, blue is convergence, in 10^{-7} 1/s) at 870 hPa for seasons-AM-same.

In order to understand why *P* is strong on the East Coast during MAM/SON and weak along the Equator during JJA/DJF, the atmospheric circulation, near-surface winds and moisture fluxes are studied. Two weak Hadley cells straddle the Equator during JJA/DJF (Fig. 6.16) and hence near-surface winds are predominantly easterly in the tropics in those seasons (Fig. 6.15). Horizontal winds and moisture fluxes converge along the Equator across the width of the whole continent, leading to weak precipitation in the region. In the absence of seasons, this 'equinoctial' circulation regime persists year round.

During MAM/SON, a strong cross-equatorial Hadley cell develops and thus the ITCZ moves off the Equator (Fig. 6.16). The resultant near-surface winds have a clear northerly/southerly component in contrast to JJA/DJF (Fig. 6.15), similar to the South America monsoon where 850hPa winds turn from being predominantly easterly to having a cross-Equatorial component in the wet season (Marengo et al., 2012; Geen et al., 2020). The fact that the winds are northeasterly/southeasterly during MAM/SON results in near-surface wind and moisture flux convergence and strong *P* on the East Coast of the continent. The western part of the continent receives less rainfall compared to the East in this 'solsticial' regime. The air advected into the western region is relatively dry since it crosses half the continent in meridional and longitudinal direction (Chou et al., 2001).

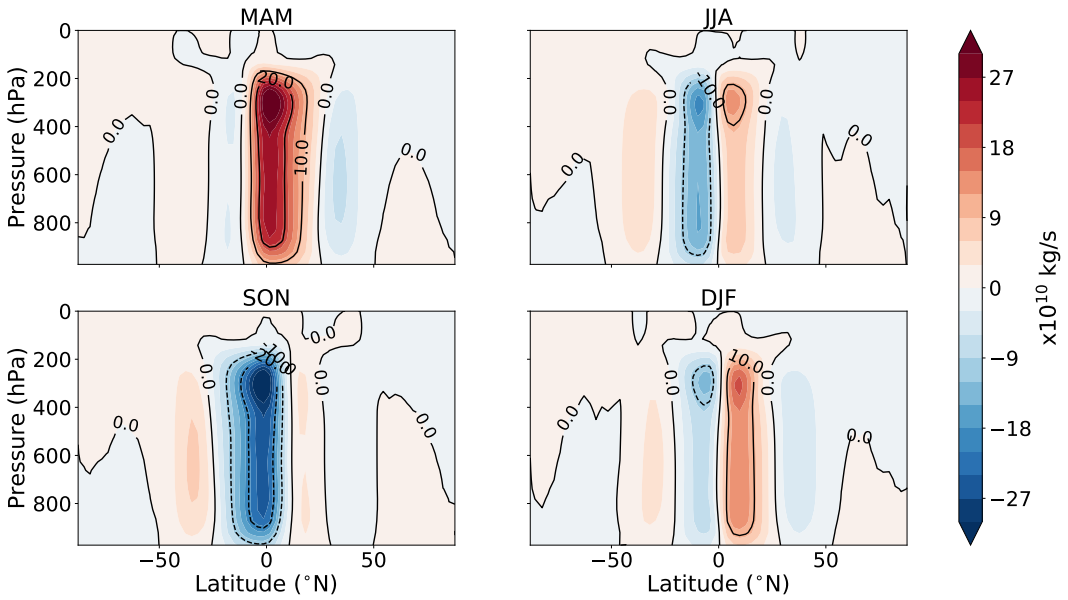

Figure 6.16: Seasonal-mean mass streamfunction for seasons-AM-same (colours and contours) in 10^{10} kg/s. Clockwise circulation is shown in red (solid contours), counter-clockwise in blue (dashed contours).

Compared to the Earth's Hadley circulation, the seasonal cycle in our simulation is lagged by about 3 months, with the equinoctial regime occuring in JJA/DJF instead of MAM/SON, and the solsticial regime occuring in MAM/SON instead of JJA/DJF (see Section 2.7). This is due to the high thermal inertia of the land and ocean in our simulation. Generally, the higher the thermal inertia of the surface, the slower the system is in responding to seasonal solar forcing, as shown in recent work on aquaplanets with different mixed-layer depths (Geen et al., 2018; Donohoe et al., 2013; Bordoni and Schneider, 2008). Our results are realistic over the ocean, since the Earth's ITCZ in the Pacific and Atlantic Ocean lag the migration of the Sun by about 3 months (Battisti et al., 2018). The lag in the overturning circulation is thus likely caused by the large thermal inertia over land, the fact that there is only one continent and potentially by the inability of the ocean to transport heat laterally (Geen et al., 2018). While the lag in the seasonal cycle of the Hadley circulation in our simulations is noteworthy, it does not affect the interpretation of our results since our simulation is inherently unrealistic.

The maximum latitude of the tropical rain band is greater over land than over ocean in this simulation (Figs. 6.14 and 6.17), consistent with e.g. Chou et al. (2001). This is somewhat similar to aquaplanets, where the ITCZ migrates fur-

ther poleward over a shallow ocean compared to a deep one, due to the greater MSE gradient between the hemispheres (Bordoni and Schneider, 2008; Wei and Bordoni, 2018; Donohoe et al., 2013). Despite the fact that there is no difference in thermal inertia between land and ocean in our simulations, a contrast in the poleward extent of the ITCZ over the two domains is achieved. This is solely due to the evaporative resistance over land (due to the bucket hydrology).

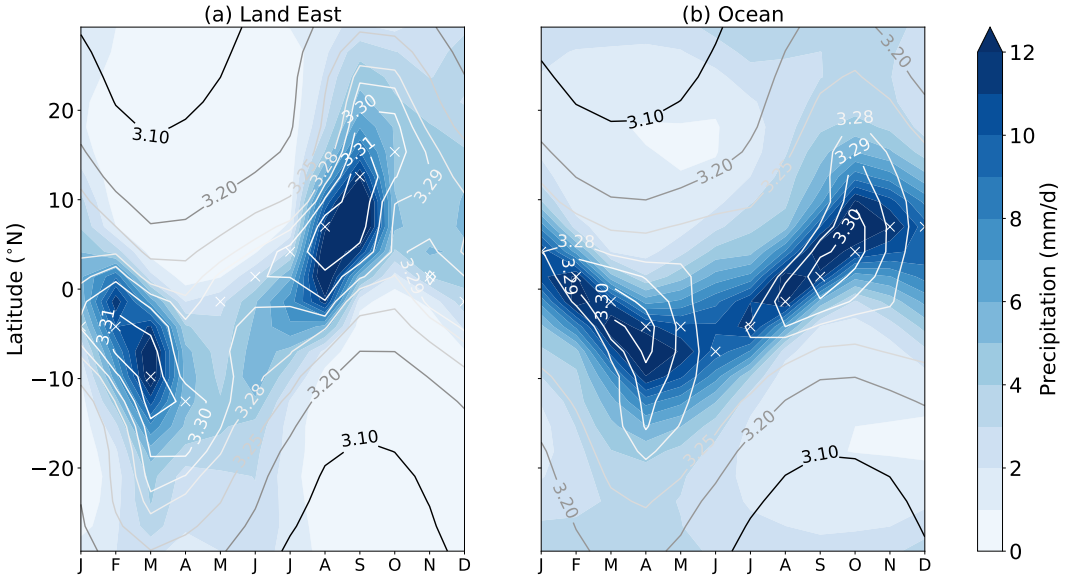

Figure 6.17: Seasonal cycle of zonal mean P (colours) over a) the eastern part of the continent (Land East = 20°-40°E) and b) over the ocean. White crosses indicate the latitude of the MSE_b maximum in each month. MSE_b is calculated at 870 hPa (following Bordoni and Schneider, 2008). Contours show the zonal mean MSE_b in units of 10^5 J/kg.

Following Privé and Plumb (2007) we study the seasonal migration of rainfall over land and ocean in relation to the sub-cloud or near-surface MSE (MSE_b, Fig. 6.17). This analysis shines a light on the energetic constraint on the poleward migration of the ITCZ over ocean compared to land. In our simulation, the maximum of MSE_b migrates further poleward over land compared to ocean. According to Privé and Plumb (2007), the precipitation maximum is located near or equatorward of the MSE_b maximum. Figure 6.17 shows that this is the case in our simulation over land, whereas over ocean, the P maximum tends to be slightly poleward of the MSE_b maximum. Privé and Plumb (2007) noted a similar behaviour in some aquaplanet simulations, but the different relationship between MSE_b and P over land compared to ocean merits further investigation. Nonetheless, the difference between the maximum latitude of MSE_b over land compared

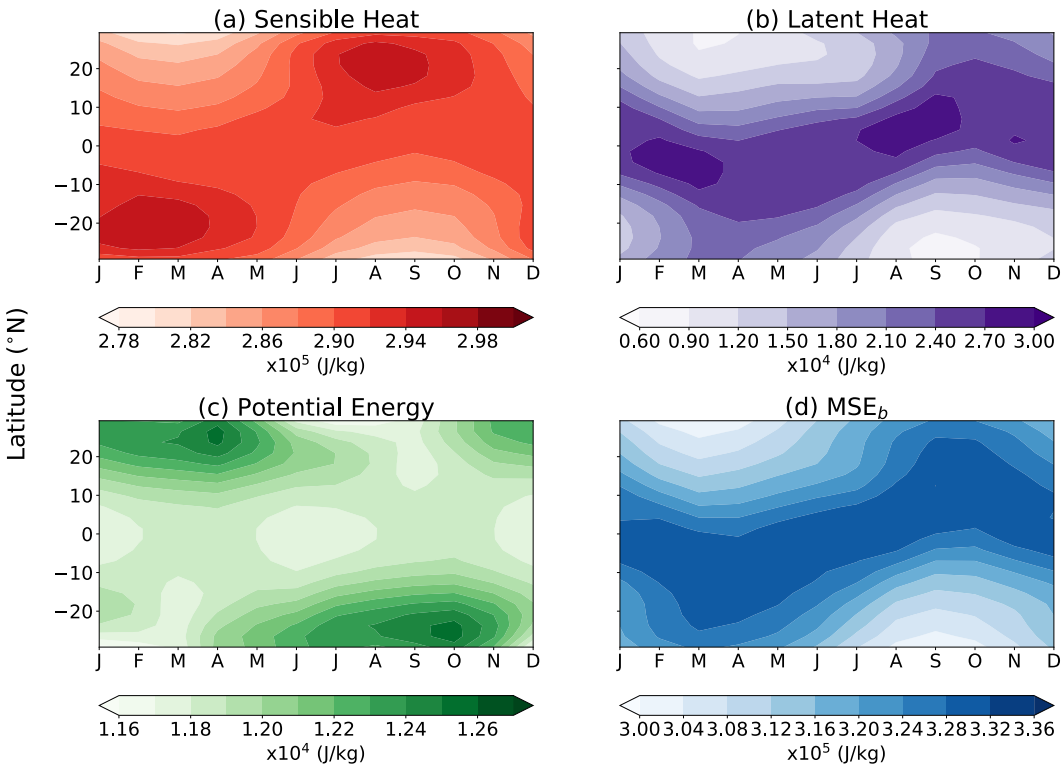

Figure 6.18: Seasonal cycle of zonal mean contributions from a) sensible heat ($c_p \cdot T$), b) latent heat ($L \cdot q$) and c) potential energy ($g \cdot z$) to MSE$_b$ (d) in J/kg, averaged over Land East (20° - 40°E) at 870 hPa as in Fig. 6.17. The latent heat and potential energy terms are an order of magnitude smaller than the sensible heat and total MSE$_b$.

to ocean might give an indication as to why the rain band migrates further poleward over the continent.

In the following, the differences in MSE$_b$ over land compared to ocean are further examined. In addition to the MSE$_b$ maximum migrating further poleward over land than over ocean, the peak value of MSE$_b$ is also higher over land. As demonstrated by Figure 6.18, MSE$_b$ over land is dominated by the sensible heat term (panel a), whereas latent heat (panel b) and potential energy (panel c) together contribute only roughly 10% of the total MSE$_b$ (panel d). The contribution of the individual terms to MSE$_b$ is similar over ocean (Fig. 6.19), with sensible heat being the dominant term.

The sensible heat release is larger over land than over ocean, and the maximum migrates further poleward due to the limited availability of soil moisture. The soil dries out seasonally poleward of about 10° (Fig. 6.20). In the Equatorial region, soil moisture is replenished by rainfall year-round. North of 10°N, soil

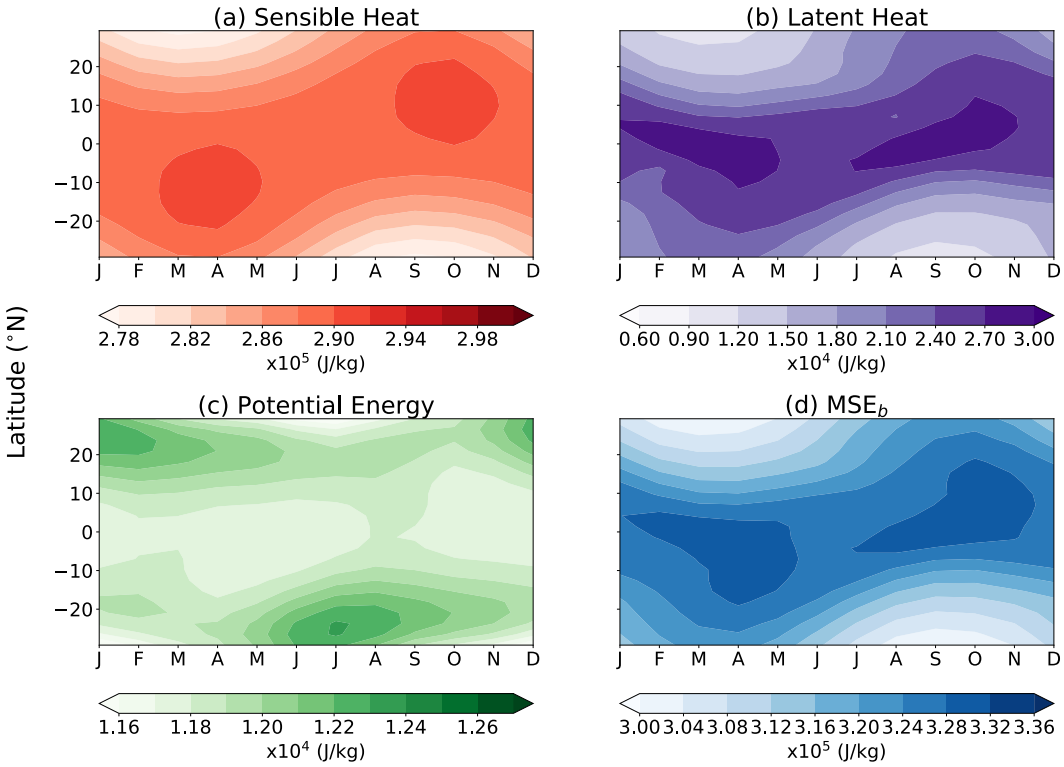

Figure 6.19: Same as Fig. 6.18 but this time over ocean.

moisture is limited between March and August. The energy input from the Sun during Northern Hemisphere summer (JJA) thus leads to high surface temperatures and sensible heat release. As the rain band migrates north, soil moisture is replenished and latent heat release increases while the sensible heat flux decreases. The further poleward migration of the ITCZ over land compared to ocean – despite the same thermal inertias – is thus connected to seasonally limited soil moisture over land, and a consequent larger and further poleward sensible heat and MSE$_b$ maximum.

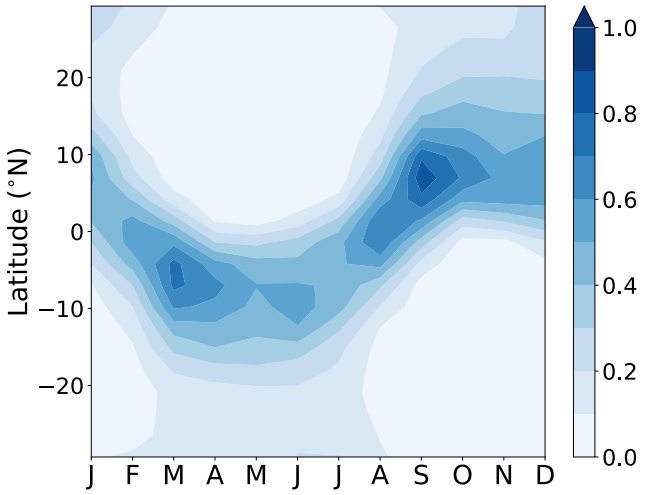

Figure 6.20: Seasonal cycle of zonal mean soil moisture (W) averaged over Land East (20° - 40°E) divided by the field capacity (W_f·0.75). This ratio determines the evaporative conductance C_L (see Section 3.2), with values ≥1 corresponding to uninhibited evaporation as over the ocean, and a value of 0 corresponding to no evaporation.

6.6 The teleconnection between Africa and South America in continental drift experiments

The impact of idealised Africa on ΔP over idealised South America is related to a warming-induced Matsuno-Gill type circulation anomaly over Africa (see Chapter 4). According to Cook et al. (2004) the teleconnection between the two continents is facilitated by the relatively small distance between them. We investigate the impact of Africa on South America in a series of 'continental drift' experiments using the same set-up as in Chapter 4 with prescribed SSTs. The two continents are located 10°, 40°, 70° and 100° longitude apart (Fig. 6.21).

When the two continents are closest to each other, both idealised Africa and America receive very little rainfall in the unperturbed climate (P_{ctl}, see contours in Fig. 6.21). P_{ctl} in 2C 10° is similar to the rainfall distribution when the two continents are combined to form one supercontinent spanning 100° longitude (resembling Pangaea, see Fig. 6.22). As shown in Chapter 5, the wider the continent is, the less rainfall it receives.

When the continents are sufficiently far apart, idealised America receives ample rainfall in the control climate, whereas idealised Africa still receives relatively little. The fact that P_{ctl} over idealised Africa is insensitive to the relative location

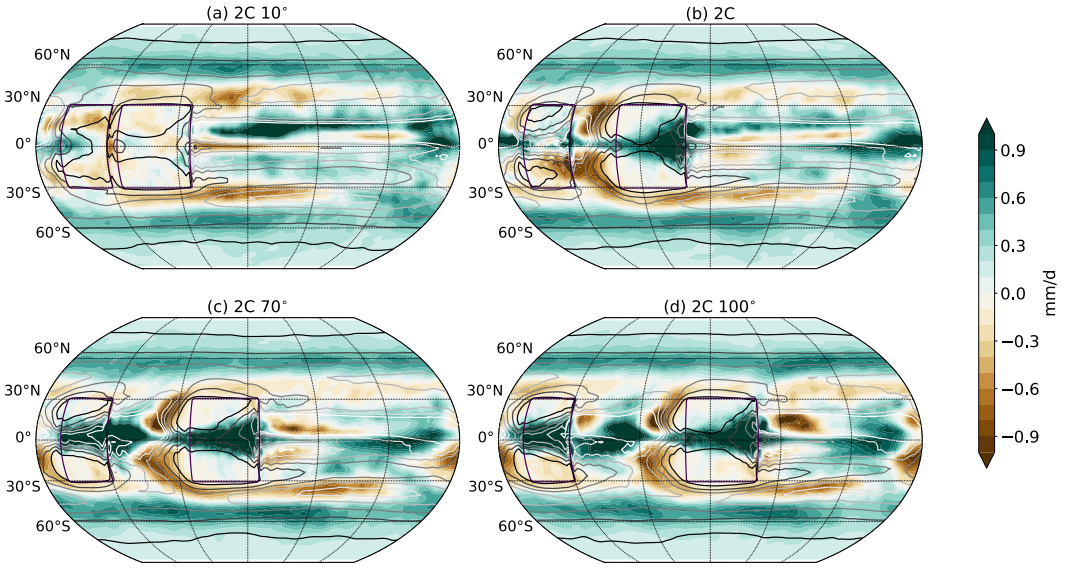

Figure 6.21: ΔP (colours) for a doubling of CO_2 for idealised America and Africa at a) 10°, b) 40°, c) 70° and d) 100° longitude apart. Contours show P_{ctl} of 1 mm/day (black) to 6 mm/day (white) with 1 mm/day spacing.

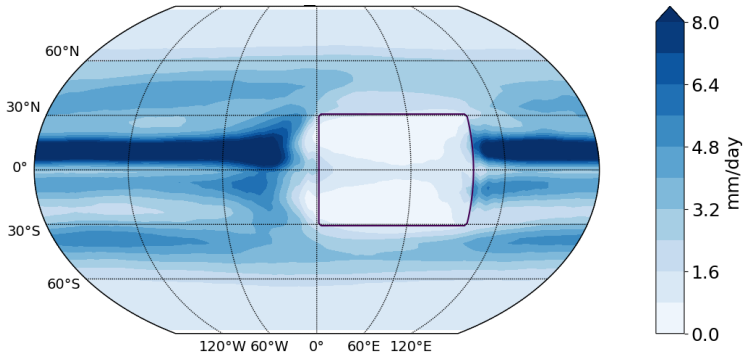

Figure 6.22: P_{ctl} for a supercontinent spanning 100° longitude (i.e. the width of idealised Africa and America combined) with the same set-up as the other experiments in this section.

of the two continents is consistent with a smaller impact of the western continent on the eastern continent as discussed in Chapter 4 and by Cook et al. (2004).

In the experiment with idealised Africa on its own in Chapter 4 (AF, Fig. 4.4b and 4.5b) there are 'peak' regions of warming-induced anomalous ascent (stronger rainfall) and 'trough' regions of anomalous subsidence (weaker rainfall) over the ocean to the west of idealised Africa. If idealised America is located in one of the peaks, rainfall over this continent can be expected to be enhanced compared to the simulation where America is on its own (AM, Fig. 4.4a).

This is in fact what we observe when America is 70° or 100° longitude to the west of idealised Africa (Figs. 6.21c, d and 6.23c, d). When idealised America is located 10° or 40° longitude away from idealised Africa, it is in a region of anomalous subsidence and hence receives less rainfall than in AM (Figs. 6.21a, b and 6.23a, b). In fact, the drying impact of idealised Africa on idealised America to the South of the Equator (the 'idealised Amazon basin') is largest in our original set-up where the two are 40° longitude apart, approximately like they are on Earth.

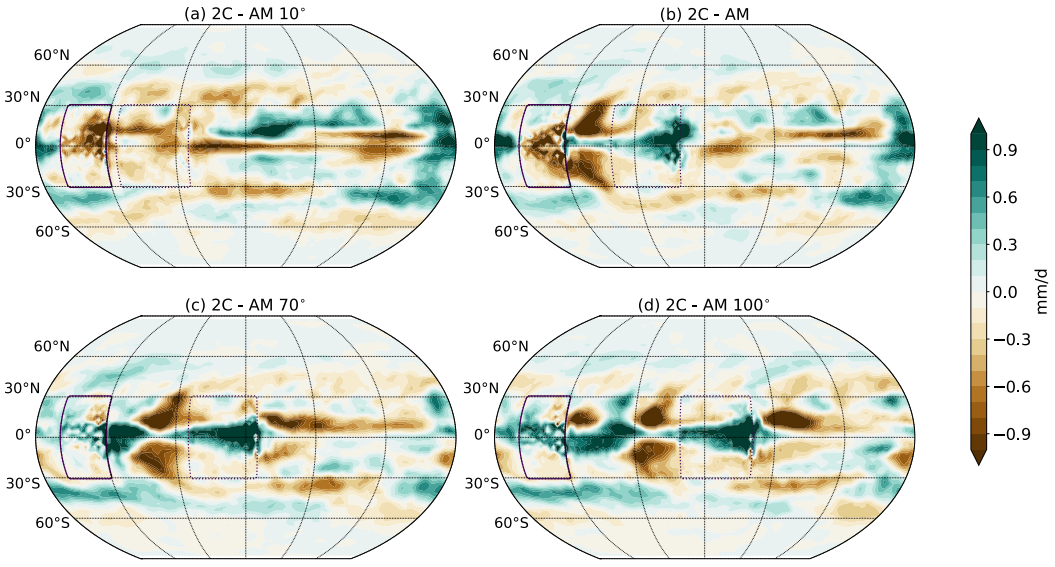

Figure 6.23: Difference in ΔP due to a doubling of CO_2 between the experiments with two continents at different distances (as in Fig. 6.21) and the set-up with only idealised America. This difference shows the impact of idealised Africa on ΔP over idealised America, as in Chapter 4.

6.7 Conclusions

In this chapter, the fundamental processes that control rainfall over land compared to ocean were studied using the idealised Atmospheric General Circulation Modeling framework 'Isca' (Vallis et al., 2018 and Section 3). Based on the Matsuno-Gill theory (Gill, 1980) and our results from Chapter 4, a source of Equatorial surface heating – such as a tropical continent or warm ocean surface temperature anomaly – would be expected to lead to anomalous ascent and stronger rainfall over the heat source. This turned out to be true in three different surface warming experiments, where the surface heating was due to a darkening of a patch of ocean, a doubling of CO_2 over land and ocean and when the albedo of a land surface was reduced. However, when a patch of ocean was replaced by a land surface, anomalous subsidence occurred over the continent and rainfall was suppressed. Since lower-level temperatures over the source of surface warming increased most in this case, temperature changes alone are not a good indicator of rainfall changes (Maroon et al., 2016).

A more useful approach was to consider changes in precipitation in terms of changes in the column-integrated MSE flux divergence (ΔF_{MSE}), following the influential work of Neelin and Held (1987). An increase/decrease in F_{MSE} was associated with an increase/decrease in precipitation on a regional scale and in the zonal mean in our simulations. Precipitation changes can be related directly to changes of F_{MSE} – and equivalently to changes in the net energy input to the atmospheric column (ΔF_{net}) – if changes in the gross moist stability can be neglected. While we provided evidence that ΔP is in fact more closely related to ΔF_{MSE} than to changes in the gross moist stability in our simulations, further investigation into the assumption of constant δh in idealised simulations like ours is called for.

At present, there is no clear theory that states under which circumstances δh can be assumed to remain constant following a certain type of climate perturbation (see Section 2.8). While several studies have successfully related changes in tropical rainfall to changes in the atmospheric energy budget (Kang et al., 2008; Donohoe et al., 2013; Frierson and Hwang, 2012) – implying that $\delta h = const.$ is a valid assumption in those cases (Seo et al., 2017) – more recent studies of aquaplanets have shown that the gross moist stability can not generally be

assumed to be constant (Wei and Bordoni, 2018; Seo et al., 2017).

In all of the above experiments, an annual-mean insolation profile was used and hence there was no seasonal variability. Introducing the seasonal migration of the Sun in a set-up with one idealised continent led to a monsoon-type rainfall behaviour over land, with strong seasonal rainfall on the East Coast of the idealised continent. The only difference between land and ocean in this simulation was the surface hydrology, while the thermal inertias over land and ocean were the same. The limited evaporation over land was enough to lead to a further poleward migration of the ITCZ compared to the ocean. According to Privé and Plumb (2007), the precipitation maximum is expected to be co-located or equatorward of the near-surface moist static energy (MSE_b) maximum. The MSE_b maximum migrated further poleward over land compared to ocean in our simulation, which might explain the ITCZ behaviour. We found that the sensible heat term dominated the MSE_b both over land and ocean. The maximum of sensible heat was greater over land and migrated further poleward than over ocean, due to seasonally limited soil moisture for evaporation over land poleward of about 10°. One caveat of this conclusion is that while over land the precipitation maximum was near or equatorward of the MSE_b maximum, the opposite was true over oceans. Privé and Plumb (2007) also observed this behavior in some aquaplanet simulations, but further investigation into the relationship between rainfall and MSE_b over ocean is called for.

In a final set of experiments, the configuration from Chapter 4 and Pietschnig et al. (2019) with two idealised continents representing South America and Africa was revisited. As discussed in Chapter 4, the warming-induced Matsuno-Gill type circulation anomaly over Africa leads to subsidence and hence drying to its west. When America was placed 70° or 100° to the west of Africa into a region where the African circulation anomaly led to ascent, rainfall over America also increased. When the idealised American continent was moved closer to idealised Africa into a region of anomalous subsidence, rainfall over idealised America decreased with warming. Notably, the drying impact of idealised Africa on idealised South America turned out to be largest when the two continents were located 40° longitude apart, as in Chapter 4 and on Earth.

Chapter 7

Conclusions and Future Work

In this thesis, the following three main questions were addressed (see Section 1.1):

1. Why is the Amazon basin projected to dry out whereas Equatorial Africa is likely to receive more rainfall in the future, even though both regions see a positive $P - E$ in the unperturbed climate?

2. Why do plant physiological changes lead to an amplification of precipitation change, i.e. more drying over the Amazon basin and more wetting over the Maritime Continent compared to climate models without a representation of vegetation?

3. What are the mechanisms controlling tropical rainfall and warming-induced changes thereof over land versus ocean?

In this chapter, the motivation and research question for each chapter are briefly repeated, followed by a summary of the most important findings and discussion of their relevance in a broader context. While the results from this thesis provide answers to the three questions stated above, they also raised further questions which are discussed in Section 7.1.

Global warming is projected to enhance precipitation by about 1 - 3% per Kelvin in the global mean, with increases near the Equator, decreases in the subtropics and increases in the mid- to high-latitudes (Allen and Ingram, 2002; Held and Soden, 2006; Collins et al., 2013). These precipitation changes roughly follow the 'wet-get-wetter' principle, which states that regions where pre-industrial precipitation exceeds evaporation ($P - E > 0$) will see an increase in precipitation

with warming whereas regions in which $P - E < 0$ will see a decrease (Held and Soden, 2006). While capturing zonal-mean and maritime precipitation change (ΔP) well, this approximation is less appropriate over land (Chadwick et al., 2013; Byrne and O'Gorman, 2015). Particularly over the Amazon basin, warming leads to precipitation decreases ('drying'). At the same latitude, a P increase ('wetting') is projected over Equatorial Africa and the Maritime Continent. All three regions see a strongly positive $P-E$ in the pre-industrial climate. This zonally asymmetric P response to warming was the main motivation for Chapter 4.

Using Isca, the University of Exeter's framework for designing atmospheric General Circulation Models (AGCMs, Vallis et al., 2018), the first question *"Why is the Amazon basin projected to dry out whereas Equatorial Africa is likely to receive more rainfall in the future, even though both regions see a positive $P - E$ in the unperturbed climate?"* was addressed in Chapter 4. The first of two important findings in this chapter was that soil moisture limitations on land-surface evaporation contribute to the zonally asymmetric ΔP patterns over the Amazon basin and Equatorial Africa under a doubling of CO_2. The soil moisture constraint on evaporation over land is parameterised in Isca using the 'bucket model' (Manabe, 1969), which was used in the first generation of Earth System Models (ESMs, Bonan, 2008). In contrast, when land evaporation was only reduced by a constant percentage compared to evaporation over ocean, ΔP was zonally uniform and exhibited a 'wet-get-wetter' response over ocean and land. Hence, the land surface cannot simply be seen as a passive component of the climate system, since changes in the evaporative flux clearly modify rainfall patterns (Shukla and Mintz, 1982).

The second important finding from Chapter 4 was that drying over the Amazon basin is caused by circulation changes over Africa. This was shown in simulations with two rectangular continents resembling tropical Africa and America in their longitudinal extent and distance to each other, each spanning the entire tropical band from 30°South to 30°North. Due to the CO_2 forcing, ascent and precipitation increased over idealised Equatorial Africa (10°S - 10°N). In accordance with the Matsuno-Gill theory (Gill, 1980), this ascent led to subsidence and associated reductions in relative humidity and precipitation over the Atlantic Ocean and over idealised America south of the Equator (the 'idealised Amazon basin'). In the absence of the African continent, idealised America saw a widespread increase

in rainfall. Hence, precipitation changes over South America are not independent of rainfall changes over Equatorial Africa.

In Chapter 4, two mechanisms were therefore identified which contribute to the zonally-asymmetric rainfall responses over Africa and South America due to CO_2 forcing: Limited soil moisture and an atmospheric teleconnection. The results from Chapter 4 were published in *Geophysical Research Letters* (Pietschnig et al., 2019).

Precipitation changes over tropical land regions are amplified by the response of vegetation to CO_2 forcing in Earth System Models (ESMs). Plant physiological changes lead to stronger drying of the Amazon basin and stronger wetting over the Maritime Continent (Swann et al., 2016; Skinner et al., 2017; Chadwick et al., 2017; Kooperman et al., 2018). Plants respond to a CO_2 forcing by reducing the conductance of the stomata on their leaves – the pathway for exchange of moisture and CO_2 with the atmosphere – potentially reducing evapotranspiration (Sellers et al., 1996; Swann, 2018). However, leaf area also increases due to CO_2 fertilisation which might lead to more evapotranspiration, although changes in leaf area are highly uncertain (Swann, 2018; Mahowald et al., 2016). In Earth System Models, the vegetation response to CO_2 forcing tends to be dominated by changes in stomatal conductance, rather than leaf area (Swann et al., 2016; Swann, 2018; Skinner et al., 2017). The amplification of ΔP due to vegetation changes were the main motivation for Chapter 5.

The second question *"Why do plant physiological changes lead to an amplification of precipitation change, i.e. more drying over the Amazon basin and more wetting over the Maritime Continent compared to climate models without a representation of vegetation?"* was addressed in Chapter 5. The first of three important findings in this chapter was that in an Isca simulation with realistic continents and topography, the parameterisation of reduced stomatal conductance with a doubling of CO_2 did in fact lead to the expected amplification of ΔP compared to the simple bucket formulation from Chapter 4, despite the simplicity of our vegetation model. This finding reinforces our statement from above, that the land surface (this time including vegetation) interacts with the atmosphere and thus modifies the climate response to CO_2 forcing (Shukla and Mintz, 1982; Bonan, 2008). While other effects of changes in the vegetation cover (such as albedo and carbon flux changes, Charney, 1975, Bonan, 2008) have been ne-

glected here, the finding that a decrease in stomatal conductance already leads to a much stronger drying of the Amazon basin implies that deforestation – which corresponds to a strong decrease in stomatal conductance in terms of evapotranspiration – could lead to a rainfall decrease in the region (Spracklen et al., 2018, 2012; Wright et al., 2017).

The second important result from Chapter 5 was based on a simulation with an idealised, rectangular continent spanning 30°S to 30°N with an extent of 3° longitude, approximately the width of Sulawesi in the Maritime Continent. For this narrow island, P increased with increasing CO_2 with the wetting around the Equator being stronger when land-surface evaporation completely ceased with warming than when stomata remained open. Surface temperatures increased more when land-surface evaporation was zero, leading to an enhancement of convection over the continent. This drew in moisture from the surrounding ocean, resulting in heavy rainfall in the Equatorial region. Hence, despite the fact that no moisture was provided to the atmosphere locally through evaporation, precipitation was able to increase due to moisture advection from the surrounding ocean. Our results confirm recent studies which explained the enhanced P increase over the Maritime Continent due plant physiological responses through a similar mechanism (Saint-Lu et al., 2019; Chadwick et al., 2019; Kooperman et al., 2018).

The third major finding from Chapter 5 was that the enhancement of the drying over the idealised Amazon basin due to vegetation changes was caused by local changes in E and $P - E$. Precipitation and the circulation over Equatorial Africa were insensitive to the decrease in stomatal conductance, and hence the remote drying influence on the idealised Amazon basin (see Chapter 4) remained the same with or without changes in stomatal conductance. Over idealised America, P increased strongly along the Equator and to the north when stomatal conductance was reduced by 50% with warming, and decreased in the idealised Amazon basin even in the absence of idealised Africa. Essentially due to high pre-industrial rainfall rates, evaporation along the Equator became 'energy limited' in the perturbed climate according to the Budyko framework, and hence did not increase in-step with P. The moisture for the enhancement of P along the Equator and to the north was provided by moisture advection from other land regions such as the idealised Amazon basin, thus reducing precipitation there. A similar mechanism appeared to contribute to the drying of the Amazon basin in

the simulation with realistic continents.

In summary, in Chapter 5 we found that a simple representation of changes in stomatal conductance produced an amplification of ΔP as expected from ESMs, suggesting that this mechanism might play a dominant role in ESM projections (Skinner et al., 2017; Swann et al., 2016; Swann, 2018). Two important mechanisms were identified which contribute to the amplification of ΔP. Over a small island (such as Sulawesi in the Maritime Continent), enhanced moisture advection from the surrounding ocean overcompensates for the loss of moisture due to ceased evaporation. The amplified drying in parts of the Amazon basin might be connected to stronger P than E increases near the Equator. Moisture for precipitation near the Equator must be provided from nearby land regions, which dry out as a result. The results from Chapter 5 are currently being drafted as a manuscript in collaboration with Prof. Abigail Swann, and will be submitted for review soon.

The Matsuno-Gill theory of the tropical circulation (Gill, 1980) states that imposing a surface heating at the Equator – be it a warm sea surface temperature anomaly or heating of a land mass – leads to enhanced ascent over the heat source. This theory was applied in Chapter 4, as discussed above. However, this triggered further questions regarding the type of surface warming. Does an increase in surface temperatures over a land surface lead to the same circulation response as heating of an ocean surface, and what happens when a land surface replaces an ocean surface?

Monsoon-type behavior has been identified in aquaplanet simulations with sufficiently shallow oceans so that a strong moist static energy gradient between the summer and winter hemispheres can be established. This allows the intertropical convergence zone (ITCZ) to rapidly move off the Equator into the summer hemisphere (Geen et al., 2020; Bordoni and Schneider, 2008; Wei and Bordoni, 2018; Geen et al., 2018). Since there are no land masses in an aquaplanet, the theory of monsoons is moving away from the historical "large-scale land-sea breeze" towards a regional manifestation of the seasonally migrating ITCZ.

In Chapter 6, we sought to address the third question *"What are the mechanisms controlling tropical rainfall and warming-induced changes thereof over land versus ocean?"*, again designing idealised simulations in Isca. Four different types of surface warming were investigated: Reducing the albedo of a

patch of ocean, replacing a patch of ocean by an idealised continent, imposing a doubling of CO_2 in a simulation with the idealised continent, and decreasing the albedo of the idealised continent. In all but one case, the surface warming led to enhanced ascent and rainfall over the surface temperature anomaly. However, when ocean was replaced by land, the strong decrease in atmospheric water vapour over the continent led to subsidence despite the strong temperature increase. Hence, our results confirm that temperatures alone are not a good indicator of rainfall changes (Maroon et al., 2016). The moist-static energy budget of the atmosphere provided a more useful framework for understanding rainfall changes in the four surface warming scenarios described above. Relating local rainfall changes to changes in the net energy input to the atmospheric column (F_{net}) following Neelin and Held (1987), we found that P decreased in the case where ocean was replaced by land because F_{net} decreased, making rainfall over the continent energetically less favourable.

In the simulations described above, the solar insolation was held fixed at annual-mean values. In another simulation, the seasonal migration of the Sun and consequent migration of the ITCZ was investigated over land and ocean. Rainfall over land exhibited a monsoon-type behaviour with very strong rainfall on the East Coast to the North of the Equator in one and to the South in the other season, and weak rainfall along the Equator in the remaining two seasons. Similar to the South America monsoon, the near-surface winds turned from mostly easterly to having a cross-Equatorial component during the wet season (Marengo et al., 2012; Geen et al., 2020).

The ITCZ migrated further poleward over land than over ocean in our simulation. This finding was somewhat surprising, since the thermal inertia of land and ocean were the same in our simulation. The only difference between the two domains – the higher evaporative resistance over land – was sufficient to produce a higher and more poleward near-surface moist static energy (MSE) maximum over land compared to ocean, essentially due to high seasonal sensible heating poleward of 10°. According to Privé and Plumb (2007), the near-surface MSE maximum roughly marks the poleward limit of the P maximum.

The main findings from Chapter 6 concerning the controls on rainfall and precipitation change over land compared to ocean were: P increases when a patch of ocean or land is warmed – as expected from the Matsuno-Gill theory – but the

theory does not apply when changes in humidity are large. The atmospheric energy budget provides a more useful framework for understanding ΔP. Monsoon-type behaviour was observed in a simulation where the thermal inertia of land and ocean were the same, but evaporation over land was constrained.

7.1 Suggestions for future work

In Chapter 4, it was shown that circulation changes over idealised Equatorial Africa led to a decrease in rainfall over the idealised Amazon basin. In this teleconnection, South America was essentially passive. However, when soil moisture feedbacks were neglected, the P response to warming was zonally uniform and P increased over the Amazon basin. In this case, the drying influence of idealised Equatorial Africa on South America vanished, despite the fact that P increased strongly over idealised Equatorial Africa. This was partly due to the fact that the teleconnection was weaker, which in itself is an interesting finding that merits further analysis. In addition, local effects might have contributed to the drying in the case with soil moisture feedbacks, analogous to our findings from Chapter 5 where we showed that local changes over South America amplify the remotely-forced drying when stomatal conductance is reduced.

In order to further investigate the local and remote influences on drying over South America in the simulation with soil moisture feedbacks (bucket model), a spatially varying land-surface hydrology could be used with the bucket model over Africa and a constant soil moisture conductance over America. If the idealised Amazon basin still dries strongly in this case, then it would appear to be essentially 'passive' in the original bucket model experiment, and local effects only become important when evaporation is also constrained by stomatal conductance. In contrast, if the Amazon basin gets wetter in this case, then local evaporative feedbacks are needed in order to produce the overall drying.

Based on our simulations with the two idealised continents, and the fact that ΔP in this simplified continental configuration captured ΔP patterns from complex GCMs, we inferred that similar circulation changes might occur over Africa, leading to a drying of the Amazon basin in those models. This hypothesis should be tested in more realistic simulations in Isca or in a complex GCM with only Africa,

only South America and the two continents combined.

The length-scale of the Matsuno-Gill type teleconnection between Africa and America was investigated in a series of 'continental drift' experiments in Chapter 6. A useful theoretical contribution to the field would be to develop a mathematical model which predicts the impact of circulation changes over one continent depending on the distance between the two and the strength of the circulation anomaly.

In addition, we briefly discussed the impact of a hemispherically symmetric annual mean sea surface temperature distribution on precipitation change over land in Chapter 4. When the annual mean temperature maximum was centered at the Equator, rainfall increased over the Amazon basin in the idealised and realistic simulations. According to previous studies, the location of the ITCZ is sensitive to the meridional SST gradient, albeit the energy budget of the atmosphere provides a more reliable framework (Kang et al., 2008; Donohoe et al., 2013; Maroon et al., 2016). In addition, SST anomalies play a central role in tropical precipitation change (Chadwick et al., 2014; Xie et al., 2010; Neelin and Held, 1987). While the SST distribution was not the focus of this thesis, further investigation is called for in the future, linking the location of the ITCZ and continental rainfall changes for the two different SST distributions to atmospheric energy transports.

In Chapter 5, we proposed one possible mechanism for the local drying response over the idealised Amazon basin when stomatal conductance decreases with warming. Due to energetic constraints on evaporation in the Equatorial region of idealised America – which were essentially a consequence of the high rainfall rates in the unperturbed climate – evaporation did not increase in step with precipitation. Therefore, moisture for the precipitation increase was provided from the surrounding land regions, reducing the humidity available for rainfall there, thus drying out the idealised Amazon basin. A similar mechanism might have contributed to drying of parts of the Amazon basin in the simulation with realistic continents.

Currently, the causal relationship between the increase in $P - E$ near the Equator and decrease in the idealised Amazon basin remains unclear. In future work, model data with a higher temporal resolution (hourly instead of monthly) will be saved and analysed, in order to investigate whether the $P - E$ increase at the Equator occurs first, leading to the stronger moisture flux divergence in the

idealised Amazon basin or whether the response in the latter region precedes the Equatorial response.

In Chapter 6, we found that a monsoon-type behaviour was exhibited over land even when the heat capacities of land and ocean were the same, only due to limited evaporation over land. We discussed that the farther poleward migration of the ITCZ over land compared to ocean can be understood in terms of the near-surface moist static energy (MSE_b, Privé and Plumb, 2007). While our results agreed with the theory over land, in that the precipitation maximum was co-located with or equatorward of the MSE_b maximum, the same was not true over the ocean. Privé and Plumb (2007) mentioned a similar behaviour in some aquaplanet simulations. Since the 'land' in our simulation was very similar to the ocean bar the surface hydrology, it would be interesting to see at which point Privé and Plumb's theory starts to 'break down'. This could be investigated in simulations where the 'land' properties are gradually changed from being equal to ocean to being more representative of an actual continent with higher albedo, lower thermal inertia and higher resistance to evaporation.

Those experiments would also yield interesting results concerning the strength of precipitation over land. A lower thermal inertia over land would be expected to result in a much larger zonal moist static energy contrast between land and ocean as land-surface temperatures and turbulent fluxes more closely follow the seasonal migration of the Sun. This would impact the zonal circulation and advection of moisture onto the continent, impacting continental rainfall and thus essentially monsoon behavior. In the sense that the summer monsoons can be viewed as a regional manifestation of the ITCZ over land, additionally being influenced by characteristics of the land-surfaces, these experiments could provide interesting insight into the importance of different features of the land-surface relative to each other and the large-scale circulation.

Finally, I have discussed ideas for future work on investigating paleo-monsoons in Isca with Prof. Dan Lunt and Dr. Alex Farnsworth at the University of Bristol. In their recent work, Farnsworth et al. (2019) showed that changes in paleogeography, rather than CO_2 concentrations led to variations in the East-Asian monsoon strength over the past 150 million years. One of the key mechanisms proposed in their study is a shift of the west Pacific warm pool towards the central Pacific, modifying the Walker circulation and leading to a drier East-Asian monsoon during the

Late Cretaceous (100.5 - 66 million years ago). We propose to use the continental configurations from their study for a wetter and a drier East Asian monsoon period in Isca, with and without topography, and with a slab ocean or with prescribed sea surface temperature distributions derived from their study. With these experiments, it might be possible to provide further evidence supporting their findings, or to identify novel mechanisms controlling the East-Asian monsoon over the past 150 million years. The advantage of using Isca (or other idealised Atmospheric GCM), particularly in this case would be the computational efficiency and thus ease of testing hypotheses compared to the authors' original experiments with a coupled atmosphere-ocean GCM, which required several thousand years of spin-up until near-equilibrium was reached. By prescribing the sea-surface temperature distributions from their study or using a mixed-layer ocean, this step can be bypassed.

7.2 Concluding Remarks

The findings presented in this thesis have contributed to the understanding of tropical precipitation change due to increasing CO_2 concentrations, particularly over the Amazon basin, Equatorial Africa and the Maritime Continent. The precipitation decrease in the Amazon basin has been connected to limited evaporation over land and enhanced rainfall over Equatorial Africa. Local mechanisms over South America lead to an amplification of this drying when vegetation changes are included. Over a narrow island such as Sulawesi in the Maritime Continent, moisture advection from the surrounding ocean leads to strong precipitation, particularly in the absence of any continental evaporation. The energy budget of the atmosphere provides a more reliable diagnostic framework for precipitation changes in response to a surface warming than the Matsuno-Gill theory, particularly when atmospheric moisture changes occur together with the warming of the surface.

These results provide answers to the questions what drives zonally asymmetric precipitation responses in the tropics, why these rainfall anomalies are amplified when vegetation changes are included and which mechanisms control tropical rainfall and precipitation changes over land and ocean. The findings from

this thesis also raised several new questions which have been outlined in the previous section as a guidance for future research.

Appendix

In Chapter 4, Welch's t-test was used in order to determine in which regions the precipitation change exceeds the natural variability in an experiment with realistic continents and bucket hydrology. In order to apply Welch's t-test, the python function *ttest_ind* from the scipy.stats module for unequal variances was used.

Welch's t-test, an adaptation of Student's t-test for samples with unequal variances, can be used to assess whether the means of two samples are sufficiently different in order to reject the 'null-hypothesis' of equal means (Welch, 1947; Derrick et al., 2016). In this case, we tested – at each model grid-point – whether the time-series of annual-mean precipitation in the perturbed climate was significantly different from the time-series in the control climate.

The *ttest_ind* function determines the t-value

$$t = \frac{\overline{x_1} - \overline{x_2}}{\sqrt{\frac{s_1^2}{N_1^2} + \frac{s_2^2}{N_2^2}}} \tag{A1}$$

and the degrees of freedom using the Welch–Satterthwaite equation

$$\nu = \frac{\left(\frac{s_1^2}{N_1^2} + \frac{s_2^2}{N_2^2}\right)^2}{\frac{s_1^4}{N_1^2 \cdot (N_1 - 1)} + \frac{s_2^4}{N_2^2 \cdot (N_2 - 1)}} \tag{A2}$$

separately for each grid-point, based on the sample means (X_i), the sample standard deviations (s_i) and the sample sizes (N_i), where the subscript i denotes sample 1 and 2, and in our case the two samples are the time-series of annual mean precipitation in the control climate (Sample 1) and perturbed climate (Sample 2). Based on the test statistic (t) and the degrees of freedom (ν), the shape of the t-distribution is determined. The two-tailed test then determines the probability (the p-value) that the value of t would be less than or greater than what

we obtained through the calculation if the null-hypothesis of equal means were in fact true, and hence could not be rejected. The p-value is equal to the area under the t-distribution to the left of $-t$ plus the area under the t-curve to the right of $+t$, where t is calculated using Equation A1. If this p-value is lower than the threshold α (here α = 0.05), we reject the null hypothesis of equal means, and hence detect a significant change in climate rather than internal variability in this grid-point.

In order to apply Welch's t-test we need to be able to make the assumption that the means of the samples follow a normal distribution, and that the data are independent. Unlike for Student's t-test, the assumption of equal variances does not need to be made for Welch's t-test.

The Shapiro-Wilk test was applied to assess whether a normal distribution can be assumed in each grid-point (Ghasemi and Zahediasl, 2012). The Shapiro-Wilk test was performed using the function *shapiro* from the scipy.stats module in python. Figure A1 shows the p-value for the Shapiro-Wilk test in each grid-point for the control climate, where all p-values less than 0.05 have been masked. Where the p-value is less than 0.05, the null-hypothesis of a normal distribution has to be rejected, and thus strictly speaking the first assumption for the Welch's t-test is not fulfilled.

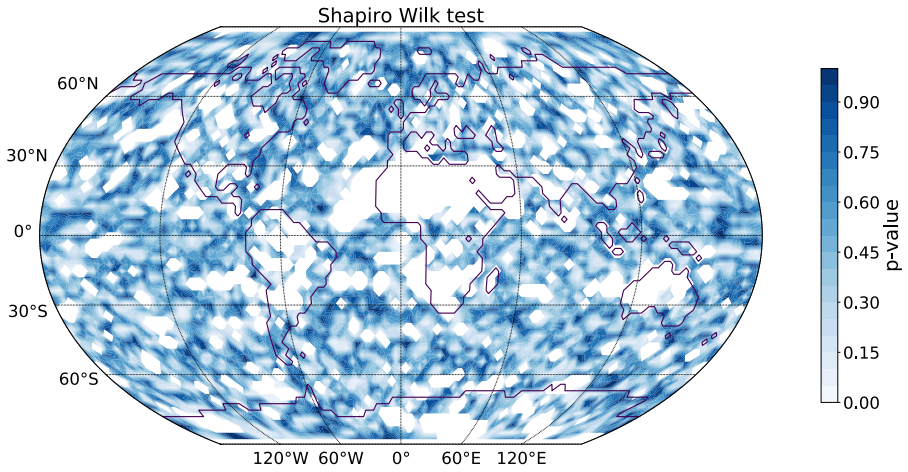

Figure A1: p-values from the Shapiro-Wilk test for the time-series of annual mean control precipitation for the RC experiment with realistic continents, topography and bucket hydrology from Chapter 4. Masked areas indicate where the p-value is less than 0.05 and hence the null-hypothesis of normal distribution must be rejected, i.e. we can not assume a normal distribution of the data in that grid-point.

We performed Welch's t-test on the time-series of annual mean data, which are more likely to fulfill the independence criterion compared to monthly data. Figure A2 shows the one-year lagged auto-correlation coefficient, with $|r| \geq 0.3$ masked. The auto-correlation was performed using the python function *pearsonr* from the scipy.stats module with a lag of one year. Generally, the auto-correlation is low (less than 0.3), with only a few locations that have a correlation coefficient greater than 0.3.

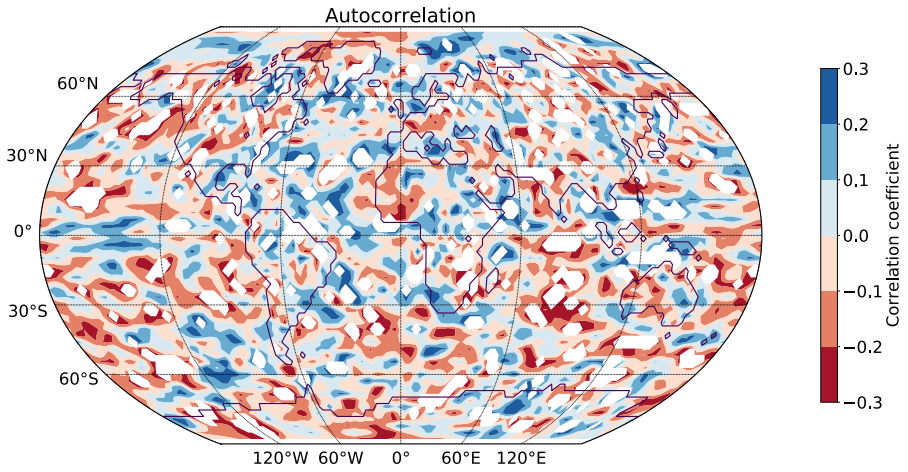

Figure A2: Pearson correlation coefficient of one-year lagged auto-correlation for the time-series of annual mean control precipitation from the RC experiment from Chapter 4. Masked areas (white) indicate where the correlation coefficient is greater than 0.3 or less than -0.3, i.e. we can not assume independence of the data in that grid-point.

Figure A3 is the same as Figure 4.2 from the main text, but with the areas masked where either the Shapiro-Wilk test has a p-value > 0.05 (and hence the assumption of normal distribution of the data is not fulfilled), or where the auto-correlation is greater than 0.3 (and hence the data are less likely to be independent). Most areas are masked due to the assumption of normal distribution not being fulfilled. In the masked areas (for example the desert regions of Africa and Australia, which are not of central importance to this thesis, but also over parts of South America), the Welch's t-test is less robust and the results should be interpreted with caution.

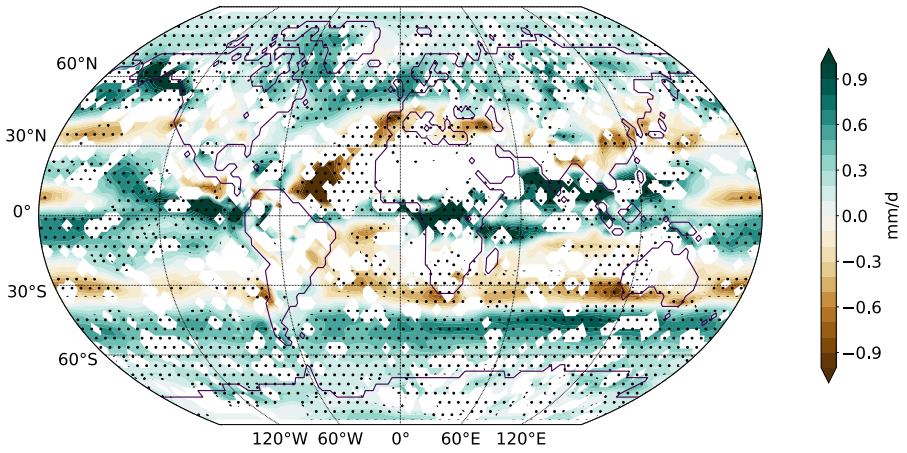

Figure A3: Precipitation change (colours) for the RC experiment from Chapter 4. Masked areas (white) show regions where one of the assumptions for the Welch's t-test (normality or independence) is not fulfilled. Stippling indicates regions where Welch's t-test suggests that the two time-series (control and perturbed climate) are significantly different from each other.

Bibliography

Ainsworth, E. and Rogers, A. (2007). The response of photosynthesis and stomatal conductance to rising [CO2]: mechanisms and environmental interactions. *Plant, Cell & Environment*, 30(3):258–270. doi: 10.1111/j.1365-3040.2007.01641.x.

Ainsworth, E. A. and Long, S. P. (2005). What have we learned from 15 years of free-air CO2 enrichment (FACE)? A meta-analytic review of the responses of photosynthesis, canopy properties and plant production to rising CO2. *New Phytologist*, 165(2):351–372. doi: 10.1111/j.1469-8137.2004.01224.x.

Allen, R. and Ingram, W. J. (2002). Constraints on future changes in climate and the hydrologic cycle. *Nature*, 419:228 – 232. doi: 10.1038/nature01092.

Battisti, D. S., Vimont, D. J., and Kirtman, B. P. (2018). 100 Years of Progress in Understanding the Dynamics of Coupled Atmosphere–Ocean Variability. *Meteorological Monographs*, 59:8.1–8.57. doi: 10.1175/AMSMONOGRAPHS-D-18-0025.1.

Best, M. J., Pryor, M., Clark, D. B., Rooney, G. G., Essery, R. L. H., Ménard, C. B., Edwards, J. M., Hendry, M. A., Porson, A., Gedney, N., Mercado, L. M., Sitch, S., Blyth, E., Boucher, O., Cox, P. M., Grimmond, C. S. B., and Harding, R. J. (2011). The joint uk land environment simulator (jules), model description – part 1: Energy and water fluxes. *Geoscientific Model Development*, 4(3):677–699. doi: 10.5194/gmd-4-677-2011.

Betts, A. K. (1986). A new convective adjustment scheme. Part I: Observational and theoretical basis. *Quarterly Journal of the Royal Meteorological Society*, 112(473):677–691. doi: 10.1002/qj.49711247307.

Betts, A. K. and Miller, M. J. (1986). A new convective adjustment scheme. Part II:

Single column tests using GATE wave, BOMEX, ATEX and arctic air-mass data sets. *Quarterly Journal of the Royal Meteorological Society*, 112(473):693–709. doi: 10.1002/qj.49711247308.

Bischoff, T. and Schneider, T. (2014). Energetic Constraints on the Position of the Intertropical Convergence Zone. *Journal of Climate*, 27(13):4937–4951. doi: 10.1175/JCLI-D-13-00650.1.

Bjerknes, J. (1969). Atmospheric Teleconnections . *Monthly Weather Review*, 97(3):163–172. doi: 10.1175/1520-0493(1969)097<0163:ATFTEP>2.3.CO;2.

Blandford, H. F. (1886). Rainfall of India. *Monsoon Monograph - India Meteorological Department*, 3(658).

Boer, G. J. (1993). Climate change and the regulation of the surface moisture and energy budgets. *Climate Dynamics*, 8(5):225–239. doi: 10.1007/BF00198617.

Bonan, G. B. (2008). Forests and Climate Change: Forcings, Feedbacks, and the Climate Benefits of Forests. *Science*, 320(5882):1444–1449. doi: 10.1126/science.1155121.

Boos, W. and Korty, R. (2016). Regional energy budget control of the intertropical convergence zone and application to mid-Holocene rainfall. *Nature Geosci.*, 9:892 – 897. https://doi.org/10.1038/ngeo2833.

Bordoni, S. and Schneider, T. (2008). Monsoons as eddy-mediated regime transitions of the tropical overturning circulation. *Nature Geosci*, 1:515–519. https://doi.org/10.1038/ngeo248.

Broccoli, A. J., Dahl, K. A., and Stouffer, R. J. (2006). Response of the ITCZ to Northern Hemisphere cooling. *Geophysical Research Letters*, 33(1). doi: 10.1029/2005GL024546.

Budyko, M. I. (1974). *Climate and Life*. Academic Press, New York and London. English ed. edited by David H. Miller. ISBN 0-12-139450-6.

Byrne, M. P. and O'Gorman, P. A. (2013). Land–Ocean Warming Contrast over a Wide Range of Climates: Convective Quasi-Equilibrium Theory and Idealized Simulations. *Journal of Climate*, 26(12):4000–4016. doi: 10.1175/JCLI-D-12-00262.1.

Byrne, M. P. and O'Gorman, P. A. (2015). The Response of Precipitation Minus Evapotranspiration to Climate Warming: Why the "Wet-Get-Wetter, Dry-Get-Drier" Scaling Does Not Hold over Land. *Journal of Climate*, 28(20):8078–8092. doi: 10.1175/JCLI-D-15-0369.1.

Byrne, M. P. and O'Gorman, P. A. (2016). Understanding Decreases in Land Relative Humidity with Global Warming: Conceptual Model and GCM Simulations. *Journal of Climate*, 29(24):9045–9061. doi: 10.1175/JCLI-D-16-0351.1.

Byrne, M. P. and Schneider, T. (2016). Narrowing of the ITCZ in a warming climate: Physical mechanisms. *Geophysical Research Letters*, 43(21). doi: 10.1002/2016GL070396.

Chadwick, R., Ackerley, D., Ogura, T., and Dommenget, D. (2019). Separating the Influences of Land Warming, the Direct CO2 Effect, the Plant Physiological Effect, and SST Warming on Regional Precipitation Changes, journal = Journal of Geophysical Research: Atmospheres. 124(2):624–640. doi: 10.1029/2018JD029423.

Chadwick, R., Boutle, I., and Martin, G. (2013). Spatial Patterns of Precipitation Change in CMIP5: Why the Rich Do Not Get Richer in the Tropics. *Journal of Climate*, 26(11):3803–3822. doi: 10.1175/JCLI-D-12-00543.1.

Chadwick, R., Douville, H., and Skinner, C. B. (2017). Timeslice experiments for understanding regional climate projections: applications to the tropical hydrological cycle and European winter circulation. *Climate Dynamics*, 49(9). doi: 10.1007/s00382-016-3488-6.

Chadwick, R., Good, P., Andrews, T., and Martin, G. (2014). Surface warming patterns drive tropical rainfall pattern responses to CO2 forcing on all timescales. *Geophysical Research Letters*, 41(2):610–615. doi: 10.1002/2013GL058504.

Chadwick, R., Good, P., and Willett, K. (2016). A Simple Moisture Advection Model of Specific Humidity Change over Land in Response to SST Warming. *Journal of Climate*, 29(21):7613–7632. doi: 10.1175/JCLI-D-16-0241.1.

Charney, J. G. (1975). Dynamics of deserts and drought in the sahel. *Quarterly Journal of the Royal Meteorological Society*, 101(428):193–202. doi: 10.1002/qj.49710142802.

Chou, C., Neelin, J. D., and Su, H. (2001). Ocean-atmosphere-land feedbacks in an idealized monsoon. *Quarterly Journal of the Royal Meteorological Society*, 127(576):1869–1891. doi: 10.1002/qj.49712757602.

Clark, D. B., Mercado, L. M., Sitch, S., Jones, C. D., Gedney, N., Best, M. J., Pryor, M., Rooney, G. G., Essery, R. L. H., Blyth, E., Boucher, O., Harding, R. J., Huntingford, C., and Cox, P. M. (2011). The joint uk land environment simulator (jules), model description – part 2: Carbon fluxes and vegetation dynamics. *Geoscientific Model Development*, 4(3):701–722. doi: 10.5194/gmd-4-701-2011.

Clough, S., Shephard, M., Mlawer, E., Delamere, J., Iacono, M., Cady-Pereira, K., Boukabara, S., and Brown, P. (2005). Atmospheric radiative transfer modeling: a summary of the aer codes. *Journal of Quantitative Spectroscopy and Radiative Transfer*, 91(2):233 – 244. https://doi.org/10.1016/j.jqsrt.2004.05.058.

Collins, M., Knutti, R., Arblaster, J., Dufresne, J.-L., Fichefet, T., Friedlingstein, P., Gao, X., Gutowski, W. J., Johns, T., Krinner, G., Shongwe, M., Tebaldi, C., Weaver, A. J., and Wehner, M. (2013). *Long-term Climate Change: Projections, Commitments and Irreversibility Pages 1029 to 1076*, page 1029–1136. Cambridge University Press. doi: 10.1017/CBO9781107415324.024.

Cook, K. H., Hsieh, J.-S., and Hagos, S. M. (2004). The Africa–South America Intercontinental Teleconnection. *Journal of Climate*, 17(14):2851–2865. doi: 10.1175/1520-0442(2004)017<2851:TAAIT>2.0.CO;2.

Cubasch, U., Meehl, G., Boer, G., Stouffer, R., Dix, M., Noda, A., Senior, C., Raper, S., and Yap, K. (2001). *Projections of future climate change, in Climate Change 2001: The Scientific Basis. Contribution of Working Group I to the Third Assessment Report of the Intergovernmental Panel on Climate Change, edited by J. T. Houghton et al.*, pages 525 – 582. Cambridge University Press.

De Kauwe, M. G., Medlyn, B. E., Zaehle, S., Walker, A. P., Dietze, M. C., Hickler, T., Jain, A. K., Luo, Y., Parton, W. J., Prentice, I. C., Smith, B., Thornton, P. E., Wang, S., Wang, Y.-P., Wårlind, D., Weng, E., Crous, K. Y., Ellsworth, D. S., Hanson, P. J., Seok Kim, H., Warren, J. M., Oren, R., and Norby, R. J. (2013).

Forest water use and water use efficiency at elevated CO2: a model-data intercomparison at two contrasting temperate forest FACE sites. *Global Change Biology*, 19(6):1759–1779. doi: 10.1111/gcb.12164.

Dee, D. P., Uppala, S. M., Simmons, A. J., Berrisford, P., Poli, P., Kobayashi, S., Andrae, U., Balmaseda, M. A., Balsamo, G., Bauer, P., Bechtold, P., Beljaars, A. C. M., van de Berg, L., Bidlot, J., Bormann, N., Delsol, C., Dragani, R., Fuentes, M., Geer, A. J., Haimberger, L., Healy, S. B., Hersbach, H., Hólm, E. V., Isaksen, L., Kållberg, P., Köhler, M., Matricardi, M., McNally, A. P., Monge-Sanz, B. M., Morcrette, J.-J., Park, B.-K., Peubey, C., de Rosnay, P., Tavolato, C., Thépaut, J.-N., and Vitart, F. (2011). The ERA-Interim reanalysis: configuration and performance of the data assimilation system. *Quarterly Journal of the Royal Meteorological Society*, 137(656):553–597. doi: 10.1002/qj.828.

Derrick, B., Toher, D., and White, P. (2016). Why Welch's test is Type I error robust. *The Quantitative Methods in Psychology*, 12:30–38. https://uwe-repository.worktribe.com/output/915692.

Dima, I. M. and Wallace, J. M. (2003). On the Seasonality of the Hadley Cell. *Journal of the Atmospheric Sciences*, 60(12):1522–1527. doi: 10.1175/1520-0469(2003)060<1522:OTSOTH>2.0.CO;2.

Dong, B., Gregory, J. M., and Sutton, R. T. (2009). Understanding Land–Sea Warming Contrast in Response to Increasing Greenhouse Gases. Part I: Transient Adjustment. *Journal of Climate*, 22(11):3079–3097. doi: 10.1175/2009JCLI2652.1.

Donohoe, A., Marshall, J., Ferreira, D., and Mcgee, D. (2013). The Relationship between ITCZ Location and Cross-Equatorial Atmospheric Heat Transport: From the Seasonal Cycle to the Last Glacial Maximum. *Journal of Climate*, 26(11):3597–3618. doi: 10.1175/JCLI-D-12-00467.1.

Erfanian, A. and Fomenko, L. (2017). Unprecedented drought over tropical South America in 2016: significantly under-predicted by tropical SST. *Scientific Reports*, 7. doi: 10.1038/s41598-017-05373-2.

Farnsworth, A., Lunt, D. J., Robinson, S. A., Valdes, P. J., Roberts, W. H. G., Clift, P. D., Markwick, P., Su, T., Wrobel, N., Bragg, F., Kelland, S.-J., and Pancost,

R. D. (2019). Past East Asian monsoon evolution controlled by paleogeography, not CO2. *Science Advances*, 5(10). doi: 10.1126/sciadv.aax1697.

Fasullo, J. T. and Trenberth, K. E. (2008). The Annual Cycle of the Energy Budget. Part II: Meridional Structures and Poleward Transports. *Journal of Climate*, 21(10):2313–2325. doi: 10.1175/2007JCLI1936.1.

Frierson, D. M. W. (2007). The Dynamics of Idealized Convection Schemes and Their Effect on the Zonally Averaged Tropical Circulation. *Journal of the Atmospheric Sciences*, 64(6):1959–1976. doi: 10.1175/JAS3935.1.

Frierson, D. M. W., Held, I. M., and Zurita-Gotor, P. (2006). A Gray-Radiation Aquaplanet Moist GCM. Part I: Static Stability and Eddy Scale. *Journal of the Atmospheric Sciences*, 63(10):2548–2566. doi: 10.1175/JAS3753.1.

Frierson, D. M. W. and Hwang, Y.-T. (2012). Extratropical Influence on ITCZ Shifts in Slab Ocean Simulations of Global Warming. *Journal of Climate*, 25(2):720–733. doi: 10.1175/JCLI-D-11-00116.1.

Frierson, D. M. W., Hwang, Y.-T., Fučkar, N. S., Seager, R., Kang, S. M., Donohoe, A., Marron, E. A., Liu, X., and Battisti, D. S. (2013). Contribution of ocean overturning circulation to tropical rainfall peak in the Northern Hemisphere. *Nature Geoscience*, 6(11):940 – 944. doi: 10.1038/ngeo1987.

Gadgil, S. (2018). The monsoon system: Land–sea breeze or the ITCZ? *J Earth Syst Sci*, 127(1). https://doi.org/10.1007/s12040-017-0916-x@.

Gates, W. L. (1992). AMIP: The Atmospheric Model Intercomparison Project. *Bulletin of the American Meteorological Society*, 73(12):1962–1970. doi: 10.1175/1520-0477(1992)073<1962:ATAMIP>2.0.CO;2.

Geen, R., Bordoni, S., Battisti, D. S., and Hui, K. L. (2020). The Dynamics of the Global Monsoon: Connecting Theory and Observations. *Earth and Space Science Open Archive*, page 50. doi: 10.1002/essoar.10502409.1.

Geen, R., Lambert, F. H., and Vallis, G. K. (2018). Regime Change Behavior during Asian Monsoon Onset. *Journal of Climate*, 31(8):3327–3348. doi: 10.1175/JCLI-D-17-0118.1.

Geen, R., Lambert, F. H., and Vallis, G. K. (2019). Processes and Timescales in Onset and Withdrawal of “Aquaplanet Monsoons”. *Journal of the Atmospheric Sciences*, 76(8):2357–2373. doi: 10.1175/JAS-D-18-0214.1.

Ghasemi, A. and Zahediasl, S. (2012). Normality Tests for Statistical Analysis: A Guide for Non-Statisticians. *International Journal of Endocrinology and Metabolism*, 10(2):486–489. doi: 10.5812/ijem.3505.

Gill, A. E. (1980). Some simple solutions for heat-induced tropical circulation. *Quarterly Journal of the Royal Meteorological Society*, 106(449):447–462. doi: 10.1002/qj.49710644905.

Hadley, G. (1735). Concerning the cause of the general trade-winds. *Phil. Trans.*, 29:58 – 62.

Halley, E. (1687). An historical account of the trade winds, and monsoons, observable in the seas between and near the Tropicks, with an attempt to assign the physical cause of the said winds. *Philosophical Transactions of the Royal Society of London*, 16(183):153–168. doi: 10.1098/rstl.1686.0026.

Hastenrath, S. and Heller, L. (1977). Dynamics of climatic hazards in northeast Brazil. *Quarterly Journal of the Royal Meteorological Society*, 103(435):77–92. doi: 10.1002/qj.49710343505.

Held, I. (2014). Simplicity amid Complexity. *Science*, 343(6176):1206–1207. doi: 10.1126/science.1248447.

Held, I. M. (2001). The Partitioning of the Poleward Energy Transport between the Tropical Ocean and Atmosphere. *Journal of the Atmospheric Sciences*, 58(8):943–948. doi: 10.1175/1520-0469(2001)058<0943:TPOTPE>2.0.CO;2.

Held, I. M. (2005). The Gap between Simulation and Understanding in Climate Modeling. *Bulletin of the American Meteorological Society*, 86(11):1609–1614. doi: 10.1175/BAMS-86-11-1609.

Held, I. M. and Soden, B. J. (2006). Robust Responses of the Hydrological Cycle to Global Warming. *Journal of Climate*, 19(21):5686–5699. doi: 10.1175/JCLI3990.1.

Hill, S. A. (2019). Theories for Past and Future Monsoon Rainfall Changes. *Curr Clim Change Rep*, 5:160–171. https://doi.org/10.1007/s40641-019-00137-8.

Hill, S. A., Ming, Y., Held, I. M., and Zhao, M. (2017). A Moist Static Energy Budget–Based Analysis of the Sahel Rainfall Response to Uniform Oceanic Warming. *Journal of Climate*, 30(15):5637–5660. doi: 10.1175/JCLI-D-16-0785.1.

Holland, M. M. and Bitz, C. M. (2003). Polar amplification of climate change in coupled models. *Climate Dynamics*, 21:221–232. https://doi.org/10.1007/s00382-003-0332-6.

Holton, J. R. (2004). *An Introduction to Dynamic Meteorology*. Elsevier Academic Press. 4th Edition. ISBN: 0-12-354015-1.

Inoue, K. and Back, L. E. (2015). Gross moist stability assessment during TOGA COARE: Various interpretations of gross moist stability. *J. Atmos. Sci.*, 72(11):4148–4166. doi: 10.1175/JAS-D-15-0092.1.

IPCC (2013). *Summary for Policymakers. In: Climate Change 2013: The Physical Science Basis.Contribution of Working Group I to the Fifth Assessment Report of the Intergovernmental Panel on Climate Change [Stocker, T.F., D. Qin, G.-K. Plattner, M. Tignor, S.K. Allen, J. Boschung, A. Nauels, Y. Xia, V. Bex and P.M. Midgley (eds.)]. Cambridge University Press, Cambridge, United Kingdom and New York, NY, USA.*

Jiménez-Esteve, B. and Domeisen, D. I. V. (2019). Nonlinearity in the North Pacific Atmospheric Response to a Linear ENSO Forcing. *Geophysical Research Letters*, 46(4):2271–2281. doi: 10.1029/2018GL081226.

Joshi, M. M., Gregory, J. M., Webb, M. J., Sexton, D. M. H., and Johns, T. C. (2008). Mechanisms for the land/sea warming contrast exhibited by simulations of climate change. *Climate Dynamics*, 30(5):455–465. doi: 10.1007/s00382-007-0306-1.

Julian, P. R. and Chervin, R. M. (1978). A Study of the Southern Oscillation and Walker Circulation Phenomenon. *Monthly Weather Review*, 106(10):1433–1451. doi: 10.1175/1520-0493(1978)106<1433:ASOTSO>2.0.CO;2.

Kalnay, E., Kanamitsu, M., Kistler, R., Collins, W., Deaven, D., Gandin, L., Iredell, M., Saha, S., White, G., Woollen, J., Zhu, Y., Chelliah, M., Ebisuzaki, W., Higgins, W., Janowiak, J., Mo, K. C., Ropelewski, C., Wang, J., Leetmaa, A., Reynolds, R., Jenne, R., and Joseph, D. (1996). The NCEP/NCAR 40-Year Reanalysis Project. *Bulletin of the American Meteorological Society*, 77(3):437–472. doi: 10.1175/1520-0477(1996)077<0437:TNYRP>2.0.CO;2.

Kang, S. and Ahn, J. (2015). Global energy and water balances in the latest reanalyses. *Asia-Pacific J Atmos Sci*, 51:293–302. https://doi.org/10.1007/s13143-015-0079-0.

Kang, S. M., Frierson, D. M. W., and Held, I. M. (2009). The Tropical Response to Extratropical Thermal Forcing in an Idealized GCM: The Importance of Radiative Feedbacks and Convective Parameterization. *Journal of the Atmospheric Sciences*, 66(9):2812–2827. doi: 10.1175/2009JAS2924.1.

Kang, S. M., Held, I. M., Frierson, D. M. W., and Zhao, M. (2008). The Response of the ITCZ to Extratropical Thermal Forcing: Idealized Slab-Ocean Experiments with a GCM. *Journal of Climate*, 21(14):3521–3532. doi: 10.1175/2007JCLI2146.1.

Kooperman, G. J., Chen, Y., Hoffman, F. M., Koven, C. D., Lindsay, K., Pritchard, M. S., Swann, A. L. S., and Randerson, J. T. (2018). Forest response to rising CO2 drives zonally asymmetric rainfall change over tropical land. *Nature Climate Change*, 8. doi: 10.1038/s41558-018-0144-7.

Koster, R. D. and Mahanama, S. P. P. (2012). Land Surface Controls on Hydroclimatic Means and Variability. *Journal of Hydrometeorology*, 13(5):1604–1620. doi: 10.1175/JHM-D-12-050.1.

Laguë, M. M., Pietschnig, M., Ragen, S., Smith, T. A., and Battisti, D. S. (2020). Northland: the climate of an Earth with a hemispheric continent. *EarthArXiv*. https://doi.org/10.31223/osf.io/qjne3.

Lambert, F. H. and Chiang, J. C. H. (2007). Control of land-ocean temperature contrast by ocean heat uptake. *Geophysical Research Letters*, 34(13). doi: 10.1029/2007GL029755.

Lambert, F. H., Ferraro, A. J., and Chadwick, R. (2017). Land–Ocean Shifts in Tropical Precipitation Linked to Surface Temperature and Humidity Change. *Journal of Climate*, 30(12):4527–4545. doi: 10.1175/JCLI-D-16-0649.1.

Lambert, F. H., Webb, M. J., and Joshi, M. M. (2011). The Relationship between Land–Ocean Surface Temperature Contrast and Radiative Forcing. *Journal of Climate*, 24(13):3239–3256. doi: 10.1175/2011JCLI3893.1.

Langenbrunner, B., Pritchard, M. S., Kooperman, G. J., and Randerson, J. T. (2019). Why Does Amazon Precipitation Decrease When Tropical Forests Respond to Increasing CO2? *Earth's Future*, 7(4):450–468. doi: 10.1029/2018EF001026.

Larsen, J., Anisimov, O., Constable, A., Hollowed, A., Maynard, N., Prestrud, P., Prowse, T., and Stone, J. (2014). *Polar regions. In: Climate Change 2014: Impacts, Adaptation, and Vulnerability. Part B: Regional Aspects. Contribution of Working Group II to the Fifth Assessment Report of the Intergovernmental Panel on Climate Change [Barros, V.R., C.B. Field, D.J. Dokken, M.D. Mastrandrea, K.J. Mach, T.E. Bilir, M. Chatterjee, K.L. Ebi, Y.O. Estrada, R.C. Genova, B. Girma, E.S. Kissel, A.N. Levy, S. MacCracken, P.R. Mastrandrea, and L.L. White (eds.)]*, pages 1567–1612. Cambridge University Press, Cambridge, United Kingdom and New York, NY, USA.

Lau, W. K. M. and Kim, K.-M. (2015). Robust Hadley Circulation changes and increasing global dryness due to CO2 warming from CMIP5 model projections. *Proceedings of the National Academy of Sciences*, 112(12):3630–3635. doi: 10.1073/pnas.1418682112.

Li, D., Pan, M., Cong, Z., Zhang, L., and Wood, E. (2013). Vegetation control on water and energy balance within the Budyko framework. *Water Resources Research*, 49(2):969–976. doi: 10.1002/wrcr.20107.

Maher, P., Gerber, E. P., Medeiros, B., Merlis, T. M., Sherwood, S., Sheshadri, A., Sobel, A. H., Vallis, G. K., Voigt, A., and Zurita-Gotor, P. (2019). Model Hierarchies for Understanding Atmospheric Circulation. *Reviews of Geophysics*, 57(2):250–280. doi: 10.1029/2018RG000607.

Mahowald, N., Lo, F., Zheng, Y., Harrison, L., Funk, C., Lombardozzi, D., and Goodale, C. (2016). Projections of leaf area index in earth system models. *Earth System Dynamics*, 7(1):211–229. doi: 10.5194/esd-7-211-2016.

Manabe, S. (1969). Climate and the Ocean Circulation. *Mon. Weather Rev.*, 97:739–774.

Manabe, S., Stouffer, R. J., Spelman, M. J., and Bryan, K. (1991). Transient Responses of a Coupled Ocean–Atmosphere Model to Gradual Changes of Atmospheric CO2. Part I. Annual Mean Response. *Journal of Climate*, 4(8):785–818. doi: 10.1175/1520-0442(1991)004<0785:TROACO>2.0.CO;2.

Manabe, S. and Strickler, R. F. (1964). Thermal Equilibrium of the Atmosphere with a Convective Adjustment. *Journal of the Atmospheric Sciences*, 21(4):361–385. doi: 10.1175/1520-0469(1964)021<0361:TEOTAW>2.0.CO;2.

Manabe, S. and Wetherald, R. T. (1975). The Effects of Doubling the CO2 Concentration on the climate of a General Circulation Model. *Journal of the Atmospheric Sciences*, 32(1):3–15. doi: 10.1175/1520-0469(1975)032<0003:TEODTC>2.0.CO;2.

Marengo, J. A., Liebmann, B., Grimm, A. M., Misra, V., Silva Dias, P. L., Cavalcanti, I. F. A., Carvalho, L. M. V., Berbery, E. H., Ambrizzi, T., Vera, C. S., Saulo, A. C., Nogues-Paegle, J., Zipser, E., Seth, A., and Alves, L. M. (2012). Recent developments on the South American monsoon system. *International Journal of Climatology*, 32(1):1–21. doi: 10.1002/joc.2254.

Marengo, J. A., Tomasella, J., Alves, L. M., Soares, W. R., and Rodriguez, D. A. (2011). The drought of 2010 in the context of historical droughts in the Amazon region. *Geophysical Research Letters*, 38(12). doi: 10.1029/2011GL047436.

Maroon, E. A., Frierson, D. M. W., Kang, S. M., and Scheff, J. (2016). The Precipitation Response to an Idealized Subtropical Continent. *Journal of Climate*, 29(12):4543–4564. doi: 10.1175/JCLI-D-15-0616.1.

Milly, P. C. D. (1994). Climate, soil water storage, and the average annual water balance. *Water Resources Research*, 30(7):2143–2156. doi: 10.1029/94WR00586.

Milly, P. C. D. and Dunne, K. A. (2016). Potential evapotranspiration and continental drying. *Nature Climate Change*, 6:946 – 949. doi: 10.1038/nclimate3046.

Mitchell, J. F. B., Wilson, C. A., and Cunnington, W. M. (1987). On co2 climate sensitivity and model dependence of results. *Quarterly Journal of the Royal Meteorological Society*, 113(475):293–322. doi: 10.1002/qj.49711347517.

Mlawer, E. J., Taubman, S. J., Brown, P. D., Iacono, M. J., and Clough, S. A. (1997). Radiative transfer for inhomogeneous atmospheres: Rrtm, a validated correlated-k model for the longwave. *Journal of Geophysical Research: Atmospheres*, 102(D14):16663–16682. doi: 10.1029/97JD00237.

Monteith, J. L. (1981). Evaporation and surface temperature. *Quarterly Journal of the Royal Meteorological Society*, 107(451):1–27. doi: 10.1002/qj.49710745102.

Moorthi, S. and Suarez, M. J. (1992). Relaxed Arakawa-Schubert. A Parameterization of Moist Convection for General Circulation Models. *Monthly Weather Review*, 120(6):978–1002. doi: 10.1175/1520-0493(1992)120<0978:RASAPO>2.0.CO;2.

Moron, V., Bigot, S., and Roucou, P. (1995). Rainfall variability in subequatorial America and Africa and relationships with the main sea-surface temperature modes (1951–1990). *International Journal of Climatology*, 15(12):1297–1322. doi: 10.1002/joc.3370151202.

Neelin, J. D. and Held, I. M. (1987). Modeling Tropical Convergence Based on the Moist Static Energy Budget. *Monthly Weather Review*, 115(1):3–12. doi: 10.1175/1520-0493(1987)115<0003:MTCBOT>2.0.CO;2.

Nie, J., Boos, W. R., and Kuang, Z. (2010). Observational Evaluation of a Convective Quasi-Equilibrium View of Monsoons. *Journal of Climate*, 23(16):4416–4428. doi: 10.1175/2010JCLI3505.1.

Oort, A. H. (1983). *Global Atmospheric Circulation Statistics, 1958 - 1973*. NOAA Professional Paper No. 14. U.S. Govt. Printing Office, Washington DC. 180 pp + 47 microfiches.

Oort, A. H. and Vonder Haar, T. H. (1976). On the Observed Annual Cycle in the Ocean-Atmosphere Heat Balance Over the Northern Hemisphere. *Journal of Physical Oceanography*, 6(6):781–800. doi: 10.1175/1520-0485(1976)006<0781:OTOACI>2.0.CO;2.

Osborne, J. M. and Lambert, F. H. (2018). A simple tool for refining gcm water availability projections, applied to chinese catchments. *Hydrology and Earth System Sciences*, 22(11):6043–6057. doi: 10.5194/hess-22-6043-2018.

Peixoto, J. P. and Oort, A. H. (1992). *Physics of Climate*. New York: American Institute of Physics. ISBN 0-88318-712-4.

Penman, H. L. (1948). Natural evaporation from open water, bare soil and grass. *Proceedings of the Royal Society of London. Series A. Mathematical and Physical Sciences*, 193(1032):120–145. doi: 10.1098/rspa.1948.0037.

Penn, J. and Vallis, G. K. (2018). Atmospheric Circulation and Thermal Phase-curve Offset of Tidally and Nontidally Locked Terrestrial Exoplanets. *The Astrophysical Journal*, 868(2):147. doi: 10.3847/1538-4357/aaeb20.

Peyser, C. E. and Poulsen, C. J. (2008). Controls on Permo-Carboniferous precipitation over tropical Pangaea: A GCM sensitivity study. *Palaeogeography, Palaeoclimatology, Palaeoecology*, 268(3):181 – 192. The late Paleozoic Earth system.

Pierrehumbert, R. (2002). The hydrologic cycle in deep-time climate problems. *Nature*, 419:191–198. https://doi.org/10.1038/nature01088.

Pierrehumbert, R. T. (1995). Thermostats, Radiator Fins, and the Local Runaway Greenhouse. *Journal of the Atmospheric Sciences*, 52(10):1784–1806. doi: 10.1175/1520-0469(1995)052<1784:TRFATL>2.0.CO;2.

Pietschnig, M., Lambert, F. H., Saint-Lu, M., and Vallis, G. K. (2019). The Presence of Africa and Limited Soil Moisture Contribute to Future Drying of South America. *Geophysical Research Letters*, 46. doi: 10.1029/2019GL084441.

Pithan, F. and Mauritsen, T. (2014). Arctic amplification dominated by temperature feedbacks in contemporary climate models. *Nature Geoscience*, 7:181–184. https://doi.org/10.1038/ngeo2071.

Polvani, L. M., Clement, A. C., Medeiros, B., Benedict, J. J., and Simpson, I. R. (2017). When less is more: Opening the door to simpler climate models. *EOS*, 98(6). https://doi.org/10.1029/2017EO079417.

Privé, N. C. and Plumb, R. A. (2007). Monsoon Dynamics with Interactive Forcing. Part I: Axisymmetric Studies. *Journal of the Atmospheric Sciences*, 64(5):1417–1430. doi: 10.1175/JAS3916.1.

Qian, W., Wu, K., and Liang, H. (2016). Arctic and Antarctic cells in the troposphere. *Theor Appl Climatol*, 125:1–12. https://doi.org/10.1007/s00704-015-1485-z.

Raymond, D. J., Sessions, S. L., Sobel, A. H., and Fuchs, (2009). The Mechanics of Gross Moist Stability. *Journal of Advances in Modeling Earth Systems*, 1(3). doi: 10.3894/JAMES.2009.1.9.

Roderick, M. L., Sun, F., Lim, W. H., and Farquhar, G. D. (2014). A general framework for understanding the response of the water cycle to global warming over land and ocean. *Hydrology and Earth System Sciences*, 18(5):1575–1589. doi: 10.5194/hess-18-1575-2014.

Rodwell, M. J. and Hoskins, B. J. (1996). Monsoons and the dynamics of deserts. *Quarterly Journal of the Royal Meteorological Society*, 122(534):1385–1404. doi: 10.1002/qj.49712253408.

Ropelewski, C. F. and Halpert, M. S. (1987). Global and Regional Scale Precipitation Patterns Associated with the El Niño/Southern Oscillation. *Monthly Weather Review*, 115(8):1606–1626. doi: 10.1175/1520-0493(1987)115<1606:GARSPP>2.0.CO;2.

Russell, G. L., Miller, J. R., and Tsang, L.-C. (1985). Seasonal oceanic heat transports computed from an atmospheric model. *Dynamics of Atmospheres and Oceans*, 9(3):253 – 271. http://dx.doi.org/10.1016/0377-0265(85)90022-3.

Saint-Lu, M., Chadwick, R., Lambert, F. H., and Collins, M. (2019). Surface Warming and Atmospheric Circulation Dominate Rainfall Changes Over Tropical Rainforests Under Global Warming. *Geophysical Research Letters*. doi: 10.1029/2019GL085295.

Salby, M. L. (1995). *Fundamentals of Atmospheric Physics*. Academic Press, San Diego, California and London, United Kingdom. Vol. 61, International Geophysics Series. ISBN 0-12-615160-1.

Scheff, J. and Frierson, D. (2012). Twenty-First-Century Multimodel Subtropical Precipitation Declines Are Mostly Midlatitude Shifts. *Journal of Climate*, 25(12):4330–4347. doi: 10.1175/JCLI-D-11-00393.1.

Scheff, J. and Frierson, D. M. W. (2014). Scaling potential evapotranspiration with greenhouse warming. *Journal of Climate*, 27(4):1539–1558. doi: 10.1175/JCLI-D-13-00233.1.

Schneider, S. H. and Dickinson, R. E. (1974). Climate modeling. *Reviews of Geophysics*, 12(3):447–493. doi: 10.1029/RG012i003p00447.

Schneider, T. (2006). The General Circulation of the Atmosphere. *Annual Review of Earth and Planetary Sciences*, 34(1):655–688. doi: 0.1146/annurev.earth.34.031405.125144.

Seager, R., Naik, N., and Vecchi, G. A. (2010). Thermodynamic and dynamic mechanisms for large-scale changes in the hydrological cycle in response to global warming. *Journal of Climate*, 23(17):4651–4668. doi: 10.1175/2010JCLI3655.1.

Sellers, P. J., Bounoua, L., Collatz, G. J., Randall, D. A., Dazlich, D. A., Los, S. O., Berry, J. A., Fung, I., Tucker, C. J., Field, C. B., and Jensen, T. G. (1996). Comparison of Radiative and Physiological Effects of Doubled Atmospheric CO2 on Climate. *Science*, 271(5254):1402–1406. doi: 10.1126/science.271.5254.1402.

Seo, J., Kang, S. M., and Merlis, T. M. (2017). A model intercomparison of the tropical precipitation response to a CO2 doubling in aquaplanet simulations. *Geophysical Research Letters*, 44(2):993–1000. doi: 10.1002/2016GL072347.

Shukla, J. and Mintz, Y. (1982). Influence of Land-Surface Evapotranspiration on the Earth's Climate. *Science*, 215(4539):1498–1501.

Skinner, C. B., Poulsen, C. J., Chadwick, R., Diffenbaugh, N. S., and Fiorella, R. P. (2017). The Role of Plant CO_2 Physiological Forcing in Shaping Future Daily-

Scale Precipitation. *Journal of Climate*, 30(7):2319–2340. doi: 10.1175/JCLI-D-16-0603.1.

Skinner, C. B., Poulsen, C. J., and Mankin, J. S. (2018). Amplification of heat extremes by plant CO_2 physiological forcing. *Nature Communications*, 9(1). doi: 10.1038/s41467-018-03472-w.

Smith, K., Woodward, A., Campbell-Lendrum, D., Chadee, D., Honda, Y., Liu, Q., Olwoch, J., Revich, B., and Sauerborn, R. (2014). *Human health: impacts, adaptation, and co-benefits. In: Climate Change 2014: Impacts, Adaptation, and Vulnerability. Part A: Global and Sectoral Aspects. Contribution of Working Group II to the Fifth Assessment Report of the Intergovernmental Panel on Climate Change [Field, C.B., V.R. Barros, D.J. Dokken, K.J. Mach, M.D. Mastrandrea, T.E. Bilir, M. Chatterjee, K.L. Ebi, Y.O. Estrada, R.C. Genova, B. Girma, E.S. Kissel, A.N. Levy, S. MacCracken, P.R. Mastrandrea, and L.L. White (eds.)]*, pages 709–754. Cambridge University Press, Cambridge, United Kingdom and New York, NY, USA.

Sobel, A., Nilsson, J., and Polvani, L. (2001). The Weak Temperature Gradient Approximation and Balanced Tropical Moisture Waves. *Journal of The Atmospheric Sciences*, 58:3650–3665.

Spracklen, D., Baker, J., Garcia-Carreras, L., and Marsham, J. (2018). The Effects of Tropical Vegetation on Rainfall. *Annual Review of Environment and Resources*, 43(1):193–218. doi: 10.1146/annurev-environ-102017-030136.

Spracklen, D. V., Arnold, S. R., and Taylor, C. M. (2012). Observations of increased tropical rainfall preceded by air passage over forests. *Nature*, 489.

Stuecker, M. F., Bitz, C. M., Armour, K. C., Proistosescu, C., Kang, S. M., Xie, S.-P., Kim, D., McGregor, S., Zhang, W., Zhao, S., Cai, W., Dong, Y., and Jin, F.-f. (2018). Polar amplification dominated by local forcing and feedbacks. *Nature Climate Change*, 8:1076–1081. https://doi.org/10.1038/s41558-018-0339-y.

Sutton, R. T., Dong, B., and Gregory, J. M. (2007). Land/sea warming ratio in response to climate change: IPCC AR4 model results and comparison with observations. *Geophysical Research Letters*, 34(2). doi: 10.1029/2006GL028164.

Swann, A. L. S. (2018). Plants and drought in a changing climate. *Current Climate Change Reports*, 4(2):192–201. doi: 10.1007/s40641-018-0097-y.

Swann, A. L. S., Hoffman, F. M., Koven, C. D., and Randerson, J. T. (2016). Plant responses to increasing CO2 reduce estimates of climate impacts on drought severity. *Proceedings of the National Academy of Sciences*, 113(36):10019–10024. doi: 10.1073/pnas.1604581113.

Taylor, K. E., Stouffer, R. J., and Meehl, G. A. (2012). An Overview of CMIP5 and the Experiment Design. *Bulletin of the American Meteorological Society*, 93(4):485–498. doi: 10.1175/BAMS-D-11-00094.1.

Tedeschi, R. G. and Collins, M. (2016). The influence of ENSO on South American precipitation during austral summer and autumn in observations and models. *International Journal of Climatology*, 36(2):618–635. doi: 10.1002/joc.4371.

Thomson, S. I. and Vallis, G. K. (2019). Hierarchical Modeling of Solar System Planets with Isca. *Atmosphere*, 10(12):803. doi: 10.3390/atmos10120803.

Trenberth, K., C. J. and Stepaniak, D. (2001). The atmospheric energy budget and implications for surface fluxes and ocean heat transports. *Clim Dyn*, 17:259–276. https://doi.org/10.1007/PL00007927.

Trenberth, K. and Solomon, A. (1994). The global heat balance: heat transports in the atmosphere and ocean. *Climate Dynamics*, 10:107–134. https://doi.org/10.1007/BF00210625.

Trenberth, K. E. (2011). Changes in precipitation with climate change. *Clim Res*, 47:123–138. https://doi.org/10.3354/cr00953.

Trenberth, K. E., Fasullo, J. T., and Mackaro, J. (2011). Atmospheric Moisture Transports from Ocean to Land and Global Energy Flows in Reanalyses. *Journal of Climate*, 24(18):4907–4924. doi: 10.1175/2011JCLI4171.1.

Trenberth, K. E. and Guillemot, C. J. (1995). Evaluation of the Global Atmospheric Moisture Budget as Seen from Analyses. *Journal of Climate*, 8(9):2255–2272. doi: 10.1175/1520-0442(1995)008<2255:EOTGAM>2.0.CO;2.

Trenberth, K. E., Smith, L., Qian, T., Dai, A., and Fasullo, J. (2007). Estimates of the Global Water Budget and Its Annual Cycle Using Observational and Model Data. *Journal of Hydrometeorology*, 8(4):758–769. doi: 10.1175/JHM600.1.

Trenberth, K. E. and Stepaniak, D. P. (2003). Covariability of Components of Poleward Atmospheric Energy Transports on Seasonal and Interannual Timescales. *Journal of Climate*, 16(22):3691–3705. doi: 10.1175/1520-0442(2003)016<3691:COCOPA>2.0.CO;2.

Vallis, G. K. (2017). *Atmospheric and Oceanic Fluid Dynamics: Fundamentals and Large-Scale Circulation*. Cambridge University Press, Cambridge, U.K., 2nd edition.

Vallis, G. K., Colyer, G., Geen, R., Gerber, E., Jucker, M., Maher, P., Paterson, A., Pietschnig, M., Penn, J., and Thomson, S. I. (2018). Isca, v1.0: a framework for the global modelling of the atmospheres of earth and other planets at varying levels of complexity. *Geoscientific Model Development*, 11(3):843–859. doi: 10.5194/gmd-11-843-2018.

Voigt, A., Biasutti, M., Scheff, J., Bader, J., Bordoni, S., Codron, F., Dixon, R. D., Jonas, J., Kang, S. M., Klingaman, N. P., Leung, R., Lu, J., Mapes, B., Maroon, E. A., McDermid, S., Park, J.-y., Roehrig, R., Rose, B. E. J., Russell, G. L., Seo, J., Toniazzo, T., Wei, H.-H., Yoshimori, M., and Vargas Zeppetello, L. R. (2016). The tropical rain belts with an annual cycle and a continent model intercomparison project: TRACMIP. *Journal of Advances in Modeling Earth Systems*, 8(4):1868–1891. doi: 10.1002/2016MS000748.

Wang, B. and Ding, Q. (2006). Changes in global monsoon precipitation over the past 56 years. *Geophysical Research Letters*, 33(6).

Wang, B., Liu, F., and Chen, G. (2016). A trio-interaction theory for Madden–Julian oscillation. *Geosci. Lett.*, 3(34). https://doi.org/10.1186/s40562-016-0066-z.

Wei, H.-H. and Bordoni, S. (2018). Energetic Constraints on the ITCZ Position in Idealized Simulations With a Seasonal Cycle. *Journal of Advances in Modeling Earth Systems*, 10(7):1708–1725. doi: 10.1029/2018MS001313.

Welch, B. L. (1947). The Generalization of Student's Problem when several different population variances are involved. *Biometrika*, 34(1-2):28–35. doi: 10.1093/biomet/34.1-2.28.

Wills, R. C. and Schneider, T. (2015). Stationary eddies and the zonal asymmetry of net precipitation and ocean freshwater forcing. *Journal of Climate*, 28(13):5115–5133. doi: 10.1175/JCLI-D-14-00573.1.

Wright, J. S., Fu, R., Worden, J. R., Chakraborty, S., Clinton, N. E., Risi, C., Sun, Y., and Yin, L. (2017). Rainforest-initiated wet season onset over the southern amazon. *Proceedings of the National Academy of Sciences*, 114(32):8481–8486. doi: 10.1073/pnas.1621516114.

Xie, S.-P., Deser, C., Vecchi, G. A., Ma, J., Teng, H., and Wittenberg, A. T. (2010). Global Warming Pattern Formation: Sea Surface Temperature and Rainfall. *Journal of Climate*, 23(4):966–986. doi: 10.1175/2009JCLI3329.1.

Yanai, M., Esbensen, S., and Chu, J.-H. (1973). Determination of Bulk Properties of Tropical Cloud Clusters from Large-Scale Heat and Moisture Budgets. *Journal of the Atmospheric Sciences*, 30(4):611–627. doi: 10.1175/1520-0469(1973)030<0611:DOBPOT>2.0.CO;2.

Yang, H., Yang, D., Lei, Z., and Sun, F. (2008). New analytical derivation of the mean annual water-energy balance equation. *Water Resources Research*, 44(3). doi: 10.1029/2007WR006135.

Yano, J.-I. and Ambaum, M. H. P. (2017). Moist static energy: definition, reference constants, a conservation law and effects on buoyancy. *Quarterly Journal of the Royal Meteorological Society*, 143(708):2727–2734. doi: 10.1002/qj.3121.

Yano, J.-I. and Plant, R. S. (2012). Convective quasi-equilibrium. *Reviews of Geophysics*, 50(4). doi: 10.1029/2011RG000378.

Zeng, N., Yoon, J.-H., Marengo, J. A., Subramaniam, A., Nobre, C. A., Mariotti, A., and Neelin, J. D. (2008). Causes and impacts of the 2005 Amazon drought. *Environmental Research Letters*, 3(1):014002. doi: 10.1088/1748-9326/3/1/014002.

Zhang, L., Hickel, K., Dawes, W. R., Chiew, F. H. S., Western, A. W., and Briggs, P. R. (2004). A rational function approach for estimating mean annual evapotranspiration. *Water Resources Research*, 40(2). doi: 10.1029/2003WR002710.